ABSTRACT

Title of Dissertation: DENSE CORE FORMATION AND COLLAPSE
                          IN GIANT MOLECULAR CLOUDS

Hao Gong, Doctor of Philosophy, 2013

Dissertation directed by: Professor Eve C. Ostriker
                           Department of Astronomy

In this thesis we present a unified model for dense core formation and collapse within post-shock dense layers inside giant molecular clouds. Supersonic converging flows collide to compress low density gas to high density clumps, inside which gravitational collapse can happen. We consider both spherically symmetric and planar converging flows, and run models with inflow Mach number $\mathscr{M} \equiv v/c_s = 1.1 - 9$ to investigate the relation between core properties and the bulk velocity dispersion of the mother cloud. Four stages of protostar formation are identified: core building, core collapse, envelope infall, and late accretion. The core building stage takes 10 times as long as core collapse, which lasts a few $\times 10^5$yr, consistent with observed prestellar core lifetimes. We find that the density profiles of cores during collapse can be fitted by Bonnor-Ebert sphere profiles, and that the density and velocity profiles approach the Larson-Penston solution at the core collapse instant. Core shapes change from oblate to prolate as they evolve. Cores with masses varying by three orders of magnitude ($\sim 0.05 - 50$ M$_\odot$) are identified in our high-$\mathscr{M}$ simulations, and a much smaller mass range for models having low $\mathscr{M}$. The median core mass versus $\mathscr{M}$ lies between the minimum mass that can collapse in late times ($\propto \mathscr{M}^{-1}$) and the most evolved core mass ($\propto \mathscr{M}^{-1/2}$). We implement sink particles to the grid code *Athena* to track the collapse of other dense regions of a large scale simulation after the most evolved core collapses, We demonstrate use of our code for applications with a simulation of planar converging supersonic turbulent flows, in which multiple cores

form and collapse to create sinks; these sinks continue to interact and accrete from their surroundings over several Myr.

DENSE CORE FORMATION AND COLLAPSE
IN GIANT MOLECULAR CLOUDS

by

Hao Gong

Dissertation submitted to the Faculty of the Graduate School of the
University of Maryland at College Park in partial fulfillment
of the requirements for the degree of
Doctor of Philosophy
2013

Advisory Committee:

Professor Eve C. Ostriker, chair
Professor Lee Mundy
Professor Massimo Riccoti
Professor James F. Drake (Dean's representative)
Professor Zhi-Yun Li

Preface

This thesis contains research that has already been published. Chapter 2 entitled "Protostar Formation in Supersonic Flows: Growth and Collapse of Spherical Cores" has been published in the Astrophysical Journal (Gong, H. & Ostriker, E. C., 2009, ApJ, 699, 230). Chapter 3 entitled "Dense Core Formation in Supersonic Turbulent Converging Flows" has been published in the Astrophysical Journal (Gong, H. & Ostriker, E. C., 2011, ApJ, 729, 120). Chapter 4 entitled "Implementation of Sink Particles in the Athena Code" has been published in the Astrophysical Journal Supplement Series (Gong, H. & Ostriker, E. C., 2013, ApJS, 204, 8). Simulations presented in Chapter 4 and Chapter 5 were performed on the HPCC deepthought cluster administrated by the OIT at the University of Maryland, as well as the Borg cluster in the Department of the Astronomy. This work was supported by by grants NNG-05GG43G, NNX09AG04G, NNXI0AF60G from NASA.

To my parents, Gong Zhibao and Zhou Qianlian.

Acknowledgements

The past six years and a half at Maryland were amazing and were an important experience in my life. I thank all the people who made this journey enjoyable and my thesis writing possible.

The person I want to thank the most is my advisor, Prof. Eve C. Ostriker. Her innovative thoughts in astronomy always inspire me and help me develop my skills in analysis and coding. Her high standard in scientific research and strict requirement for her students fostered in me the strong will power and confidence for facing difficult situations in science. I thank her for training me towards the scientist I wanted to be.

I want to thank my parents, and my two young sisters. My parents were supportive throughout my academic life. I can not reach this finish line without the support from them.

I am grateful to Dr. Mark Heyer and Prof. John Kwan at the University of Massachusetts. Dr. Heyer introduced star formation to me and showed this fantastic research world. He was so supportive and encouraged me a lot in research. Prof. John Kwan gave me a lot of suggestions on my academic career. The private chats between him and me helped me understand stuff

other than astronomy.

Contents

List of Figures

Chapter 1

Introduction

Stars are the smallest condensed radiating units in the Universe. We know that stars form in giant molecular clouds (GMCs) in the interstellar medium (ISM); Figure 1.1 shows an assembly line of newborn stars in the Vulpecula constellation. However, understanding the details of how stars form is one of the most important unsolved topics in astronomy. Star formation converts the diffuse gas into dense stars with low efficiency ($\sim 1 \ M_\odot/$ yr in the Galaxy). This process happens over several million years across different environments and involves many physical mechanisms.

Star formation theories have been developing for decades. As observations resolve finer details within star forming regions, more fields related to star formation are discovered. The most significant change in the past several decades relates to ideas about the supporting mechanism for dense clumps; there has been a paradigm shift, where magnetic fields have been replaced by turbulence as the mechanism believed to be dominant in controlling clump formation and collapse. This change has yielded an explosion in the development of star formation theory: in addition to modeling the formation of individual stars, theorists have started to consider the formation of GMCs, the source of turbulence inside GMCs, core mass functions (CMFs), the initial stellar mass function (IMF), the relationship between the CMF and the IMF, the large scale star formation ef-

ficiency, and stellar cluster formation, etc. Here CMFs are empirical measurements of dense core mass distributions inside GMCs and the IMF is the stellar mass distribution in open and globular stellar clusters. McKee & Ostriker (2007) divides topics in star formation into two broad categories: microphysics and macrophysics. Microphysics deals with how individual stars form and macrophysics deals with how stellar systems form. In summary, star formation regions and understanding have continued to refine the details of the microphysical processes, while moving into the arena of macrophysics.

Figure 1.1: A PACS/SPIRE three colors composite images (blue=70μm, green=160μm, red=250μm) from *Herschel* of the star forming region in constellation of Vulpecula in the Milky Way. (Courtesy of ESA and the online showcase of *Herschel* images:www.oshi.esa.int)

1.1 Supersonic Turbulence in GMCs

Turbulence is a key process that governs star formation inside GMCs (Mac Low & Klessen 2004; McKee & Ostriker 2007). Research over the past decade has shown that density and velocity fields in turbulence have strong connections to different topics of star formation (see e.g., Hennebelle & Chabrier 2008; Hopkins 2012; Ostriker et al. 2001). The most important feature of turbulence is self-similarity, which can be expressed with the scaling relation $v(l) \propto l^q$, where $v(l)$ is the one-dimensional velocity difference at length scale l. Kolmogorov's classic theory (Kolmogorov 1941) applies to incompressible, homogeneous, isotropic turbulence; this applies to the limit where the sound cross time is infinitely small. With the assumption that the energy transfer rate, $\dot{\varepsilon} \propto v^2(l)/t \propto v^3(l)/l$, is conserved during the energy cascade from larger scales to smaller scales, a power-law relation of $v(l) \sim l^{1/3}$ is derived between $v(l)$ and l. In the limit with no thermal pressure, the energy at a given scale can be dissipated directly via shocks instead of cascading conservatively to the dissipation scale, creating a power-law relation of $v(l) \sim l^{1/2}$. This shock dominated limit is referred to as Burgers turbulence.

The importance of turbulence and shocks in star formation is indicated by the widespread observations of supersonic linewidths in GMCs (see e.g., review of Elmegreen & Scalo 2004). Larson (1981) was the first to systematically analyze the size-velocity relation inside GMCs and used molecular line observations (H_2CO, NH_3 etc.) towards different GMCs inside the Galaxy to empirically derive a relation between velocity dispersion, $\sigma_v(L)$, at size, L,

$$\sigma_v/\mathrm{kms}^{-1} = 1.10\,(L/\mathrm{pc})^{0.38}. \tag{1.1}$$

The power-law scaling relation between observed length scale and velocity dispersion was the first strong evidence that GMCs were turbulent objects. Solomon et al. (1987) furthered the turbulence argument by using the CO line emission from 273 molecular

clouds to get a linewidth-size scaling index of $q \approx 0.5$. Passot et al. (1988) demonstrated that the observed linewidth-size relation, $\sigma(l) \propto l^{1/2}$, in star-forming regions is representative of Burgers turbulence with two-dimensional numerical simulations of compressible flows. Heyer & Brunt (2004) analyzed images of ^{12}CO $J = 1 - 0$ emission of 27 GMCs using the principal component analysis (PCA) and found a scaling index of $q \approx 0.59$ concluding that turbulence in GMCs is universal.

The supersonic turbulence inside GMCs plays a fundamental role in determining the density structure, which is a precursor to star formation. Overdense structures generated by supersonic shocks attract material from surroundings via gravity and some of them grow to be gravitationally unstable and collapse to form stars. Structures that can not grow to be gravitationally bound tend to be dispersed by rarefaction or large scale motions. Thus, understanding the density probability distribution function (PDF) set by supersonic turbulence is fundamental to star formation theory. Numerical simulations of 3D supersonic turbulence with (Li et al. 2004; Ostriker et al. 2001; Ostriker 2003) and without (Klessen 2000) magnetic fields have shown that the density PDF is a log-normal distribution:

$$f(x) = \frac{1}{\sqrt{2\pi\sigma_x^2}} \exp\left[\frac{-(x \pm |\mu_x|)^2}{2\sigma_x^2}\right], \tag{1.2}$$

where $x \equiv \ln(\rho/\bar{\rho})$, and $\mu_x = \sigma_x^2/2$. Here $\bar{\rho}$ is the local mean density. The dispersion, σ_x, scales weakly with the turbulence Mach number (Ostriker et al. 2001; Padoan et al. 1997). Taking $\rho/\bar{\rho} = A_i(1 + \delta_i)$, with $\delta_i > 0$ for compression and $\delta_i < 0$ for rarefaction, the density fluctuations, x, in supersonic turbulence are a sum of random processes – they obey a Gaussian distribution.

1.2 The IMF and the CMF

The IMF is a final outcome of star formation processes and keeps an imprint from the turbulent environment from which it was born. The IMF could be described as a three-part power-law ($\xi(m) \propto m^{-\alpha}$) (Kroupa 2001), with $\alpha = -0.7$ for 0.01 M$_\odot \leq m \leq 0.08$ M$_\odot$, $\alpha = 0.3$ for 0.08 M$_\odot \leq m \leq 0.50$ M$_\odot$, and $\alpha = 1.3$ for 0.50 M$_\odot \leq m$. $dN = \xi(m)d\ln m$ represents the number of stars in the mass interval m to $m + dm$. Miller & Scalo (1979) and Chabrier (2003) show that the low mass end (< 1 M$_\odot$) can be fit smoothly by a log-normal function $dN/d\ln m \propto \exp[-(\ln m - \ln m_c)^2/(2\sigma^2)]$, where m_c is the characteristic stellar mass and σ is the standard deviation of the distribution. Numerous studies reveal that the IMF is nearly invariant in different environments across the Galaxy and the Local Group (see, e.g., reviews of Chabrier 2003; Elmegreen 2009; Kroupa 2001; Scalo 1998).

Dense cores are the immediate precursors of new stars on small scales. CMFs measured in different molecular clouds (e.g., Alves et al. 2007; Beuther & Schilke 2004; Enoch et al. 2006; Ikeda & Kitamura 2009; Ikeda et al. 2009, 2007; Johnstone et al. 2000, 2001; Könyves et al. 2010; Motte et al. 1998, 2001; Nutter & Ward-Thompson 2007; Onishi et al. 2002; Reid & Wilson 2005, 2006; Simpson et al. 2008; Stanke et al. 2006; Testi & Sargent 1998) are strikingly similar in shape to stellar IMFs: a shift of CMFs toward lower masses by a factor of $3 - 4$ is consistent with observed IMFs (see, e.g., Alves et al. 2007; Rathborne et al. 2009). Also, numerical simulations of turbulent, self-gravitating systems (e.g., Basu et al. 2009; Bate 2012; Clark et al. 2008; Gammie et al. 2003; Heitsch et al. 2008; Krumholz et al. 2011, 2012; Li et al. 2004, 2010; Offner et al. 2008; Smith et al. 2009; Tilley & Pudritz 2007; Wang et al. 2010) have shown that the resulting CMFs/IMFs are consistent with observed CMFs/IMFs with a power-law distribution at the large core/stellar mass end.

Based on the fact that the PDF of density structures (Equation 1.2) in turbulent fields

5

are similar to the cosmological Gaussian density fluctuations, Hennebelle & Chabrier (2008) and Hopkins (2012) built analytical theories for the origin of the IMF/CMF in a manner analogous to the cosmological case (Press & Schechter 1974). Their results generally reproduced the observed IMF/CMF. The consistency between observations and theories of the IMF/CMF indicates that turbulence is the dominant mechanism that controls star formation inside GMCs.

However, there is still a big gap in understanding details of the CMF and the IMF connection – how do individual dense cores form and evolve to create stars inside supersonic turbulent GMCs? A unified model to describe this conversion process will be the base for further exploration of many important questions in star formation, such as what processes set final stellar masses, is the IMF really a direct map of CMFs, what determines the characteristic core/stellar mass, what is the role of magnetic fields during star formation, and so on. The objective of this thesis is to build such a model that describes dense core formation and collapse inside "turbulent" GMCs.

1.3   Isothermal Assumption

The isothermal assumption approximately holds for the range of densities and other conditions of interest to core formation. The temperatures inside GMCs are determined by heating and cooling processes. In the outer part of GMCs, the heating is mainly from UV radiation from OB associations and from cosmic rays, and the cooling is from CI and CII fine-structure emission. CO molecules are dissociated by UV radiation. The number density in the outer part increases from 10 to $5 \times 10^2 \mathrm{cm}^{-3}$ and the temperature decreases from about 100 K to 50 K towards the denser interior (Wolfire et al. 2010). In the inner part of GMCs, UV radiation is shielded by high colums of H_2 and CO rotational line emission cooling is dominant. Number density ranges from $5 \times 10^2 \sim 10^4 \mathrm{cm}^{-3}$. Since

CO line cooling is so efficient (Goldsmith 2001; Neufeld et al. 1995) that the temperature in the inner part is almost constant ~ 10 K (Wolfire et al. 2010). Note the observed number density inside dense cores ranges from $10^2 \mathrm{cm}^{-3}$ (edge) to $10^5 \mathrm{cm}^{-3}$, which is the range where the isothermal assumption is appropriate.

Numerical simulations of GMCs with chemical processes, heating and cooling processes support the expectation that the isothermal assumption is valid in high density regions. Calculation by Goldreich & Kwan (1974) showed that the line cooling by CO is able to radiate away the heating from gravitational compression during the collapse of a molecular cloud. Nakamura (1998) studied the collapse of a molecular cloud with gravitational compression heating, and with CO line cooling and dust-gas interaction cooling considered. They found that the temperature is nearly constant (15 K) as the density increases from 10^3 to $10^8 \mathrm{cm}^{-3}$. Glover & Mac Low (2007a,b) and Glover & Clark (2012) showed that the temperature drops from 10^4 K to ~ 10 K as the number density increases from 10^0 to $10^3 \mathrm{cm}^{-3}$ inside GMCs from simulations with chemical processes included. Especially as the number density is above $10 \mathrm{cm}^{-3}$, the polytropic index γ is ~ 1 and is constant.

1.4 Solutions of Spherically Symmetric Isothermal Equations

Before proceeding to review dense core formation, I first introduce realistic solutions of the spherically symmetric isothermal equations, which are used to describe processes during core evolution.

The spherically symmetric fluid equations take the form:

$$\frac{\partial \rho}{\partial t} + \frac{1}{r^2} \frac{\partial (r^2 \rho u)}{\partial r} = 0 \tag{1.3}$$

$$\frac{\partial u}{\partial t} + u\frac{\partial u}{\partial r} = -\frac{c_s^2}{\rho}\frac{\partial \rho}{\partial r} - \frac{GM(r)}{r^2} \tag{1.4}$$

where M is the mass within radius r defined by $dM = 4\pi r^2 \rho dr$, u is the radial velocity, ρ is the density, and the gas pressure $P = \rho c_s^2$. We adopt the isothermal assumption.

To compare the results with previous work in the literature, we use the following non-dimensional variables:

$$D \equiv \frac{\rho}{\rho_c}, m \equiv \frac{GM\sqrt{4\pi G\rho_c}}{c_s^3}, v \equiv \frac{u}{c_s},$$
$$\xi \equiv \frac{r}{c_s}\sqrt{4\pi G\rho_c}, \tau \equiv t\sqrt{4\pi G\rho_c,}. \tag{1.5}$$

where ρ_c is a fiducial density. Using the non-dimensional variables, the fluid equations become:

$$\frac{\partial D}{\partial \tau} + \frac{1}{\xi^2}\frac{\partial(\xi^2 Dv)}{\partial \xi} = 0, \tag{1.6}$$

$$\frac{\partial v}{\partial \tau} + v\frac{\partial v}{\partial \xi} = -\frac{1}{D}\frac{\partial D}{\partial \xi} - \frac{m}{\xi^2}, \tag{1.7}$$

with $m = \int D\xi^2 d\xi$.

1.4.1 Hydrostatic Equilibrium Sphere

For the hydrostatic case, $v = 0$ and $\partial/\partial t = 0$, the governing equations reduce to

$$-\frac{1}{D}\frac{\partial D}{\partial \xi} = \frac{\int D\xi^2 d\xi}{\xi^2}. \tag{1.8}$$

The simplest solution to Equation (1.8) is the singular hydrostatic solution,

$$D = \frac{2}{\xi^2}. \tag{1.9}$$

The solution has a singularity at $\xi = 0$ since $D \to \infty$ as $\xi \to 0$. It is therefore not realistic, and it does not exist in nature. To derive a realistic solution, reasonable boundary conditions are necessary at the inner boundary.

Consider building a sphere from the center with a central density, ρ_c, each shell of density is added to the inner shell with hydrostatic equilibrium (gas pressure gradient

balances the self-gravity) satisfied. Then this sphere can be described by Equation (1.8) with the boundary condition $D(\xi = 0) = 1, \frac{dD}{d\xi}(0) = 0$. It is trivial to show that Equation (1.8) rewrites as:

$$\frac{1}{\xi^2}\frac{\partial}{\partial\xi}\left(\xi^2\frac{\partial\Psi}{\partial\xi}\right) = e^{-\Psi}, \tag{1.10}$$

with $D = \exp(-\Psi)$, and boundary conditions:

$$\begin{aligned} \Psi(0) &= 0, \\ \frac{d\Psi}{d\xi}(0) &= 0. \end{aligned} \tag{1.11}$$

As $\xi \to 0$, the asymptotic solution is derived through Taylor expansion near $\xi = 0$,

$$\Psi = \frac{1}{6}\xi^2, \tag{1.12}$$

which corresponds to

$$D = 1 - \frac{1}{6}\xi^2. \tag{1.13}$$

As $\xi \to \infty$, the solution approaches the singular hydrostatic solution since it always satisfies Equation (1.8). The hydrostatic equilibrium solution consists of the inner flat part and r^{-2} outer part.

Bonnor (1956) and Ebert (1955) show that as the central to edge density ratio ρ_c/ρ_e exceeds 14.3, the hydrostatic equilibrium sphere is unstable. This density ratio corresponds to the non-dimensional radius $\xi_{e,\text{crit}} = 6.45$, which is called the critical radius. A hydrostatic equilibrium sphere is referred to as Bonnor-Ebert sphere (hereafter BE sphere). Figure 1.2 shows stable and unstable BE sphere density profiles.
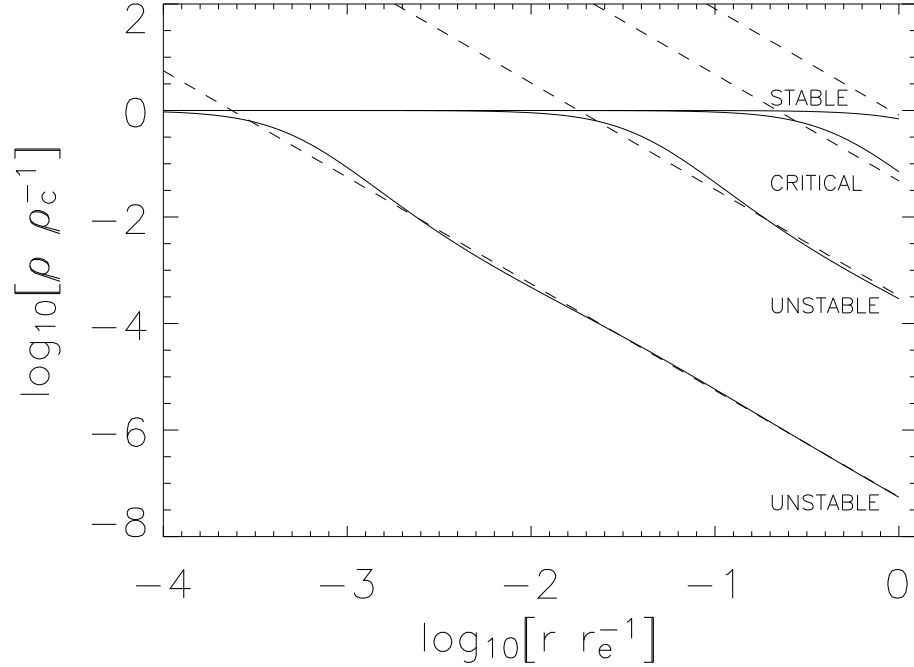
Figure 1.2: BE density profiles for stable and unstable cases versus radius. ρ_c is the central density. r_e is the outer radius, converted from ξ_e through Equation (1.5). The dash lines are the singular density profile (see Equation (1.9)) corresponding to the same radius.

1.4.2 Self-similar Asymptotic Solutions

For a dynamically evolving gaseous sphere, the evolution stages shall be distinguished for with or without a central point mass. Taking protostar formation as an example, a gaseous sphere that is initially gravitationally unstable collapses to form a protostar. After the formation of a protostar at the center, the solution near the center approaches free-fall since the gravitational potential overwhelms the gas pressure, which should be different from the solution before the formation of the central protostar. A set of physical solutions needs to be able to describe the dynamical motions both before and after the protostar formation.

Larson (1969) and Penston (1969) derived the self-similar asymptotic solutions before the protostar formation for $\xi/\tau \to 0$:

$$D = \frac{1.672}{\tau^2}, v = \frac{2}{3}\frac{\xi}{\tau}; \qquad (1.14)$$

and for $\xi/\tau \to \infty$:

$$D = \frac{8.86}{\xi^2}, v = -3.28. \qquad (1.15)$$

The solution described by Equation (1.15) is referred to as the LP solution in the literature after Hunter (1977). Shu (1977) gave the solution near the central point mass ($\xi/\tau \to 0$):

$$D = \left(\frac{m_0}{2\xi^3}\right)^{\frac{1}{2}}\frac{1}{\tau}, v = -\left(\frac{2m_0}{\xi}\right)^{\frac{1}{2}}, \qquad (1.16)$$

where m_0 is the mass of the central point mass. Hunter (1977) joined the LP solution and the Shu (1977) solution and concluded that the LP solution can describe the whole evolution of a collapsing gaseous sphere, from stages before collapse to accretion.

Many numerical simulations of isothermal collapse have shown that the density in the core approaches a $\rho \propto r^{-2}$ profile at the point of protostar formation, regardless of how collapse is initiated (Bodenheimer & Sweigart 1968; Foster & Chevalier 1993; Gómez et al. 2007; Gong & Ostriker 2009, 2011; Hennebelle et al. 2003; Hunter 1977; Larson 1969; Motoyama & Yoshida 2003; Ogino et al. 1999; Penston 1969; Vorobyov & Basu 2005). Foster & Chevalier (1993) checked the validity of the solution described by Equation (1.14) in their numerical simulations. Gong & Ostriker (2009) reported that the linear relation between the velocity and radius was observed in simulations of spherical converging flows. In all these simulations, the central density profiles of collapsing spheres increase steadily but the shape stays flat as time goes on, which is consistent with Equation (1.14).

Note that the density profile from Equation (1.14-1.15), which is flat in the inner part and approaches r^{-2} in the outer part for a collapsing sphere, is similar to the density

11

profile of a BE sphere (Equation (1.13), (1.9)). This is the physical foundation of fitting observed core density profiles (see e.g., André et al. 2007; Goodman et al. 1998; Kirk et al. 2007; Lada et al. 2008; Myers 1983) using the BE sphere profile.

In this section, we do not include the other self-similar solutions such as the set of r^{-2} solutions in Shu (1977), and the "Hunter-b" and "Hunter-d" solutions (Hunter 1977) since they are not stable (Hanawa & Nakayama 1997) and not realistic to be found in nature.

1.5   Individual Core Formation

Shu (1977) presented his classic protostar formation theory based on the "expansion wave" solution of Equation (1.6-1.7). The dense core starts as a singular isothermal sphere with density profile

$$\rho(r) = \frac{2c_s^2}{4\pi G} r^{-2}. \tag{1.17}$$

Given a perturbation, the sphere will collapse from the center and the collapse front expands outwards. The collapse front propagates at the sound speed and the gas inside the expansion front collapses to the center. Since the gas outside the expansion front is initially in a perfectly hydrostatic equilibrium state, it will keep static until the expansion front arrives. The center point mass forms at the beginning of the collapse and accretes at a constant rate, $0.975 \, GM/c_s^3$.

In the 1990s, magnetic fields were thought to offer the dominant support against self-gravity in GMCs (see e.g., Shu et al. 1987), even though the supersonic turbulent motions in GMCs had already been observed (see e.g., Larson 1981; Solomon et al. 1987). Turbulent motions were excluded from the supporting mechanisms due to quick energy dissipation by CO line emission cooling (Goldreich & Kwan 1974). Without turbulence in the picture, the prevailing ideas of dense core formation involved ambipolar diffusion. In ambipolar diffusion regulated core formation, neutrals are free to drift pass ions to form

supercritical cores, and these supercritical cores collapse to form stars.

Shu et al. (1987) combined the "expansion wave" solution and the idea of ambipolar diffusion, and built the "standard star formation model"; which consists of four stages. In the first stage, subcritical clumps contract via ambipolar diffusion to resemble singular isothermal spheres. The second stage is the "inside-out" collapse of these spheres; during this phase, the newly formed protostar is surrounded by a nebular disk. A bipolar flow is created during the third stage, and the fourth stage involves termination of the infall, and the formation of the star with a circumstellar disk.

The difficulty with this core formation picture is the time scale of the prestellar core formation. Numerical simulations of dense core formation and collapse via ambipolar diffusion (see e.g., Basu & Mouschovias 1994, 1995a,b; Mouschovias & Ciolek 1999) showed that the time scale for an initially subcritical core to evolve to supercritical is about 10 Myr, which is much longer than observed prestellar core lifetimes ($2 - 5 \times 10^5$ yr). People started to consider the supersonic turbulence as a key process that could build dense cores in a relatively short time (see e.g., Mac Low & Klessen 2004).

Before considering the core formation process in a strongly turbulent medium, many numerical simulations have investigated individual isothermal core collapse without magnetic fields involved (Bodenheimer & Sweigart 1968; Foster & Chevalier 1993; Hennebelle et al. 2003; Hunter 1977; Larson 1969; Motoyama & Yoshida 2003; Ogino et al. 1999; Penston 1969; Vorobyov & Basu 2005). These simulations included initiation from a static configuration that is unstable without explaining how or where the pre-existing core was formed. Simulations with triggered core collapse (Hennebelle et al. 2003; Motoyama & Yoshida 2003) are motivated by the fact that star-forming regions are highly dynamic, such that external compression may significantly affect core internal evolution, and enhance the accretion rate by raising the central density. Gómez et al. (2007) considered how an impulsive converging velocity field can create gravitationally bound,

centrally concentrated cores.

Core formation induced by supersonic turbulence has been studied in a number of numerical simulations that focus on the large scales (see e.g., Basu et al. 2009; Bonnell et al. 2003; Clark et al. 2008; Gammie et al. 2003; Klessen 2001; Krumholz et al. 2011, 2012; Li et al. 2004; Offner et al. 2008; Smith et al. 2009; Tilley & Pudritz 2004), with much of the emphasis on determining the distribution of core masses for comparison to observed CMFs and the IMF. However, these studies have not had sufficient resolution to investigate the internal properties of the cores that form. If the mass of a core is built up over time as the post-shock product of colliding supersonic flows, what is the detailed evolution leading up to collapse, and during the accretion phase?

We believe that prestellar cores form inside the dense post-shock regions generated by the supersonic, turbulent converging flows inside GMCs. During this process, supersonic turbulence compresses gas to densities at which gravitational collapse can occur rapidly and produce stellar-mass fragments. Figure 1.3 shows this picture of core formation in a GMC size simulation. The four frames show the isovolume of the density field. The sheet-like structures formed by collisions of supersonic shocks are evident in the top left frame. The subsequent figures show the contraction and collapse of prestellar cores inside these sheets.

1.6   Thesis Outline

My thesis is to build a unified core formation and collapse model inside turbulent GMCs demonstrated in Figure 1.3. In Chapter 2, we present a unified model for spherical core formation and evolution, based on numerical simulations of converging, supersonic flows. In Chapter 3, we investigate dense core formation in planar post-shock layers produced by colliding turbulent flows. In Chapter 4, we present the implementation and tests of sink
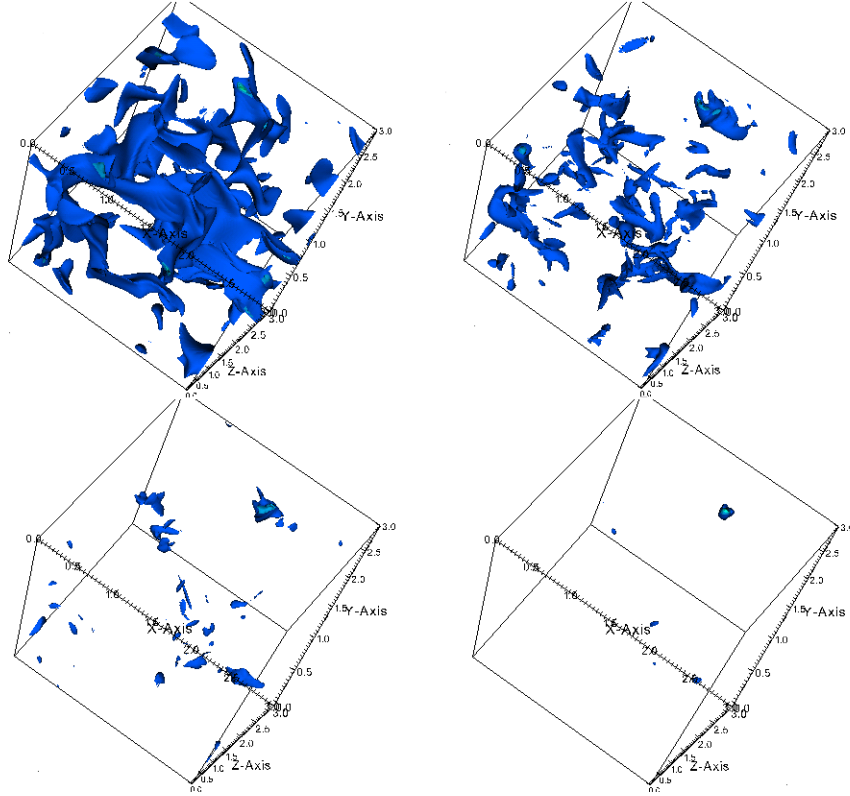
Figure 1.3: Demonstration of core formation. It shows the evolution of an isosurface of density field in a GMC size (~ 10 pc) simulation. The simulation stops at the collapse of the most evolved core. The top left frame shows the isosurface of density at $2\rho_0$ at 2% of the whole time of the simulation (t_{total}). Here ρ_0 is the initial density. The top right frame shows the isosurface of the density at $10\rho_0$ at 68% $\times t_{\text{total}}$. The bottom two frames show the isosurface of density at $15\rho_0$ at 84% $\times t_{\text{total}}$ and $20\rho_0$ at t_{total} from left to right. The two-dimensional post-shock structures are evident in the earliest time, and they contract to form dense cores in the succeeding frames. The maximum density increases dramatically from $85\rho_0$ to $200\rho_0$ in the last two frames indicating gravitational collapse.

particle algorithms in the Eulerian grid-based code Athena. In Chapter 5, we summarize this thesis, and discuss prospects for future research.

Chapter 2

Protostar Formation in Supersonic Flows: Growth and Collapse of Spherical Cores

Abstract

We present a unified model for molecular core formation and evolution, based on numerical simulations of converging, supersonic flows. Our model applies to star formation in giant molecular clouds dominated by large-scale turbulence, and contains four main stages: core building, core collapse, envelope infall, and late accretion. During the building stage, cores form out of dense, post-shock gas, and become increasingly centrally stratified as the mass grows over time. Even for highly supersonic converging flows, the dense gas is subsonic, consistent with observations showing quiescent cores. When the shock radius defining the core boundary exceeds $R \approx 4a(4\pi G\rho_{\mathrm{mean}})^{-1/2}$, where a is the isothermal sound speed, a wave of collapse propagates from the edge to the center. During the building and collapse stages, density profiles can be fitted by Bonnor–Ebert profiles with temperature 1.2 - 2.9 times the true value, similar to many observed cores.

As found previously for initially static equilibria, outside-in collapse leads to a Larson–Penston density profile $\rho \approx 8.86a^2/(4\pi Gr^2)$. The third stage, consisting of an inside-out wave of gravitational rarefaction leading to $\rho \propto r^{-3/2}$, $v \propto r^{-1/2}$, is also similar to that for initially static spheres, as originally described by Shu. We find that the collapse and infall stages have comparable duration, $\sim t_{\mathrm{ff}}$, consistent with estimates for observed prestellar and protostellar (Class 0/I) cores. Core building takes longer, but does not produce high-contrast objects until shortly before collapse. The time to reach core collapse, and the core mass at collapse, decrease with increasing inflow Mach number. For all cases the accretion rate is $\gg a^3/G$ early on but sharply drops off; the final system mass depends on the duration of late-stage accretion, set by large-scale conditions in a cloud.

2.1   Introduction

Dense molecular cores are the immediate precursors of new stars on small scales, and understanding how they grow and evolve is fundamental to the theory of star formation (McKee & Ostriker 2007; Shu et al. 1987). Because many elements are involved in core formation, complete theoretical models have not yet been developed, and it is not yet clear whether a single dynamical effect dominates the overall process, or whether several contributing effects have comparable importance. In one limit that has been studied in some detail, ambient velocities are negligible, and self-gravitating cores form by the slow diffusion of partially-ionized gas through strongly supporting magnetic fields until a supercritical configuration is reached (e.g., Mouschovias & Ciolek 1999). In another limit, which has been considered more recently—but in much less detail at core scales, magnetic support is negligible, and supersonic turbulence creates and destroys condensations, with some fraction of this gas sufficiently dense and long-lived that it can undergo collapse (e.g., Mac Low & Klessen 2004). As observed clouds are both magnetized and

strongly turbulent, the eventual theory for core formation that is developed must account for both processes; pioneering work towards this goal has begun (e.g., Kudoh & Basu 2008; Nakamura & Li 2008). Because of the technical challenges involved in building comprehensive models and the need to elucidate the contributing physics, it is important to develop simplified models in greater detail. In this contribution, we consider aspects of core growth and evolution in the turbulence-dominated, unmagnetized limit.

Increasingly detailed observations in recent years provide constraints on theoretical models (see, e.g., the reviews of André et al. 2008; di Francesco et al. 2007; Ward-Thompson et al. 2007). One class of observations focuses on the density distribution within cores. One-dimensional (angle-averaged) density profiles (e.g., Alves et al. 2001; Bacmann et al. 2000; Evans et al. 2001; Kandori et al. 2005; Kirk et al. 2005; Shirley et al. 2000; Ward-Thompson et al. 1994) generally show a uniform-density center surrounded by a power-law envelope extending to an outer radius ~ 0.1 pc, which is consistent with the density profile of a static, isothermal, unmagnetized Bonnor–Ebert (hereafter BE) sphere (Bonnor 1956; Ebert 1955). The interpretation in terms of static equilibrium is problematic, however, insofar as many cases show center-to-edge density contrasts exceeding the maximum ratio ($\rho_c/\rho_{\text{edge}} = 14.0$; here ρ_c is the central density) that would be stable against collapse, and would also require central temperatures greater than observed values in order to provide support for the total masses inferred from the integrated continuum emission. In addition, cores are generally not isolated; rather than being surrounded by a high-temperature, low-density medium with pressure matching the core's outer edge, they are surrounded by moderate-density cold molecular gas representing clumps and filaments within larger clouds (Bergin & Tafalla 2007). The interpretation of observed density profiles as static solutions is also not unique, in that dynamically collapsing cores initiated from near-critical equilibrium show the same density profiles as (supercritical) static solutions (see, e.g., Kandori et al. 2005; Myers 2005, and below).

Concentrations formed within turbulent flows can also have density profiles resembling BE spheres (Ballesteros-Paredes et al. 2003).

Velocity information can distinguish between static, oscillating (Broderick et al. 2007; Keto et al. 2006), and collapsing cores, and can potentially also help discriminate how these cores formed out of more diffuse gas. Dense, low-mass cores generally have subsonic internal velocity dispersions, whether for isolated cores or for cores found in clusters (e.g., André et al. 2007; Goodman et al. 1998; Kirk et al. 2007; Lada et al. 2008; Myers 1983). In cores containing protostars, signatures of infall on small scales ($\sim 0.01 - 0.1$ pc), believed to be indicative of gravitational collapse, have been observed via the asymmetry of molecular lines that trace high-density gas (e.g., Di Francesco et al. 2001; Gregersen et al. 1997; Mardones et al. 1997; Zhou et al. 1993). For prestellar cores, inward motions are often evident over both small ($\lesssim 0.1$ pc) and larger scales ($\sim 0.1 - 0.4$ pc), sometimes encompassing a whole star-forming complex (Lee et al. 1999, 2001; Walsh et al. 2006; see also Peretto et al. 2006). Small-scale inward motions within cores are subsonic (Lee et al. 2001), while larger-scale motions can be transonic or supersonic (Walsh et al. 2006 infer higher velocities in lower-density gas), and may be indicative of converging larger-scale flows in which dense gas builds up in a shock-bounded stagnation region.

The relative durations of prestellar and protostellar (i.e., containing an accreting embedded Class 0 or I object) stages of core evolution are determined by comparing the relative numbers of the two classes of sources in a given cloud. Absolute core lifetimes are further obtained by comparison to the number of T Tauri stars with measured ages. Several studies using this statistical approach in different clouds have reached similar conclusions: the durations of the prestellar and accreting stages of cores are comparable (Beichman et al. 1986; Enoch et al. 2008; Evans et al. 2008; Hatchell et al. 2007; Jessop & Ward-Thompson 2000; Jørgensen et al. 2007; Kirk et al. 2005; Lee et al. 1999). Typical

prestellar core lifetimes are estimated at $\sim 2 - 5 \times 10^5$ yr, amounting to a few times the free-fall time

$$t_{\text{ff}} \equiv \left(\frac{3\pi}{32G\bar{\rho}} \right)^{1/2} = 1.37 \times 10^5 \text{ yr} \left(\frac{\bar{n}_H}{10^5 \text{ cm}^{-3}} \right)^{-1/2} \qquad (2.1)$$

measured at the mean core density $\bar{\rho} = 1.4 m_H \bar{n}_H$. With lifetimes considerably below the ambipolar diffusion time for strong magnetic fields $t_{AD} \approx 10 t_{\text{ff}}$ (e.g., Mouschovias & Ciolek 1999), this suggests that observed cores are gravitationally supercritical with respect to the magnetic field. This conclusion is also supported by magnetic field Zeeman observations, indicating that cores have mean mass-to-magnetic flux ratios two times the critical value (Troland & Crutcher 2008). Since cores are only identified in millimeter and submillimeter continuum when the n_H exceeds a few $\times 10^4 \text{ cm}^{-3}$, in principle it is possible that an extended period of slow diffusion at lower density precedes the observed core stage. Turbulence accelerates ambipolar diffusion, however (e.g., Fatuzzo & Adams 2002; Heitsch et al. 2004; Li & Nakamura 2004; Zweibel 2002), so it is also possible that the flux loss needed to reach a magnetically supercritical state may occur more dynamically, at densities below 10^4 cm^{-3}.

Theoretical modeling of core evolution has a long history. Much work has focused on the evolution of unstable thermally supported equilibria into collapse (formally resulting in infinite density at the origin), followed by accretion of the envelope. Self-similar solutions for collapse and/or accretion stages of isothermal spheres were found by Larson (1969), Penston (1969), Shu (1977), and Hunter (1977); these were later generalized by Whitworth & Summers (1985). Larson (1969) and Penston (1969) (hereafter LP) independently found self-similar solutions which describe the density and velocity prior to the instant of protostar formation (defined as the instant at which the central density becomes infinite). In the LP solution, the radial velocity approaches a constant value $-3.28a$ and the density approaches

$$\rho = 8.86 \frac{a^2}{4\pi G r^2} \qquad (2.2)$$

at the instant of central protostar formation, with mass inflow rate $\dot{M} = 29.1\,a^3/G$. Here, a is the isothermal sound speed, and the dimensional factor in the accretion rate is given by

$$\frac{a^3}{G} = 1.6 \times 10^{-6}\ \mathrm{M_\odot\ yr^{-1}} \left(\frac{T}{10K}\right)^{3/2}. \tag{2.3}$$

The analysis of Shu (1977) showed that for an initial profile that is a static singular isothermal sphere, $\rho = 2a^2/(4\pi G r^2)$, evolution yields an "inside-out" infall solution in which a wave of rarefaction propagates outward at the sound speed. Inside of the expansion wave, the mass inflow rate is $\dot{M} = 0.975\,a^3/G$ independent of r, and gas accelerates to free fall ($v \propto r^{-1/2}$, $\rho \propto r^{-3/2}$). Hunter (1977) connected and extended the investigations of LP (which address evolution prior to protostar formation) with that of Shu (which focuses on the accretion stage). He showed that self-similar solutions before and after the point of singularity formation (i.e., $t = 0$) can be smoothly matched. This allowed the LP solution to be extended into the accretion phase with similar free-fall behavior near the origin; Hunter (1977) also found a sequence of self-similar solutions valid for all time that approach the Shu (1977) expansion wave solution.

Many numerical simulations of isothermal collapse have shown that the density in the core approaches a $\rho \propto r^{-2}$ profile at the point of protostar formation, regardless of how collapse is initiated (Bodenheimer & Sweigart 1968; Foster & Chevalier 1993; Gómez et al. 2007; Hennebelle et al. 2003; Hunter 1977; Larson 1969; Motoyama & Yoshida 2003; Ogino et al. 1999; Penston 1969; Vorobyov & Basu 2005). These simulations include initiation from a static configuration that is unstable, and initiation from static, stable configurations that are subjected to transient compression, either from enhanced external pressure or a converging velocity field. Another feature common to the results from simulations is that the collapse generally begins on the outside, with the infalling region propagating inward as the central density increases. At the time of singularity formation, the central velocity has been found to be comparable to the value $-3.3a$ derived by LP,

with the density normalization also similar to the LP result (Foster & Chevalier 1993; Ogino et al. 1999). Following the instant of protostar formation, the evolution of the mass accretion rate over time depends strongly on the initial conditions, however.

Simulations with triggered core collapse (Hennebelle et al. 2003; Motoyama & Yoshida 2003) are motivated by the fact that star-forming regions are highly dynamic, such that external compression may significantly affect core internal evolution, and enhance the accretion rate by raising the central density. Triggering events may be associated with high–mass star formation, but even without these highly energetic events, the large-scale turbulence that pervades giant molecular clouds (GMCs) can compress initially quiescent cores. Taking this idea one step further, it is interesting to consider not just the core-collapse process, but also the core formation process, in a strongly turbulent medium. Gómez et al. (2007) conducted one such study, considering how an impulsive converging velocity field can create gravitationally bound, centrally concentrated cores. Core formation induced by supersonic turbulence has also been studied in a number of numerical simulations that focus on the large scales, with much of the emphasis on determining the distribution of core masses for comparison to observed core mass functions and the stellar initial mass function (IMF; see, e.g., the review of McKee & Ostriker (2007)). However, these studies have not had sufficient resolution to investigate the internal properties of the cores that form. If the mass of a core is built up over time as the post-shock product of colliding supersonic flows, what is the detailed evolution leading up to collapse, and during the accretion phase?

In this chapter, we initiate a study of dynamically induced core formation and collapse by considering perhaps the simplest possible situation: a supersonic, converging, spherical flow. Our initial conditions are a uniform low-density medium with no stratification. A dense core forms inside a spherical shock, and over time becomes stratified as its mass grows and it becomes self-gravitating. When the stratification becomes too great,

collapse and subsequent accretion occurs in a similar manner to the case of an initially-unstable static equilibrium. We consider cases of varying inflow Mach number, and with the large-scale inflow either steady over all time, or shut off after an interval.

The condition of spherical inflow that we adopt for this first study is, of course, likely to be rare in real clouds. As the main purpose of this study is to take the first step towards unified models of core formation and collapse in dynamic environments, however, we consider one-dimensional solutions the natural place to start. We shall show that many features consistent with observed cores are evident even in these idealized models, suggesting that they are generic to dynamic core formation scenarios. The present set of simulations, in addition to enabling identification of characteristic evolutionary stages, also serve as a useful reference point for more realistic but more complex simulations. More typical than a converging spherical flow would be a converging planar flow, which yields a dense post-shock stagnation layer in which self-gravitating cores can form. Numerical studies that we have begun for supersonic planar inflows show results for core building and collapse that are qualitatively similar to the present results for supersonic spherical inflows.

The plan of this chapter is as follows: in Section 2 we present the governing equations and describe our problem specification and numerical method. Section 3 briefly describes results of collapse initiated from static configurations, demonstrating that we reproduce prior results, and providing a baseline for comparison to our models of dynamic formation and collapse. Section 4 presents numerical results for our converging-flow simulations, covering the stage of core formation and evolution up to the point of singularity formation in Section 4.1 and the subsequent stages in Section 4.2. We introduce a breakdown into new physically defined stages in Section 4.3, and quantify the evolution of accretion rates in Section 4.4. Section 5 summarizes our new results and discusses our findings in the context of previous theory and observations.

2.2 Governing Equations and Numerical Methods

The equations of motion for a spherically symmetric flow take the form:

$$\frac{\partial \rho}{\partial t} + \frac{1}{r^2}\frac{\partial (r^2 \rho v)}{\partial r} = 0, \tag{2.4}$$

$$\frac{\partial v}{\partial t} + v\frac{\partial v}{\partial r} = -\frac{1}{\rho}\frac{\partial P}{\partial r} - \frac{GM(r)}{r^2}, \tag{2.5}$$

where M is the mass within radius r defined by $dM = 4\pi r^2 \rho dr$, v is the radial velocity, P is the gas pressure, and ρ is the density. For prestellar collapse, an isothermal equation of state $P = a^2\rho$ is often used, because cooling is so efficient that the gas remains at nearly constant temperature during the gravitational collapse (Larson 1969; Nakamura 1998). We adopt an isothermal equation of state.

For ease of comparison with previous work, we introduce the following dimensionless variables:

$$\tau \equiv t/t_0, \tag{2.6}$$

$$\xi \equiv r/r_0, \tag{2.7}$$

$$D \equiv \rho/\rho_0, \tag{2.8}$$

$$u \equiv v/a, \tag{2.9}$$

$$m \equiv M/M_0. \tag{2.10}$$

Here ρ_0 is a fiducial density representing the volume-averaged ambient density in a cloud on large scales, which we shall later set to the uniform density of the converging flow. The unit of velocity is the isothermal sound speed

$$a = 0.19 \text{ km s}^{-1}\left(\frac{T}{10\text{ K}}\right)^{1/2}, \tag{2.11}$$

the unit of time is related to the free-fall time at the fiducial density by

$$t_0 \equiv \frac{1}{(4\pi G\rho_0)^{1/2}} = 0.52 t_{ff} = 2.3 \times 10^6 \text{ yr}\left(\frac{n_H}{10^2\text{ cm}^{-3}}\right)^{-1/2}, \tag{2.12}$$

24

the unit of length is related to the Jeans length at the fiducial density $L_J \equiv a(\pi/G\rho_0)^{1/2}$ by

$$r_0 \equiv \frac{a}{(4\pi G\rho_0)^{1/2}} = \frac{L_J}{2\pi} = 0.44 \text{ pc} \left(\frac{T}{10 \text{ K}}\right)^{1/2} \left(\frac{n_H}{10^2 \text{ cm}^{-3}}\right)^{-1/2}, \qquad (2.13)$$

and the corresponding basic unit of mass is $\rho_0 r_0^3 = a^3/[4\pi(4\pi G^3\rho_0)^{1/2}]$. The mass unit adopted in equation (2.10) is larger than this by a factor 4π:

$$M_0 \equiv \frac{a^3}{(4\pi G^3\rho_0)^{1/2}} = 3.7 \text{ M}_\odot \left(\frac{T}{10 \text{ K}}\right)^{3/2} \left(\frac{n_H}{10^2 \text{ cm}^{-3}}\right)^{-1/2}. \qquad (2.14)$$

With the dimensionless variables, the fluid equations become

$$\frac{\partial D}{\partial \tau} + \frac{1}{\xi^2}\frac{\partial(\xi^2 Du)}{\partial \xi} = 0, \qquad (2.15)$$

$$\frac{\partial u}{\partial \tau} + u\frac{\partial u}{\partial \xi} = -\frac{1}{D}\frac{\partial D}{\partial \xi} - \frac{m}{\xi^2}, \qquad (2.16)$$

$$m = \int D\xi^2 d\xi. \qquad (2.17)$$

We solve the one-dimensional hydrodynamic equations (2.15)-(2.17) with the ZEUS-2D (Stone & Norman 1992) code, in spherical symmetry. During the evolution to singularity formation (collapse phase), we adopt an inner reflecting boundary condition. For the post-collapse accretion phase, we implement a sink cell (Boss & Black 1982; Ogino et al. 1999) at the origin when the central density reaches a reference value. Subsequently, the inner boundary condition is changed to "outflow" (i.e. flow in the inward radial direction off the grid at the smallest radius) and the value of the central point mass is tracked via the integrated flow off the grid, with $\dot{M}_{\text{ctr}} = (a^3/G)D_{\text{in}}u_{\text{in}}\xi_{\text{in}}^2$. The sink cell is only implemented after the inflow in the central region becomes supersonic, so that information from the inner boundary cannot propagate into the remainder of the grid.

2.3 Evolution of Initially-Static Cores

As discussed in Section 1, many previous numerical simulations of core evolution have adopted static initial conditions and a fixed total mass (e.g., Foster & Chevalier 1993; Hunter 1977; Ogino et al. 1999; Vorobyov & Basu 2005). The adopted initial density profile shapes are consistent with (or similar to) a hydrostatic equilibrium, i.e., a BE sphere, with the initial density perturbed above the value that can be supported by the internal pressure in order to initiate collapse. These fixed-mass simulations adopt a prescribed external pressure at a low density with an effectively Lagrangian outer boundary (Hunter 1977), or else a fixed outer boundary with prescribed external pressure and no mass inflow (Ogino et al. 1999; Vorobyov & Basu 2005). Foster & Chevalier (1993) explored both types of boundary conditions, and found very similar results for a given initial cloud density profile. They concluded that the evolution for the fixed-mass case is insensitive to the outer boundary condition for initially unstable equilibria. This is consistent with the argument of Bodenheimer & Sweigart (1968) that the outer boundary condition does not affect evolution up to collapse as long as the free-fall time (Equation 2.1) is shorter than the cloud crossing time. The ratio of the free-fall time at the mean density to the sound crossing time $r_{\max}/a$ over the radius of a BE sphere is $\pi/(8\xi\frac{d\Psi}{d\xi})^{1/2}$, which approaches $\pi/4 \sim 0.785$ as ξ approaches infinity. Here, $\Psi = \Phi/a^2$, the dimensionless gravitational potential. For the critical case, the free-fall time is 0.71 times the sound crossing time over the radius.

For comparison to previous work, we consider collapse of an initially-static BE sphere. For initial conditions, we adopt a critical BE sphere, i.e., the outer boundary of the grid is at radius

$$R_{\mathrm{BE,crit}} = 6.45\frac{a}{(4\pi G\rho_c)^{1/2}} = 1.72\frac{a}{(4\pi G\rho_{\mathrm{edge}})^{1/2}} = 2.70\frac{a}{(4\pi G\rho_{\mathrm{mean}})^{1/2}} \qquad (2.18)$$

corresponding to dimensionless outer radius $\xi_e = \xi_{\mathrm{crit}} = 6.45(\rho_0/\rho_c)^{1/2}$. Here, $\rho_{\mathrm{mean}} =$

$2.45 \rho_{\mathrm{edge}}$ is the total core mass divided by its volume. The mass of the critical BE sphere is

$$M_{\mathrm{BE,crit}} = 1.18 \frac{a^4}{(G^3 P_{\mathrm{edge}})^{1/2}} = 4.18 \frac{a^3}{(4\pi G^3 \rho_{\mathrm{edge}})^{1/2}} = 1.5 \ \mathrm{M_\odot} \left(\frac{T}{10 \ \mathrm{K}} \right)^{3/2} \left(\frac{n_{\mathrm{H,edge}}}{10^4 \ \mathrm{cm^{-3}}} \right)^{-1/2}.$$

(2.19)

To initiate collapse, density is perturbed above the equilibrium value by 10%. Our outer boundary condition is at a fixed pressure, with no inflow. The temporal evolution of the accretion rate for this model is shown in Figure 2.1.
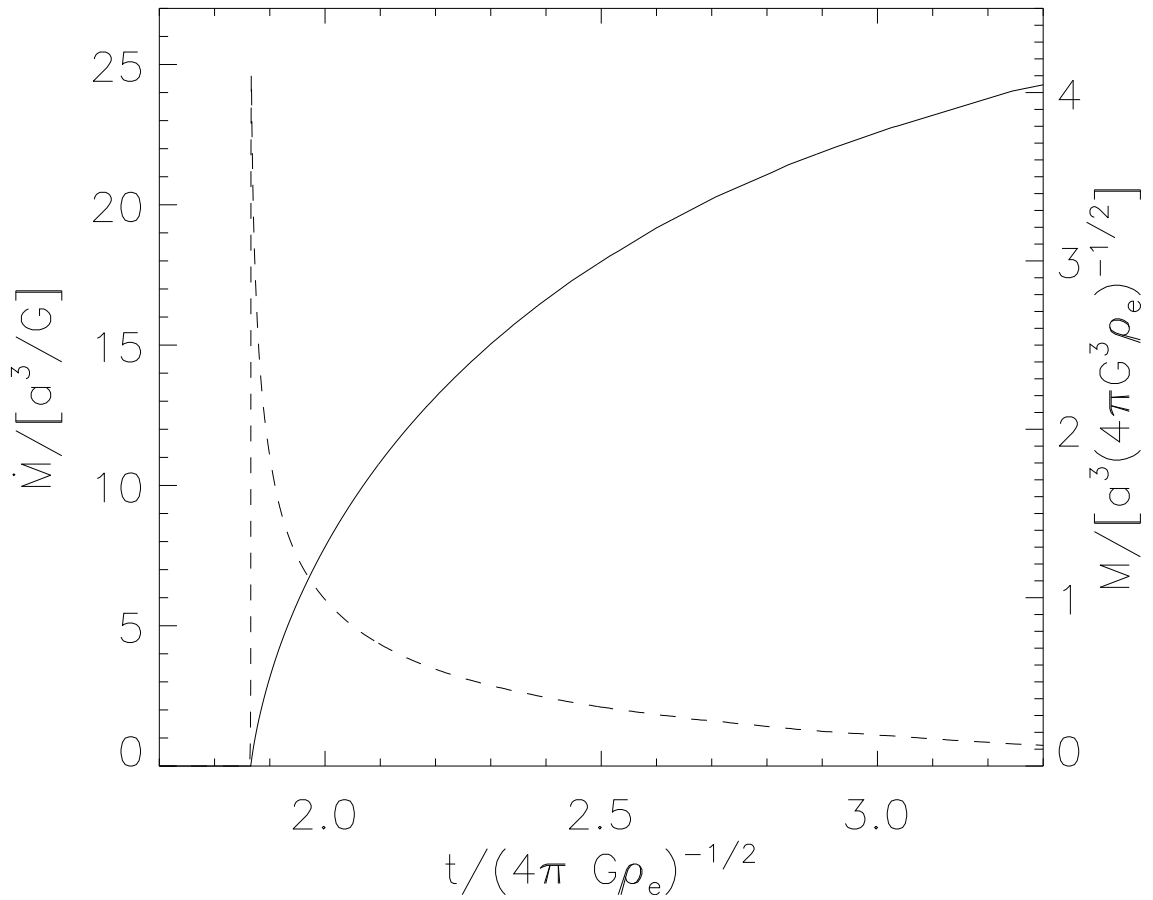
Figure 2.1: *Dashed curve, left scale:* The temporal evolution of the mass accretion rate at inner edge of the grid, for collapse initiated from a critical BE sphere (see Equation 2.3 for units). *Solid curve, right scale:* Evolution of the central point mass (see Equation 2.14 for units). Time is shown in units scaled by the density at the outer edge (see Equation 2.12).

Features similar to those outlined by Vorobyov & Basu (2005) are observed in our

simulation. The accretion rate peaks at a value approaching the LP prediction at the instant when the central density (formally) becomes infinite, and steeply decreases thereafter. Vorobyov & Basu (2005) find that the decline in the accretion rate after singularity formation (unlike the increase in the accretion rate in Hunter's self-similar extension of the LP solution) can be attributed to the variation of velocity with radius in the sphere as it evolves toward collapse. We also considered cases of much larger initial static spheres, with outer boundaries $\xi_e = 5\,\xi_{\rm crit}$ corresponding to highly unstable BE configurations. For these cases, the accretion rate decreases until it reaches a plateau at $\dot{M} = 1.45\,a^3/G$, consistent with the value reported in Shu (1977) (when the density is 10% greater than for hydrostatic equilibrium), and then further declines to zero after a rarefaction wave propagates inward from the outer boundary to reach the center.

Similar to the results of previous simulations, we find that the first collapse is "outside-in," with velocities initially nonzero only in the outer parts where the imbalance between gravity and pressure is largest. For cases where the initial sphere is larger than the critical BE sphere, collapse begins at radii near $\xi_{\rm crit}$, as was previously shown by Foster & Chevalier (1993). This is because the inner portions of the sphere, at $\xi < \xi_{\rm crit}$, initially are equivalent to *stable* BE solutions. In all of our models initiated from static spheres, the density profile approaches the LP self-similar solution $D = 8.86\xi^{-2}$, and the velocity in the inner region approaches $-3.28a$, at the moment of singularity formation. Before this time, the density profile in the central region is flat with a magnitude that increases over time. The process can be thought of as a wave of compression propagating from the outside to the inside, creating a density distribution in which the ratio of radius to the Jeans length at the local density is everywhere constant: $r/L_J(r) \approx \sqrt{8.86}/2\pi \approx 0.47$. The singularity represents the instant the compression wave converges at the center.

Supersonic inflow velocities can be achieved without shock formation in the interior of the core (except at $r = 0$) because inward acceleration occurs at all radii where the

inward gravitational force exceeds the outward pressure force. By construction, the solutions initiated from static configurations all have gravity (slightly) exceeding pressure forces everywhere in the initial state, so that the inward acceleration is nonzero. After a singularity forms at the center, accretion begins, and the flow in the interior transitions from the $v = const.$, $\rho \propto r^{-2}$ LP solution to a free-fall solution, with the accreting region propagating from the interior to the exterior in a manner similar to that described by Shu (1977). Thus, while collapse develops in an "outside-in" fashion, accretion develops in an "inside-out" fashion. Note that accretion in any centrally concentrated configuration should work its way outward from the center, because gravitational collapse times decline outwards $\propto \rho^{-1/2}$, which is $t_{\mathrm{ff}} \propto r$ for an inverse-square density profile (true for either the LP profile or the singular isothermal sphere).

2.4   Converging-Flow Model Results

In this section, we present the results of our simulations of core formation and evolution for the case of converging spherical, supersonic flows. For these simulations, the outer boundary condition at ξ_{max} is maintained at a constant density and inflow velocity. The inflow velocity is characterized by the Mach number relative to the isothermal sound speed, $\mathcal{M} \equiv v_{\mathrm{in}}/a$. We vary $\mathcal{M}$ over the range from 1.05 to 7. For some models (see below), we suppress inflow at the outer radius after collapse occurs to test how the late-time accretion rate is altered. The initial conditions consist of uniform (low) density, and uniform inflow velocity equal to the value at the outer boundary. The size of the grid, in terms of the reference length scale given in equation (2.13), is $2.51327 r_0$, which amounts to a fraction 0.4 of the Jeans length at the initial density. Note that the radius of a critical BE sphere at the same external pressure (so that $\rho_{\mathrm{edge}} = \rho_0$) would be $R_{\mathrm{BE,crit}} = 6.45(\rho_{\mathrm{edge}}/\rho_c)^{1/2} r_0 = 1.72 r_0$. That is, a critical BE sphere confined by the same ambient

pressure would be able to fit within our simulation domain, with plenty of room to spare. The size of zones in the radial direction has a constant logarithmic increment, i.e., $\Delta r_{i+1} = (1+\alpha)\Delta r_i$, for some $\alpha > 0$, such that $r_i = r_1 + \alpha^{-1}[(1+\alpha)^{i-1} - 1]\Delta r_1$ and $\Delta r_1/(r_{max} - r_{min}) = \alpha[(1+\alpha)^{N-1} - 1]^{-1}$. For all the converging–flow simulations in this chapter, α is set to 0.009; 605 and 597 grids are used during the collapse phase and accretion phase, respectively.

2.4.1 Core Formation and Collapse

We begin with a description of the core formation process, which is similar for all of the converging-flow models. Because of the reflecting boundary condition at the center and the initial inflow velocities, immediately after we initiate the simulation, a shock forms at the origin and propagates outward. The inflowing matter is compressed by the shock. The shock front divides the converging inflow into two regions: an inner dense post-shock region and an outer low-density region of supersonic inflow. These two regions evolve quasi-independently but are connected by shock jump conditions. Under competition between gas pressure and self-gravity, the inner region contracts slowly to begin forming a dense core. As self-gravity starts to overwhelm gas pressure, the dense core enters the collapse phase.

At the beginning, the inner region is quasi-hydrostatic, with the velocity a linear function of radius. With negligible density gradient and self-gravity in the early stages, equation (2.16) becomes

$$\frac{\partial u}{\partial \tau} + u\frac{\partial u}{\partial \xi} \approx 0. \tag{2.20}$$

This equation is satisfied by

$$u = \frac{\xi}{\tau - \tau_0}; \tag{2.21}$$

for $|\tau/\tau_0| \ll 1$, $u \approx -\xi/\tau_0$, i.e., the coefficient of the linear profile is constant in time. The leftmost lower panels of Figures 2.2 - 2.5 show this linear-velocity behavior in the
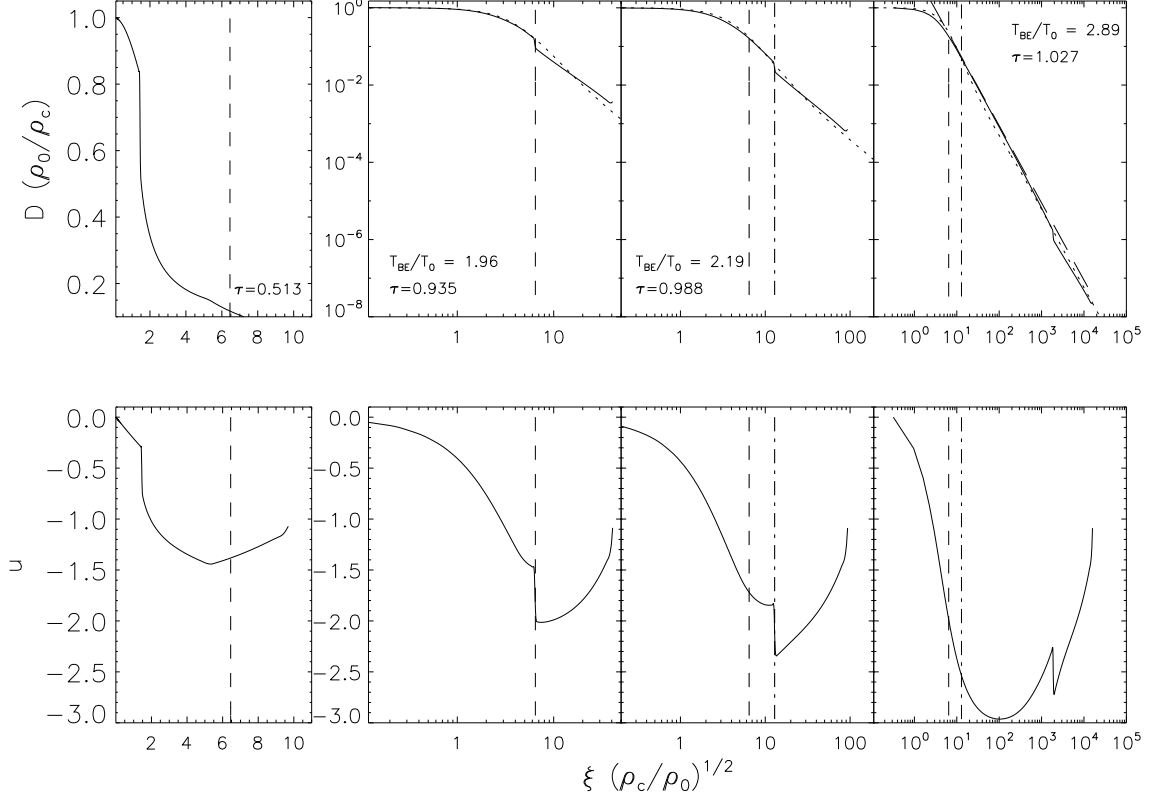
Figure 2.2: Density and velocity profiles (*solid lines*) for converging-flow model with $\mathcal{M} = 1.05$, at times τ as noted in the upper panel for each pair. The radius is normalized by the central density, i.e., the abscissa is $r(4\pi G\rho_c)^{1/2}/a$. For the three upper panels on the right, the dotted line is a fit to a BE sphere with temperature T_{BE}, with the fitted temperature noted in each panel. Dashed vertical lines denote the critical radius of a BE sphere with the same central density and sound speed a. Dot-dashed vertical lines mark twice this critical radius. The time for the leftmost pair is half of the collapse time τ_{coll}. The time for the second and third pairs are when the shock reaches the critical BE radius and twice that value. The time for the last pair is the instant of collapse τ_{coll} (defined in the simulations as $\rho_c/\rho_0 = 4 \times 10^7$). The top-right panel shows with a dashed diagonal line the LP density profile $D = 8.86\xi^{-2}$.

shocked region, at the time that equals half of the collapse time τ_{coll}. Throughout this chapter, we define the collapse time τ_{coll} as the moment that $\rho_c/\rho_0 = 4 \times 10^7$. Shown in the leftmost upper panels of Figures 2.2 - 2.5 are the density profiles; even when the density profile has nonzero gradients, the velocity in the inner region is dominated by the linear term. Note that the leftmost panels have linear–linear scales. The velocity over the whole post-shock region is subsonic and negative, which means the core is slowly

contracting. For the $\mathscr{M} = 4$, 7 models (see Figures 2.4, and 2.5), the inner part of the density and velocity profiles oscillate at the beginning of simulations. As the shock front propagates outward, the mass inside the shock increases, and so does self-gravity. After a period of accumulation lasting about 90% of the time until collapse τ_{coll}, the slowly contracting dense region starts to be gravitationally unstable.
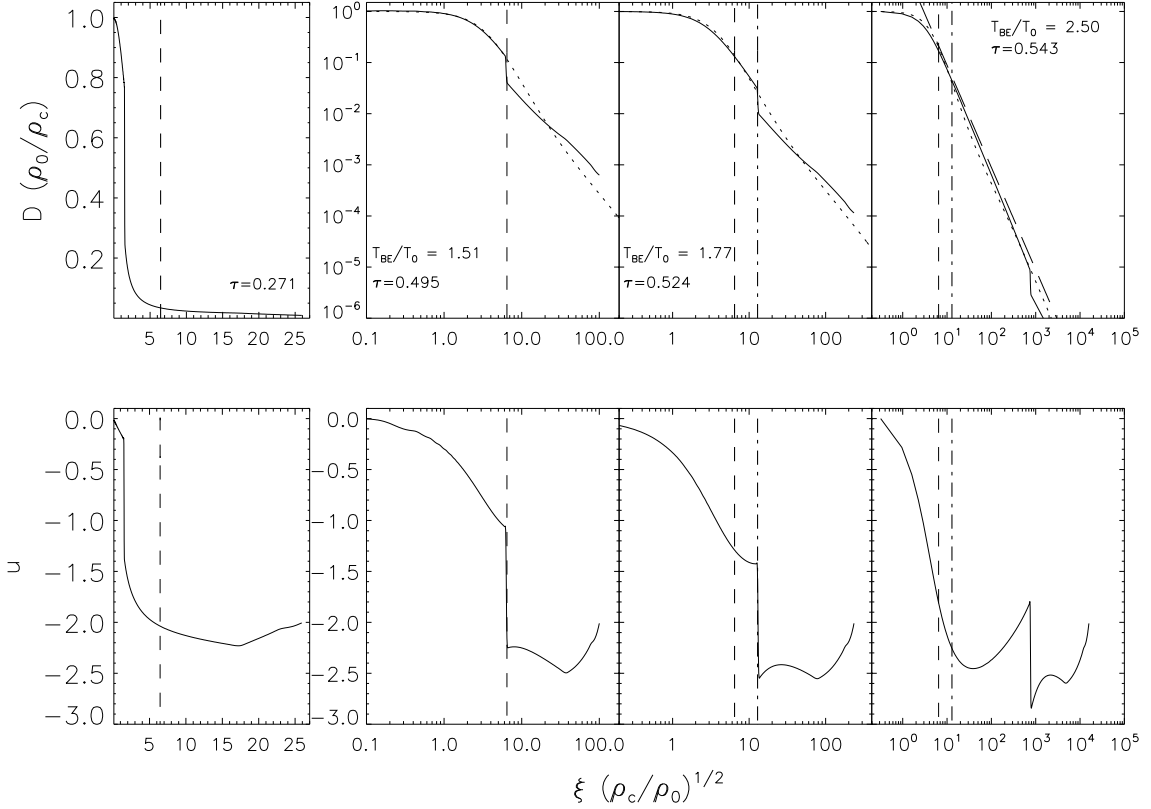
Figure 2.3: Same as Figure 2.2, for inflow Mach number $\mathscr{M} = 2.0$.

Note that the density and velocity profiles of the regions outside of the shock go through a transient evolution after simulations begin. The density profile evolves from a uniform profile set in the initial condition to a $\rho \propto r^{-2}$ profile consistent with supersonic radial inflow the material is also increasingly accelerated by gravity. Note that for supersonic radial flow, $v \sim const.$ upstream of the shock combines with the steady state mass inflow condition $\rho v r^2 = const.$ to yield $\rho \propto r^{-2}$; In Figures 2.2 - 2.5, the inflection feature in the velocity profiles exterior to the shock corresponds to a wave propagating inward at
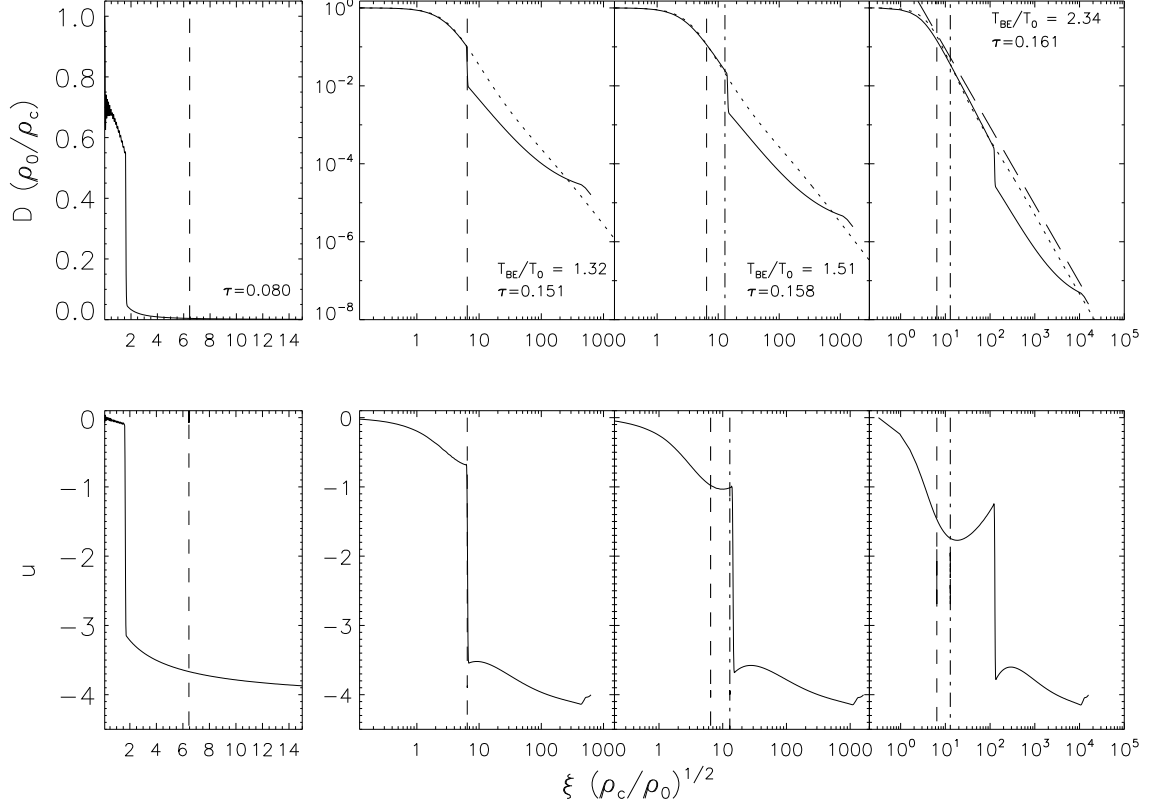
Figure 2.4: Same as Figure 2.2, for inflow Mach number $\mathcal{M} = 4.0$.

a speed equal to the inflow speed plus the sound speed.

Since post-shock velocities are subsonic, gravitational instability is expected to develop at a point when the radius of the inner dense post-shock region becomes comparable to the critical radius of a BE sphere. This expectation is indeed borne out by our simulations, which moreover show that the properties of the collapsing dense inner region are similar as those of collapsing cores initialized from hydrostatic BE spheres. The collapse follows an "outside-in" pattern, starting from the shock front. The central density increases dramatically and the inflow velocity inside the shock becomes supersonic. The collapse propagates inward and establishes a centrally concentrated density profile (Hunter 1977; Larson 1969; Penston 1969; Shu 1977), which approaches the LP density profile $D(\xi) = 8.86\xi^{-2}$, and the velocity approaches $-3.28a$.

The three panels on the right of Figures 2.2 - 2.5 show the density profile (top) and
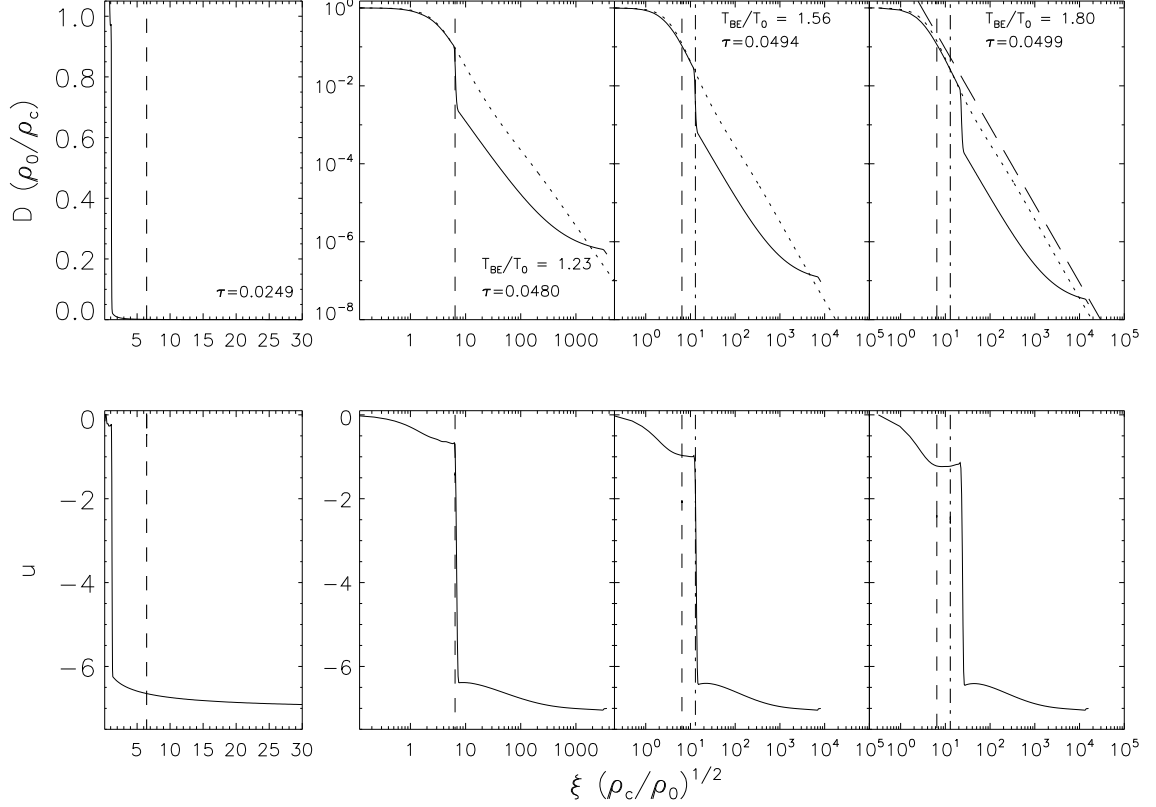
Figure 2.5: Same as Figure 2.2, for inflow Mach number $\mathcal{M} = 7.0$.

the velocity profile (bottom) at three different instants during the outside-in collapse. The density profiles plotted are normalized by the central density and the interior regions are fit by BE sphere density profiles. That is, we match solutions of the density profile inside the shock to solutions of the hydrostatic equation $\frac{d\ln D}{d\xi} = -\frac{m(\xi)}{\xi^2}$ with a fitted temperature T_{BE}. These fits are further discussed below. The ratio between the fitted BE sphere temperature T_{BE} and the true temperature T_0 is also noted in the figures. The first figure of these three shows profiles at the instant when the radius of the post-shock region reaches the critical radius (see Equation 2.18) of a BE sphere at temperature T_0 with the same central density, i.e., $r_{shock} = R_{BE,crit}$. We define the period after this as the supercritical regime. The center-to-edge density ratio after this point exceeds ~ 10. The second figure of these three shows the instant when the radius of the post-shock region reaches twice the critical radius of a BE sphere. The third figure is at the instant of core–collapse τ_{coll} (defined

34

here as $\rho_c/\rho_0 = 4 \times 10^7$). The long dashed diagonal line in the third figure shows the LP density profile, which is very close to the numerical solution. The time interval between $r_{\text{shock}} = R_{\text{BE,crit}}$ and collapse for the $\mathcal{M} = 2$ case in code units is 0.048 (see Equation 2.12), which corresponds to 1.1×10^5 yr if the inflowing ambient medium's density is $n_H = 100\,\text{cm}^{-3}$.

We note that prior to collapse, the velocities in the dense gas (inside the shock) remain small. In particular, for $\mathcal{M} \geq 2$ cases, the inflow velocity inside the shock is subsonic throughout the post-shock region before the time when $r_{\text{shock}} = R_{\text{BE,crit}}$. When $\mathcal{M}$ is high, Figures 2.4 and 2.5 show that the post-shock velocities remain subsonic until shortly before the instant of collapse.

The outward propagation speed of the shock, which from the simulations is approximately constant (Figure 2.6) at early time, can be obtained using the shock jump conditions. If the shock position is $\xi_{\text{sh}} = u_{\text{sh}}\tau$, then provided equation (2.21) is satisfied, the velocity on the downstream side is

$$u_d = \frac{\tau u_{\text{sh}}}{\tau - \tau_0}. \tag{2.22}$$

Note that in order for the downstream velocity to be inward and the shock to be propagating away from the origin, we must have $\tau < \tau_0$. The isothermal shock jump conditions, with subscript "u" denoting upstream and "d" downstream values, are $D_d(u_d - u_{\text{sh}}) = D_u(u_u - u_{\text{sh}})$ and $D_d[1 + (u_d - u_{\text{sh}})^2] = D_u[1 + (u_u - u_{\text{sh}})^2]$; together these imply $D_d/D_u = (u_u - u_{\text{sh}})^2$ and $(u_d - u_{\text{sh}})(u_u - u_{\text{sh}}) = 1$. Treating the shock speed as approximately constant so that Equation (2.22) holds, we can solve for the shock velocity to obtain $u_{\text{sh}} = \frac{1}{2}(u_u + [u_u^2 + 4 - 4(\tau/\tau_0)]^{1/2})$. For $\tau/\tau_0 \ll 1$, and taking the upstream velocity as $u_u \approx -\mathcal{M}$ which corresponds to the limit of strongly supersonic inflow, gives

$$u_{\text{sh}} \approx \frac{1}{2}\left[-\mathcal{M} + (\mathcal{M}^2 + 4)^{1/2}\right] = \frac{2}{\mathcal{M} + (\mathcal{M}^2 + 4)^{1/2}}. \tag{2.23}$$

The shock speed decreases as the Mach number increases, and therefore from equation

35

(2.22) the post-shock flow speed also decreases as the Mach number increases. Figure 2.6 shows the position of shock front versus time for $\mathcal{M} = 4$. The intercept and the slope are based on the best fit of the linear part where $\tau \in [0.0, 0.04]$. The intercept is nearly 0 and the slope 0.3061 is the measured shock speed in units of the isothermal sound speed a; equation (2.23) predicts a slightly smaller value 0.24. The analytical solution (Equation 2.23) for u_{sh} as a function of $\mathcal{M}$ is plotted as a dotted line in Figure 2.7 (labeled as $u_{\mathrm{sh,estimate}}$) and the shock speeds directly measured from simulations u_{sh} are plotted as asterisks. The analytical approximation is about 15%-28% below the measured value from the simulations as $\mathcal{M}$ ranges from 1.05 to 7.0.
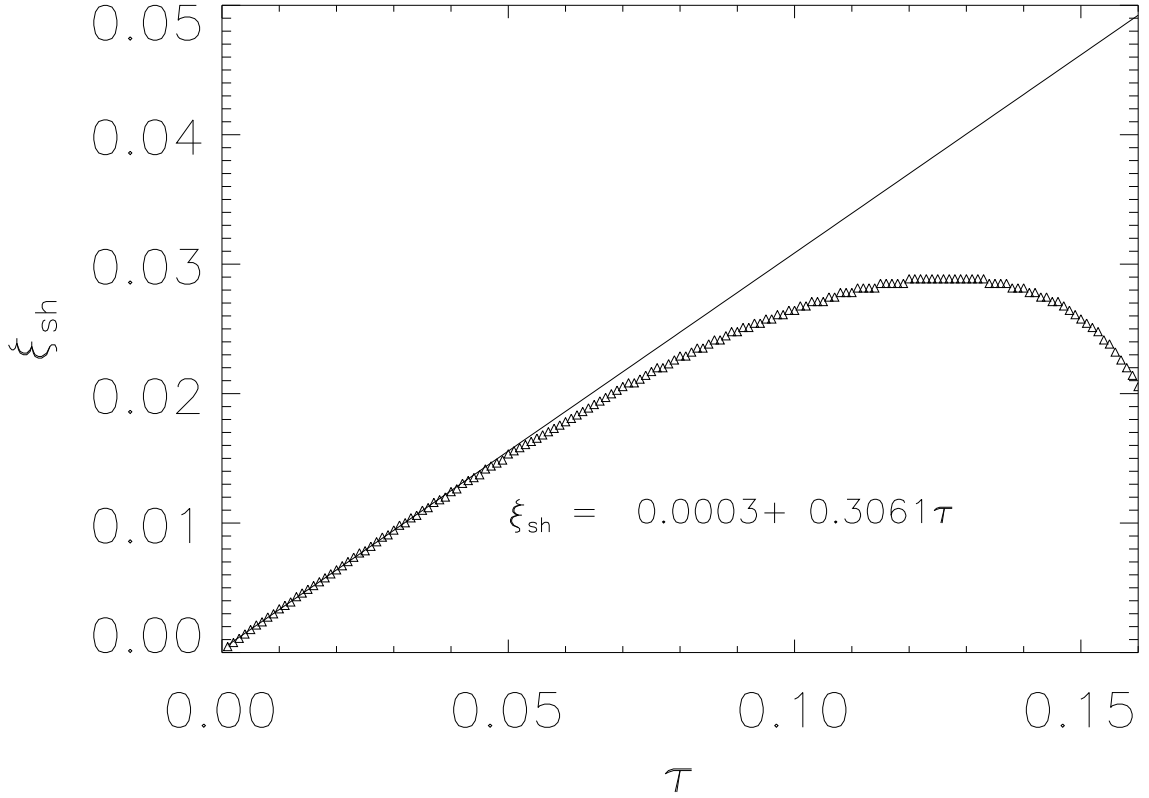
Figure 2.6: The shock front position versus time for $\mathcal{M} = 4$. The solid line is the best fit to the linear part, i.e., a constant-speed outward- propagating shock at early times. Collapse occurs for this model at $\tau_{\mathrm{coll}} = 0.16$.

Using the constant-shock-speed approximation, the immediate post-shock density can also be obtained in terms of the pre-shock density, in the limit $\tau/\tau_0 \ll 1$ and using $u_u \approx$

$-\mathcal{M}$ as:

$$\frac{D_d}{D_u} = \frac{1}{4}\left[\mathcal{M} + (\mathcal{M}^2 + 4)^{1/2}\right]^2, \qquad (2.24)$$

which for $\mathcal{M} \gg 1$ is $D_d/D_u \approx \mathcal{M}^2$. Because of the radial convergence of the inflow in the simulations, D_u varies; it is initially equal to 1, but after an initial transient, in the highly supersonic limit D_u would approach $(\xi_{\mathrm{outer}}/\xi_{\mathrm{sh}})^2$ because of mass conservation.
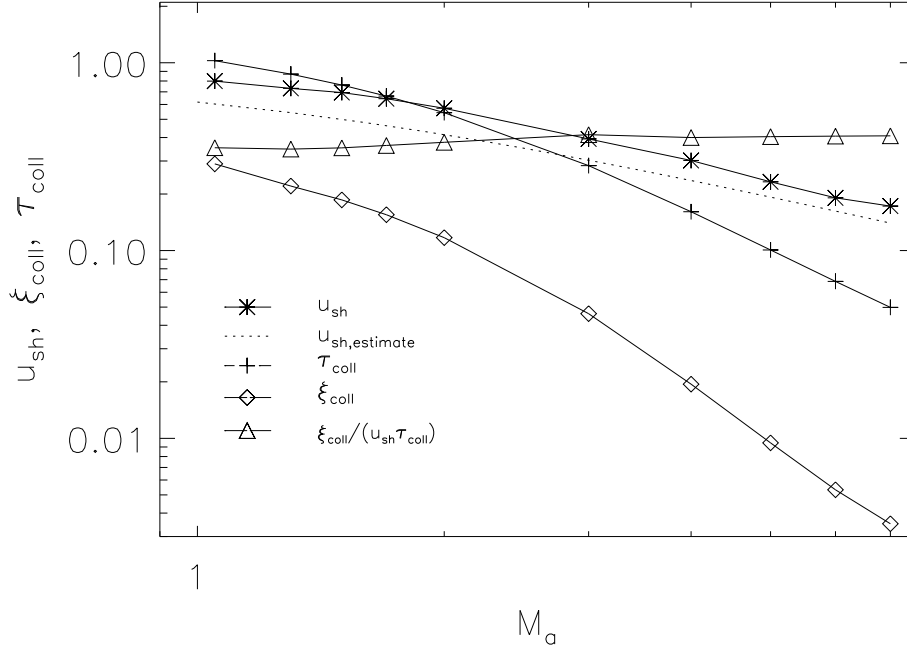
Figure 2.7: The speed of shock front at early times (asterisks), the radius of the core at the instant of collapse (diamonds), and the time at which collapse occurs (plus signs) as a function of $\mathcal{M}$. Triangles show the ratio of $\xi_{\mathrm{coll}}/(u_{\mathrm{sh}}\tau_{\mathrm{coll}})$, which is nearly constant, ranging from 0.34 to 0.42. The dotted line is the analytic estimate for u_{sh} given in equation (2.23).

It is interesting to investigate how the state of the core when it collapses depends on Mach number. Figure 2.8 shows the density profiles and the velocity profiles of the simulated cores at the instant of collapse τ_{coll}, for different Mach numbers. First, it is clear that all the density profiles approach the LP solution, especially for low Mach number cases. The inflow velocity inside the shock is supersonic and does not strongly vary over the dense core region. The smaller the Mach number is, the closer the inflow speed is to the LP result, $v = -3.3a$. Second, the radius of the core at the instant of collapse decreases
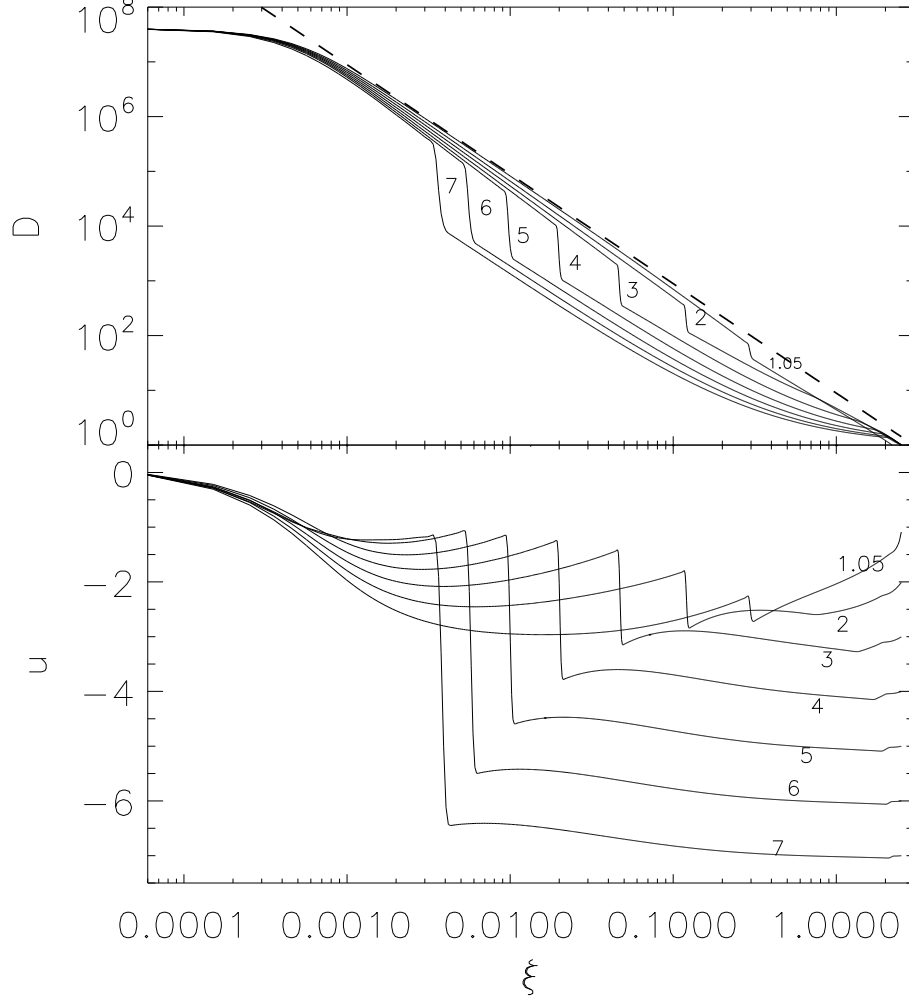
Figure 2.8: The density profiles (top panel) and the velocity profiles (bottom panel) at the instant of collapse for simulations with different Mach number $\mathcal{M}$ (as labeled). The thick dashed line in the top panel is the LP density profile $D = 8.86\xi^{-2}$. For higher $\mathcal{M}$ cases, the shock front is at smaller radius (in units of r_0) and the post-shock speeds in the dense core are lower in magnitude. Units of length and velocity are given by equations (2.13) and (2.11), respectively. Density is in units of the GMC ambient value.

as Mach number increases. We plot this dependence in Figure 2.7 with diamonds.

We quantitatively compare the basic core properties in Figure 2.7, which shows the collapse time τ_{coll} and the shock radius ξ_{coll} at time τ_{coll}, both as function of $\mathcal{M}$. As noted above, ξ_{coll} decreases with increasing $\mathcal{M}$; the same is true for τ_{coll}. We also recall that u_{sh} decreases with $\mathcal{M}$. Interestingly, while $\xi_{\mathrm{coll}}, u_{\mathrm{sh}}$, and τ_{coll} all decrease with $\mathcal{M}$, the ratio $\xi_{\mathrm{coll}}/(u_{\mathrm{sh}}\tau_{\mathrm{coll}})$ is nearly constant with $\mathcal{M}$: it ranges only from 0.34 to 0.42 (see

Figure 2.7). This result is potentially useful for empirical estimates of core lifetimes, since the inflow velocity $\mathcal{M}$, the isothermal sound speed a and the radius of dense core are all in principle measurable. If the ratio $\xi_{coll}/(u_{sh}\tau_{coll})$ is taken as a constant ≈ 0.4, and the shock speed is estimated via equation (2.23), then the life time of cores up to the point of collapse is given in dimensional form by $t_{coll} \approx 1.3R_{coll}[\mathcal{M}+(\mathcal{M}^2+4)^{1/2}]/a$. In practice, it may be difficult to measure $\mathcal{M}$ outside of a core, because the density is much lower than that of the core, and it is difficult to isolate the immediate environment of the core from foreground and background gas. This result is still useful in a statistical sense, however, using the mean Mach number of the turbulent flow in a cloud.
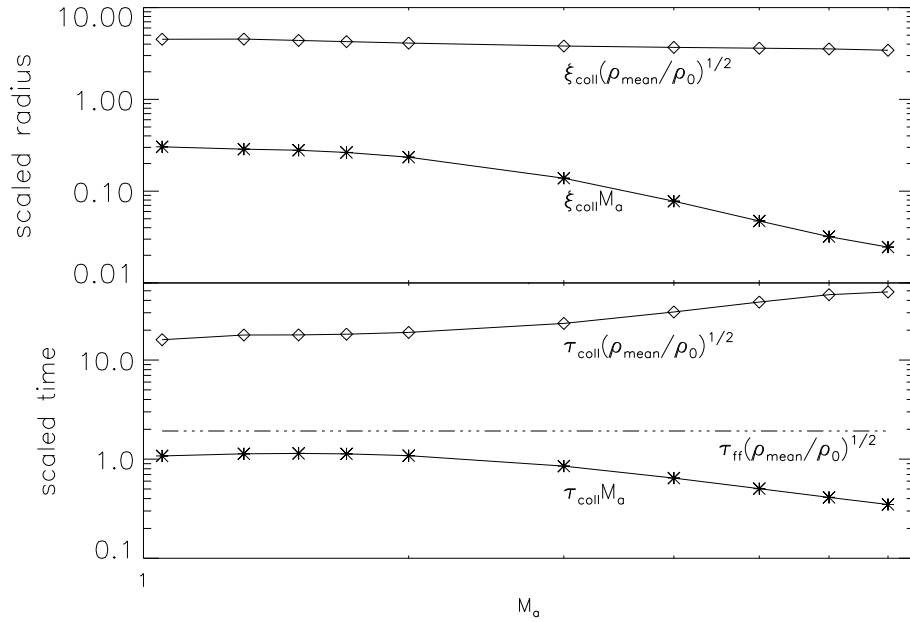
Figure 2.9: The renormalized radius (top panel) and collapse time (bottom panel) of cores versus $\mathcal{M}$. Diamonds show quantities normalized using the mean core density and asterisks show quantities normalized using the Mach number (see text). The dot-dashed line in the lower panel shows the free fall time at density ρ_{mean} in units $(4\pi G\rho_{mean})^{1/2}$, i.e., $\tau_{ff}(\rho_{mean}/\rho_0)^{1/2} = \pi(3/8)^{1/2}$.

Another direct observable is the core density, so it is interesting to test how the values of the collapse time and radius depend on the mean density in the core at the time of collapse. Diamonds in the top panel of Figure 2.9 show the core radius in units of $a(4\pi G\rho_{mean})^{-1/2}$, which is $\xi_{coll}(\rho_{mean}/\rho_0)^{1/2}$, as a function of $\mathcal{M}$. We can see

$\xi_{coll}(\rho_{mean}/\rho_0)^{1/2}$ is nearly constant, ranging from 4.58 to 3.42 as Mach number increases from 1.05 to 7. Taking this as approximately constant, and using the measured core mean density, the predicted size of core at the time of collapse is $R_{coll} \approx 4a(4\pi G\rho_{mean})^{-1/2}$. Note that this radius is $\sim 50\%$ larger than the critical BE radius for the same temperature (see Equation 2.18). Since the post-shock density increases relative to the upstream density approximately as $D_d/D_u \sim \mathcal{M}^2$ (see Equation 2.24), it is also interesting to test how $\xi_{coll}\mathcal{M}$ depends on Mach number. In fact this quantity decreases with $\mathcal{M}$, as seen in Figure 2.9.

To express the core–collapse time in terms of observables, we normalize the collapse time using the mean core density. This quantity $t_{coll}(4\pi G\rho_{mean})^{1/2} = \tau_{coll}(\rho_{mean}/\rho_0)^{1/2}$, is plotted in Figure 2.9 as a function of $\mathcal{M}$. For reference, the core collapse time normalized using $\mathcal{M}$ is also plotted in Figure 2.9. The free-fall time t_{ff} for a uniform sphere in units of $(4\pi G\rho_{mean})^{-1/2}$ is 1.92, so that we have $t_{coll} \sim 8 - 26\,t_{ff}$ as Mach number varies from 1.05 to 7. This time scale is much longer than the observed values $\sim 2 - 5\,t_{ff}$ for prestellar cores. The reason for this disparity is that during the early part of its evolution, the central density of the core is low, and it would not be identifiable within its surroundings. This is evident in the low contrast between the center and the edge of the core seen in the first frames of Figure 2.2 - 2.5. Only when the core approaches collapse does the center-to-edge contrast become large. For example, for the $\mathcal{M} = 1.05$ model, the center-to-edge density ratio ρ_c/ρ_{edge} reaches 2 at $\tau = 0.78$ and reaches 5 at $\tau = 0.92$; this can be compared with the total time until collapse, $\tau_{coll} = 1.027$ for this model. For the whole set of models, the observable fraction of the pre-collapse core life is 30%-50% if we choose $\rho_c/\rho_{edge} \geq 2$, or 10%-20% if we choose $\rho_c/\rho_{edge} \geq 5$. Taking the period when $\rho_c/\rho_{edge} \geq 2$ or $\rho_c/\rho_{edge} \geq 5$ as the period over which a core could be observable, e.g., in submilimeter continuum, our simulations give $t_{observable} \sim 2 - 13\,t_{ff}$ or $t_{observable} \sim 1 - 6\,t_{ff}$, respectively. The latter is consistent with observed estimates.

Another observable aspect of prestellar cores is their density structure. As discussed above, for each solution at the times shown in Figure 2.2 - 2.5, we fit a BE sphere profile. The density in code units ρ_0 is $D(\xi) = \rho/\rho_0$ and the radius in code units is $\xi = r(4\pi G\rho_0)^{1/2}/a$. When the central density is instead used to normalize, the density and radius variables are:

$$\widetilde{D} = \rho/\rho_c = D\rho_0/\rho_c \tag{2.25}$$

and

$$\widetilde{\xi} = r\frac{(4\pi G\rho_c)^{1/2}}{a} = \xi(\rho_c/\rho_0)^{1/2}. \tag{2.26}$$

For a BE sphere with sound speed a_{BE}, the density profile normalized by the central density is $\widetilde{D}_{\mathrm{BE}}$, which is a function of the scaled radius $\xi_{\mathrm{BE}} = r(4\pi G\rho_c)^{1/2}/a_{\mathrm{BE}} = \widetilde{\xi}\, a/a_{\mathrm{BE}}$. To fit the density profiles in our simulations to a BE sphere, the only free parameter is the ratio of the isothermal sound speed a_{BE} of the BE sphere to the sound speed in the simulations, a. Thus, for any given density profile $\widetilde{D}$ we adjust the value of a_{BE}/a until a good match between $\widetilde{D}_{\mathrm{BE}}$ and $\widetilde{D}$ is obtained. This procedure yields the fitted temperature ratio:

$$\frac{T_{\mathrm{BE}}}{T_0} = \left(\frac{a_{\mathrm{BE}}}{a}\right)^2. \tag{2.27}$$

The values obtained for T_{BE}/T_0 are marked in Figures 2.2 - 2.5. The range of values we find is 1.23–2.89. This range is consistent with theoretical expectations. As the radius of the BE sphere extends to infinity, the density profile approaches the singular solution $\rho = 2a_{\mathrm{BE}}^2/(4\pi Gr^2)$ (Shu 1977) corresponding to $\widetilde{D}_{\mathrm{BE}} = \rho/\rho_c = 2(a_{\mathrm{BE}}/a)^2\widetilde{\xi}^{-2}$. The density profile of the collapsed core approaches the LP solution $\widetilde{D} = 8.86\widetilde{\xi}^{-2}$. To match the LP profile with the singular profile therefore requires $2(a_{\mathrm{BE}}/a)^2 = 8.86$, which corresponds to a temperature ratio $T_{\mathrm{BE}}/T_0 = 8.86/2 = 4.43$. Fits of core profiles to BE spheres that indicate values of T_{BE} up to 4.43 times the measured thermal temperature therefore are expected if collapse has taken place; this does not by itself indicate that magnetic support is present.

2.4.2 Post-Collapse Evolution: Infall and Accretion Stages

After the central density becomes singular, the evolution transitions to the infall and accretion stages. For our simulations, we make this transition by implementing an outflow boundary condition at the center when the central density reaches $4 \times 10^7 \rho_0$. The initial mass of the central protostar is calculated by integrating the innermost part of the density profile where density is between $[1 \times 10^7, 4 \times 10^7] \rho_0$. The specific choice of this density does not significantly affect τ_{coll}, ξ_{coll}, or the subsequent evolution since the central density increases dramatically only at the very end of the collapse stage.

At the beginning of the accretion phase, the material inside the shock falls onto the protostar. The material approaching the protostar is in a free-fall state (Hunter 1977). The region of unsupported infall starts from the center and propagates outward, similar to the "expansion wave" described by Shu (1977). The density profile inside the rarefaction wave changes from $\rho \propto r^{-2}$ to $r^{-3/2}$ and the velocity profile changes from $v \propto r^0$ to $r^{-1/2}$. For our simulations, this infall stage ends as the infall rarefaction wave arrives at the shock front. This generally occurs very rapidly (in less than 10% of τ_{coll}; see below).

For an initially static density profile Ar^{-2}, where $A = Ka^2/(4\pi G)$ and K is a constant, if the gas pressure is negligible the average speed of the rarefaction wave is $(2\sqrt{2K}/\pi) a$. For $K = 8.86$, which is the LP profile, this yields $2.7a$. For the real case, the initial velocity is nonzero and the gas pressure is non negligible, so that the rarefaction wave propagates at a modified speed. For example, for the $\mathcal{M} = 1.05$ model, which has $\xi_{\mathrm{coll}} = 0.29$ and infall interval $\Delta\tau_{\mathrm{inf}} = 0.092$, the average speed is $3.15a$. For $\mathcal{M} = 4.0$ and 7.0, the measured average infall speed of the infall rarefaction wave is $2.22a$ and $1.95a$, respectively.

After the infall rarefaction wave arrives at the shock front, the final accretion stage begins, with material initially outside the shock falling onto the protostar at supersonic speeds. This process is similar to Bondi accretion, except that the central mass is growing

and the velocity field for our simulations is uniformly converging at large distance. During this stage, the density and the velocity profiles vary $\propto r^{-3/2}$ and $r^{-1/2}$, respectively, corresponding to free fall.

The typical density profiles and velocity profiles during the accretion stage for $\mathscr{M} = 1.05$ and 4 models are shown in Figure 2.10. Three different instants in the evolution are shown: the instant of core collapse, the instant when the infall rarefaction wave arrives at the shock front, and a point during the late accretion stage. The transition from the LP profiles to the free–fall profiles in density and velocity are clearly evident in the figure.
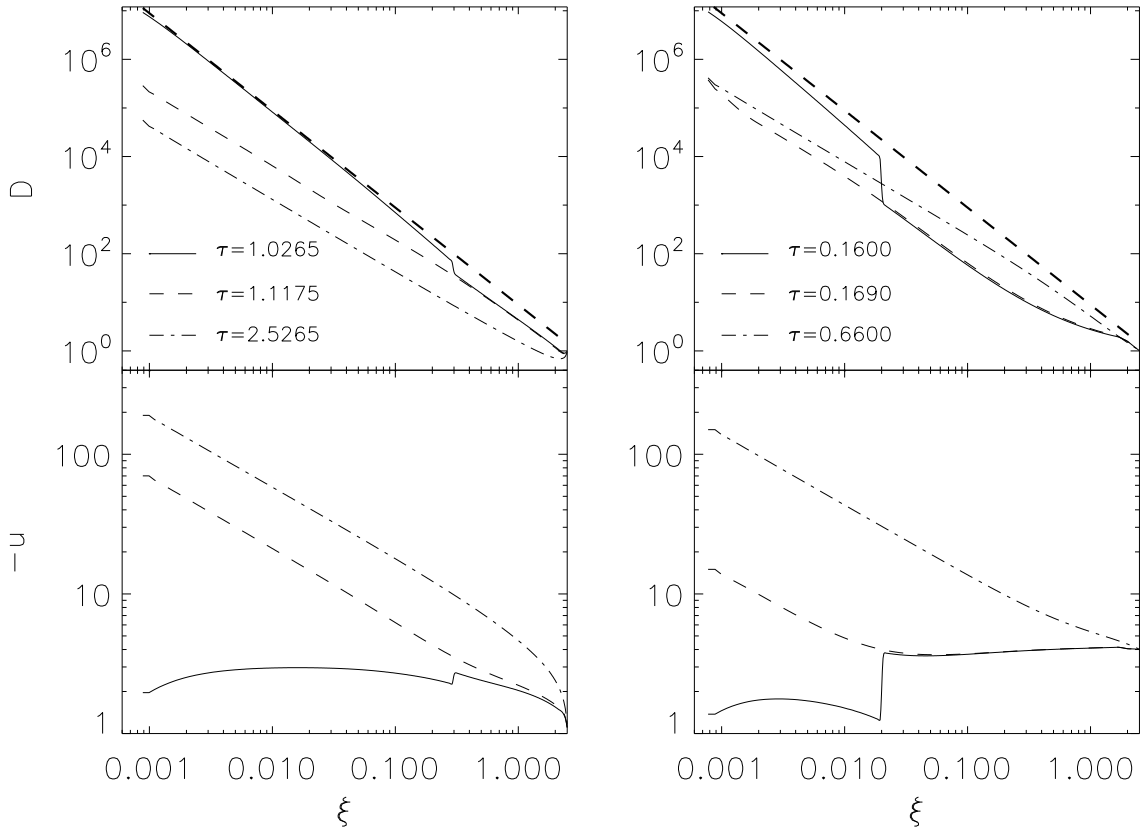
Figure 2.10: The density and velocity profiles during the accretion phase for $\mathscr{M} = 1.05$ (left) and $\mathscr{M} = 4$ (right) models. Density profiles (top) and the velocity profiles (bottom) are each shown at three different instants: solid lines show the instant of core collapse, dashed lines show the instant when the gravitational rarefaction wave arrives at the shock front, and dot-dashed lines show the profiles at a late accretion stage. Numbers in the figure show the corresponding time for each instant. In the upper panels, the LP density profile $D = 8.86\xi^{-2}$ is plotted for reference with thick dashed lines. The transitions from $D \propto \xi^{-2}$ (early) to $D \propto \xi^{-3/2}$ (late) and $u \propto \xi^0$ (early) to $u \propto \xi^{-1/2}$ (late) are evident.

43

In a real system, the duration of the accretion stage depends on the environment of the protostar, and how long the inflow that creates the core is maintained at large scales. To explore how the late-time evolution is affected by changes in the accretion, we have conducted additional simulations in which the flow inward from the outer boundary is halted at the end of the infall stage (i.e., when the rarefaction reaches the shock). Suppression of inflow will affect the mass flux onto the protostar after the rarefaction wave from the boundary reaches the central protostar. We discuss comparison of these models to our standard models in Section 4.4.

2.4.3 Definition of Evolutionary Stages

Based on the results presented in Sections 4.1 and 4.2, we have identified four main stages of protostellar core formation and evolution in a supersonic turbulent medium (see Figure 2.11 for a schematic depiction).

1. *Core building —*

Converging flows in a supersonic turbulent medium collide, with post-shock compressed gas accumulating over time in stagnant, shock-bounded regions. If these dense regions are not destroyed by larger– scale turbulence, the high–density gas will undergo a long contraction process during which gas pressure competes with self-gravity. The typical character of this stage is that the velocity inside the dense gas is subsonic and increases linearly with distance from the center. Since the center-to-edge density contrast is relatively low, these clumps are gravitationally subcritical. Towards the end of this stage, when the center-to-edge density contrast becomes appreciable, these objects would become observable as prestellar cores. This core–building stage lasts $> 90\%$ of τ_{coll}; only the last 10%-20% would be observable.

2.*Core collapse —*

The core built up during the first stage accumulates enough mass that it becomes grav-

itationally supercritical, which we operationally define as $r_{\text{shock}} > R_{\text{BE,crit}}$. Self-gravity overwhelms the gas pressure, and the unstable core starts to collapse. The collapse begins near the shock front, where the imbalance between gravity and pressure gradient forces is greatest, and propagates inward. This collapse is an "outside-in" process. During core collapse, the central density increases dramatically and the inflow velocity inside the core becomes supersonic. As the collapse propagates inward, a density profile $\rho \propto r^{-2}$ is left behind and the velocity increases toward the center. The end of this stage is defined by the instant of protostar formation τ_{coll}, when the wave of collapse has reached the center of the core. The density profile approaches the LP profile, $\rho = 8.86a^2/(4\pi G r^2)$. The velocity in the interior of the collapsed core approaches a uniform value comparable to that in the LP solution $-3.28a$. The central density is high enough to be optically thick and a protostar forms. Because of their large central volume densities, prestellar cores during this collapse stage would be observed as having high peak submillimeter flux densities. This stage lasts for a time $\Delta\tau_{\text{supcrit}}$, less than 10% of the prestellar core lifetime τ_{coll}.

3. *Envelope infall —*

During this stage, the high–density material inside the shock front falls to the protostar (or, if angular momentum was included, a circumstellar disk). This stage starts at the instant of the protostar formation and ends at the instant when the gravitational rarefaction wave reaches the shock front, clearing out the remnants of the dense gas that accumulated during core building. During this stage, the density and velocity profiles in the interior change from LP profiles to free fall profiles. Since the core contains an embedded protostar, the system would be observationally classified as Class 0/I. This stage lasts for a time Δt_{inf} less than 10% of the prestellar core lifetime. In a real system, the fraction of the envelope mass that eventually reaches the center would depend on the details of the protostellar wind, which would sweep up at least the polar portion of the envelope, creating an outflow.

45
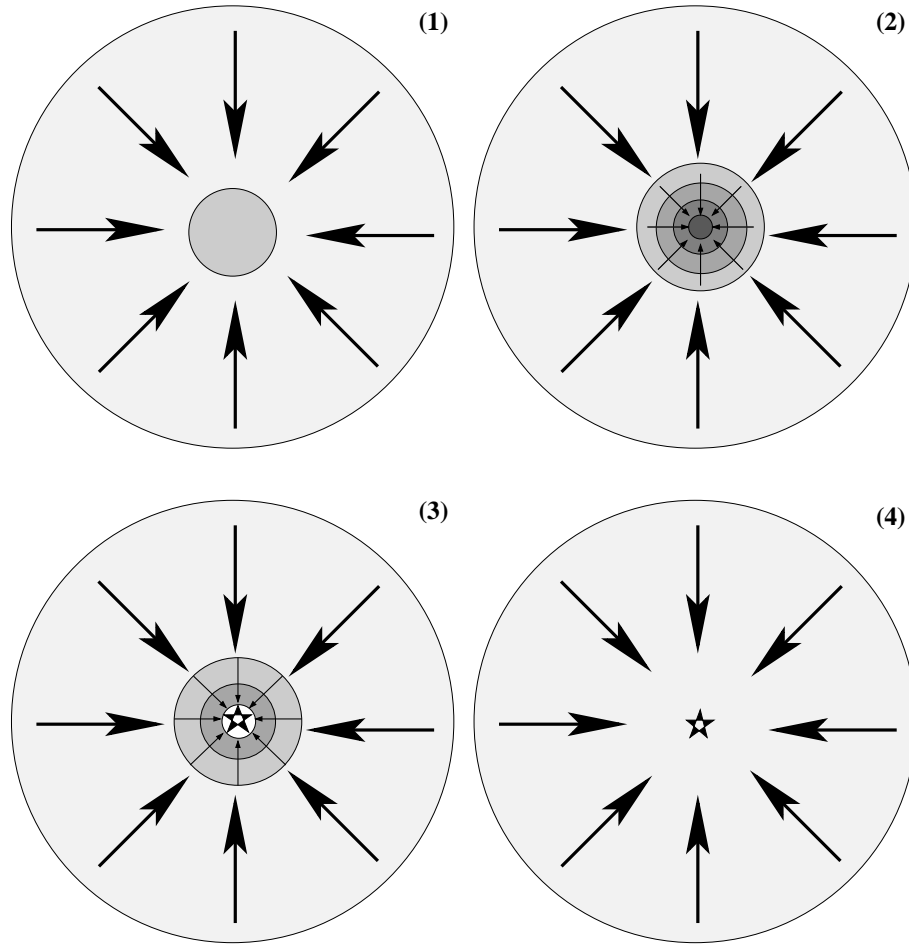
Figure 2.11: The four stages of core evolution in the idealized models of this chapter. (1) Core building via supersonic converging flow, yielding a stagnant, shock-bounded dense region. (2) Core collapse, propagating from outside to inside, leading to a density profile $\rho \propto r^{-2}$. (3) Envelope infall, propagating from inside to outside, and resulting in free fall onto the protostar. (4) Late accretion of ambient gas onto the protostar. For real systems, evolution would be modified in several ways: converging flows would be non-spherical, angular momentum would lead to disk formation, and outflows would contribute to clearing the envelope.

4. *Late accretion* —

During this stage, material from the ambient environment directly accretes to the protostar (or, more realistically, a disk). Accretion during this stage is similar to Bondi accretion, with free-falling density and velocity profiles $\rho \propto r^{-3/2}$ and $v \propto r^{-1/2}$ over the whole core region. For a real system, the duration of the late accretion stage, and hence the final stellar mass, depends on ambient conditions far from the protostar. In a real sys-

tem, the potential of this stage to contribute significantly to the stellar mass would also depend on protostellar winds, which can reverse the accretion.
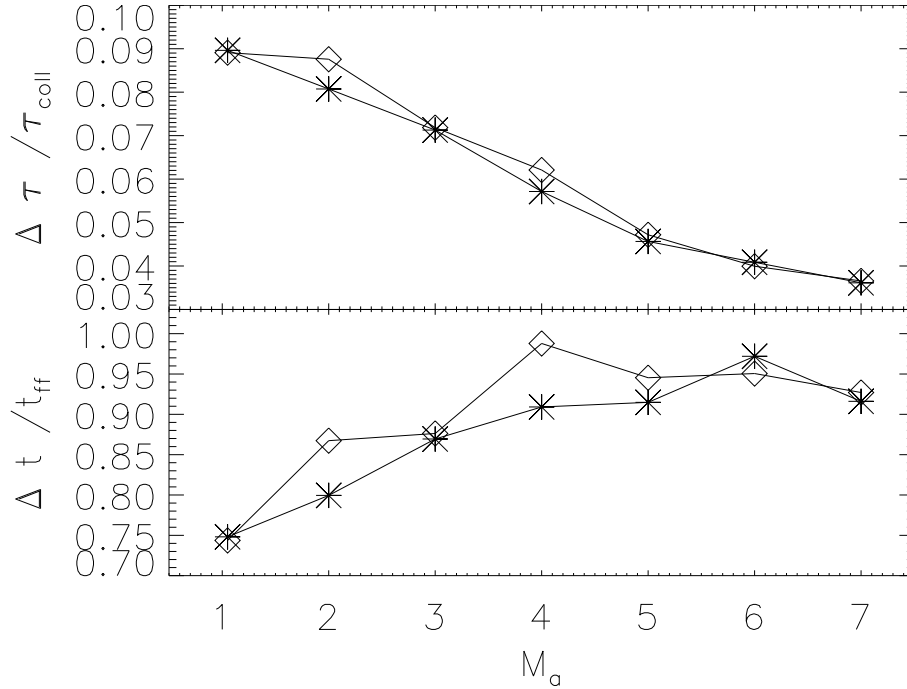
Figure 2.12: Top panel shows the ratio of the duration of the supercritical collapsing stage $\Delta\tau_{supcrit}$ (asterisks) and the post-collapse infall stage $\Delta\tau_{inf}$ (diamonds) to the prestellar lifetime τ_{coll} of cores, as a function of Mach number. Bottom panel shows ratios $\Delta t_{supcrit}/t_{ff}$ (diamonds) and $\Delta t_{inf}/t_{ff}$ (asterisks), which range from [0.8, 1], as a function of Mach number; here t_{ff} is computed using the mean density inside the shock at τ_{coll}.

Although we have identified these stages based on idealized spherically symmetric models with constant gaseous inflow rates at large distance, we expect that the same stages would be present, in modified form, under more realistic conditions. Based on our simulations, the ratios $\Delta\tau_{supcrit}/\tau_{coll}$ and $\Delta\tau_{inf}/\tau_{coll}$ decrease with increasing $\mathcal{M}$, as shown in Figure 2.12. The supercritical stage and the infall stage have similar durations, and range from 9%-3% of the prestellar core lifetime t_{coll}, which itself ranges from 8 to 26 t_{ff}. The supercritical collapse period (stage 2) $\Delta t_{supcrit}$ and the infall period (stage 3) Δt_{inf} thus both range over $\sim 0.8 - 1 t_{ff}$, as shown in Figure 2.12. While the time to reach collapse would differ for nonspherical or nonsteady converging large-scale flows, we expect that the character of the evolution would not. We also expect that the ratios

$\Delta t_{\mathrm{supcrit}}/t_{\mathrm{ff}}$ and $\Delta t_{\mathrm{inf}}/t_{\mathrm{ff}}$ would remain order-unity.

2.4.4   Evolution of Mass Accretion Rates
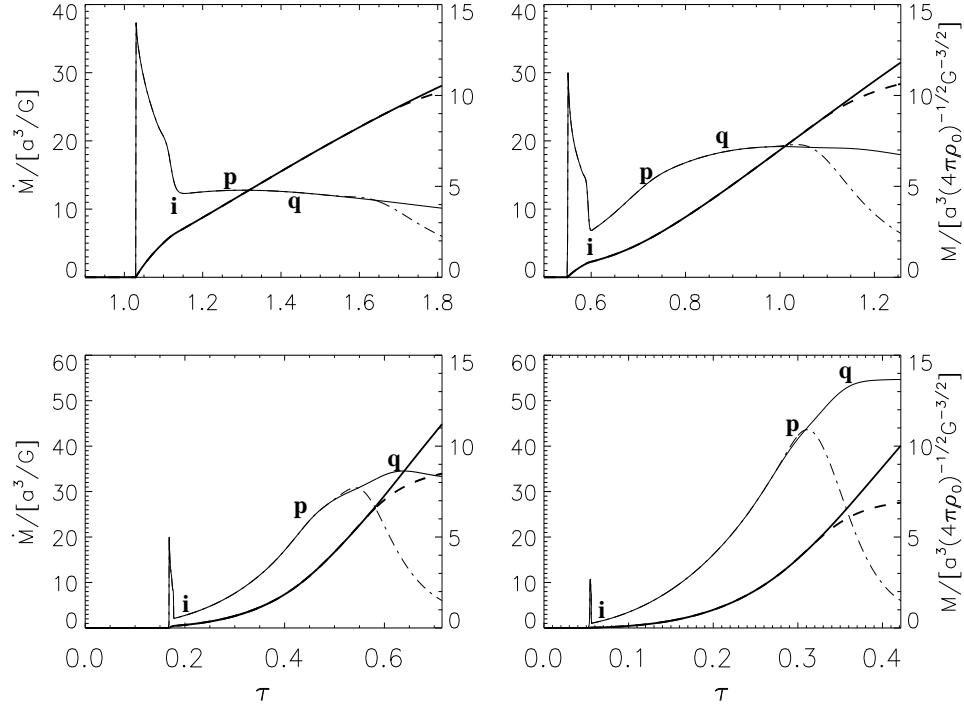
Figure 2.13: Temporal evolution of the mass accretion rate (thin solid lines; left axis) and the integrated mass of protostar (thick solid line; right axis) for models with Mach number $\mathcal{M} = 1.05, 2, 4$ and 7, as labeled. The corresponding dot-dashed lines show the results for models in which the inflow to the grid is suppressed after the end of the infall stage. The point marked i represents the end of the infall stage, p represents the instant when the density profile reaches $\rho \propto r^{-3/2}$ everywhere, q represents the instant when the velocity profile reaches $v \propto r^{-1/2}$ everywhere. Units of time, mass, and accretion rate are given by equations (2.12), (2.14) and (2.3), respectively.

Figure 2.13 shows the temporal evolution of the mass accretion rate and the total integrated mass of the central protostar for $\mathcal{M} = 1.05, 2, 4$ and 7. These can be compared with the mass accretion rate and the integrated central mass for an initially static critical BE sphere, as shown in Figure 2.1 (see also Vorobyov & Basu (2005), who show similar accretion histories to Figure 2.1). For both the initially static collapse and our models that

allow for core building from supersonic flows, there is a sharp early peak in the accretion rate. The rise starting from $\dot{M} = 0$ corresponds to the moment of protostar formation at τ_{coll}. The smooth decline that follows (ending at the points marked "i" in Figure 2.13) corresponds to the infall stage, as the gravitational rarefaction wave propagates outward. At late times, however, the accretion differs for the initially static versus dynamically built cores. For an initially static unstable BE core, the late accretion steadily declines over time (Figure 2.1). In contrast, for cores formed in the $\mathcal{M} = 1.05$ model (i.e., barely supersonic inflow), the late–time accretion is nearly constant, and for cores formed in large $\mathcal{M}$ models, the late accretion rate increases over time (thin lines in Figure 2.13).

The early-time peak accretion rates can be compared with the predictions of self-similar models. For the LP profiles at the instant of core collapse, $D = 8.86\xi^{-2}$ and $u = -3.28$ give $\dot{M} = 29.1a^3/G$, while the self-similar solution for the accretion phase in Hunter (1977) predicts $\dot{M} = 46.195a^3/G$. In fact, we do see a jump in $\dot{M}$ above $29.1a^3/G$ as the evolution transits from the collapse stage to the infall stage. This phenomenon is most clearly evident for the $\mathcal{M} = 1.05$ model, which has the highest resolution of the central region because the shock strength is lower than in the high $\mathcal{M}$ models, yielding a larger core (see Figure 2.8) at the instant of collapse.

The detailed behavior of $\dot{M}$ during the late accretion stage can be understood in terms of various transitions that occur. For $\mathcal{M} = 1.05$, the accretion rate (see Figure 2.13) starts to increase from point i until to point p, and then decreases. The increases from i to p occurs as gas stored between the shock front and the outer boundary collapses into the center. The point p represents the instant when the density in the whole outer region reaches a profile $\rho \propto r^{-3/2}$. After point p, the gravitational rarefaction has reached the boundary, and subsequent accretion is limited by the inflow rate imposed at the outer boundary. For the $\mathcal{M} = 2$, 4 and 7 models shown in Figure 2.13, the mass accretion process between point i and p is similar to that of $\mathcal{M} = 1.05$. However, there is additional

transitory behavior before the accretion rate decreases to the inflow rate imposed at the boundary. At the instant corresponding to point p, the rarefaction has produced $\rho \propto r^{-3/2}$ over the whole region. But the velocity profile has $v \propto r^{-1/2}$ only over the inner region. During the stage between point p and q, the density profile stays almost unchanged but the velocity profile evolves to reach $v \propto r^{-1/2}$ everywhere (see also Figure 2.10). After point q, the accretion rate decreases to the imposed inflow rate. The stage between p and q is most obvious for the $\mathscr{M} = 4.0, 7.0$ models.

As mentioned above, we have also performed models in which inflow to the grid is halted after the point when the rarefaction reaches the shock. The resulting late-stage accretion (see Figure 2.13) is initially the same as in our standard models, but then declines over time, after the rarefaction wave reaches the boundary.
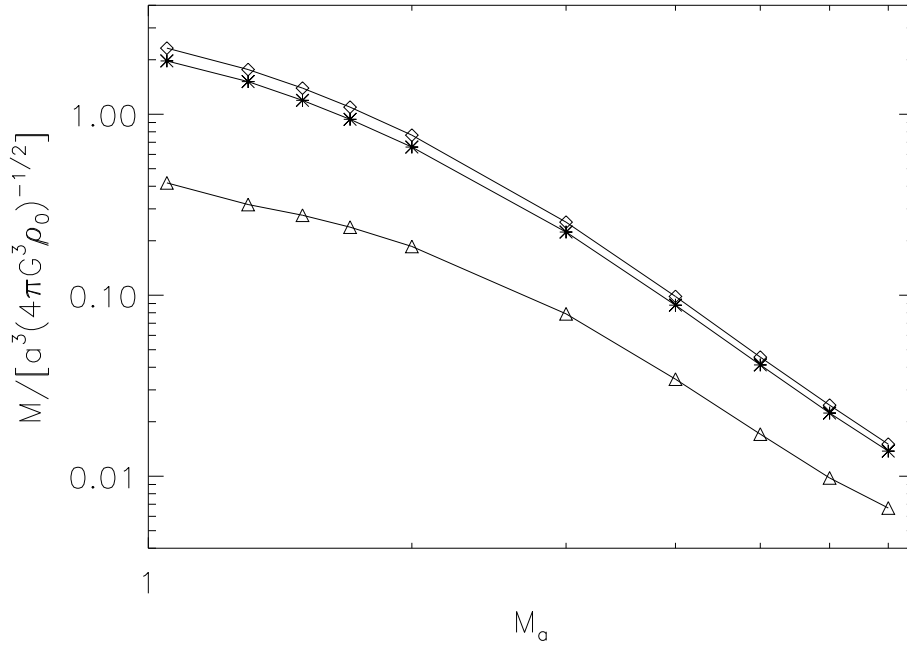
Figure 2.14: The protostellar mass at the end of the infall stage (diamonds), the core mass inside the shock at the instant τ_{coll} of protostar formation (asterisks), and the critical BE sphere mass (triangle) based on the mean core density at time τ_{coll}, all as a function of Mach number $\mathscr{M}$. The mass unit is given by equation (2.14).

The mass of the protostar at the end of the infall stage and the total core mass M_{core} inside the shock at instant of core collapse, are shown in Figure 2.14. For comparison, we

also show the critical BE sphere mass (see Equation 2.19) using the mean core density at the time of collapse for ρ_{edge}; these are lower than the actual core mass. Because there is continued mass passing through the shock during the infall stage, the post-infall protostellar mass is slightly higher than the core mass inside the shock at the time when core collapses. As the Mach number increases, the post-infall protostellar mass and the core mass at τ_{coll} both decrease. The protostellar mass ranges over $0.06 - 8.8$ M$_\odot$ and the core mass at τ_{coll} ranges over $0.05 - 7.5$ M$_\odot$, taking $n_H = 100\,\text{cm}^{-3}$ for the ambient density.

2.5   Summary and Conclusions

Star formation takes place in GMCs pervaded by supersonic turbulence, and theoretical models of prestellar (and protostellar) cores must take these large-scale supersonic flows into account. Here, we have developed models in an idealized, spherically symmetric framework that nevertheless captures key aspects of the real situation, enabling us to identify and analyze the main stages of core formation and evolution in a dynamic environment.

Our models differ from previous studies of core evolution in that the cores are not present as either stable or unstable density concentrations in our initial conditions—the initial density is everywhere uniform. Instead, during the first evolutionary stage cores are built "from scratch" by the collision of converging supersonic flows. The boundaries defining the outer edge of a core—where the density drops—correspond to a shock front across which the temperature is constant and the mass flux is nonzero. The shock front propagates outward, with the mass of the post-shock dense region growing in time. Initially, the core is essentially uniform. Over time, the mass grows sufficiently so that the core becomes centrally stratified due to self-gravity. Observationally, the latter part of this

"core– building" stage corresponds to prestellar cores that have low to intermediate peak brightness. The period over which $\rho_c/\rho_{\mathrm{edge}} \geq 5$, and a core would be clearly identifiable in observations, amounts to $1-6\ t_{\mathrm{ff}}$, with the free fall time defined using the mean core density.

When the center-to-edge density contrast exceeds ~ 10, the core becomes supercritical and a stage of violent "outside-in" collapse ensues. The density profile throughout the core approaches $\rho \propto r^{-2}$, and a protostar forms at the center. We define the instant that collapse is complete and a protostar forms as t_{coll}, or τ_{coll} in our dimensionless variables. Although the central density becomes very large, the wave of outside-in collapse still leaves most of the core mass in the outer parts. Observationally, this core–collapse stage corresponds to prestellar cores that have high peak brightness. The period $\Delta t_{\mathrm{supcrit}}$ over which cores are supercritical, undergoing outside-in collapse, amounts to less than 10% of t_{coll}, or $0.8-1\ t_{\mathrm{ff}}$.

The third stage of evolution is governed by an "inside-out" wave of gravitationally-driven rarefaction propagating from the center of the core to the shock front that defines the core's outer edge. The accretion rate onto the star during this infall stage is initially very high, but declines over time. At the end of this infall stage, the dense envelope built during the first stage has plunged into the star. The velocity and density profiles approach free fall, $v \propto r^{-1/2}$ and $\rho \propto r^{-3/2}$, respectively. Observationally, this stage corresponds to Class 0/I embedded protostars. The period Δt_{inf} over which cores undergo this inside-out infall is similar to the duration of the previous stage, $\Delta t_{\mathrm{supcrit}}$, and comparable to t_{ff}.

During the final stage of evolution, there is no longer a massive envelope. The protostar can continue to accrete from the more distant, lower-density gas in its surroundings. The late-stage accretion rate and the total mass accumulated by the system depend on the large-scale environment, rather than the properties established in the core during the building stage. Observationally, this stage corresponds to a non-embedded YSO that may

52

still be accreting from a disk.

Based on our simulations, our chief conclusions are as follows:

1. The initiation of star formation via outside-in core collapse, followed by inside-out envelope infall, appears to be very robust. The dynamical behavior during these stages of evolution is very similar whether the core is initiated as an unstable equilibrium (as in previous models) or is built up dynamically through a shocked converging flow (as in the present work). The LP singular solution with $\rho = 8.86a^2/(4\pi Gr^2)$ appears to be an "attractor," in that models initiated from stationary equilibria or with different supersonic converging velocities all arrive at this configuration at the moment of protostar formation.

2. Prior to the point at which cores become supercritical and outside-in collapse begins, the velocities interior to cores are subsonic, even if they are created by highly supersonic flows. In fact, *higher* inflow velocities from ambient gas produce *lower* post-shock velocities within the dense core (see Figures. 2–5 and Equation (23)). This result is consistent with observations showing that dense cores are quiescent in their interiors (see, e.g., André et al. 2007; Caselli et al. 2002; Goodman et al. 1998; Kirk et al. 2007; Lee et al. 2001; Myers 1983).

3. Throughout both the core-building and core-collapse stage, density profiles for cores formed by shocked converging flows can be fitted by BE profiles, but with fitted temperatures T_{BE} larger than the true temperature T_0. The range of temperatures fitted for our models with Mach numbers up to 7 is $T_{BE}/T_0 = 1.2 - 2.9$. This result is consistent with observational findings (Kandori et al. 2005; Kirk et al. 2005) that effective temperatures greater than directly measured values (from fitting spectral energy distributions (SEDs)) are usually required in order to fit BE spheres to observed prestellar cores. The largest possible ratio that could be obtained for an isothermal spherical flow is $T_{BE}/T_0 = 4.43$, so that any observed ratio larger than this suggests that magnetic fields contribute appreciable support, or else the core is anisotropic. Dapp & Basu (2009) have

also recently pointed out that the temperature fit based on matching a BE profile may be significantly higher than the true kinetic temperature, for clouds in collapsing stages.

4. At the time of collapse, for all Mach numbers the core size and mean density are closely related. We find that $R_{\mathrm{coll}} \approx 4a(4\pi G\rho_{\mathrm{mean}})^{-1/2}$ within 15% for Mach numbers $\mathcal{M} = 1.05 - 7$. This radius is $\sim 50\%$ larger than the critical radius of a BE sphere with the same mean internal density.

5. As $\mathcal{M}$ increases, and assuming a given ambient medium density ρ_0, the time to reach collapse t_{coll} is shorter, the physical size of the core at t_{coll} is smaller, the mean internal density at t_{coll} is higher, and the mass of the core at t_{coll} is lower. For high Mach number, the collapse time and collapse radius are related by $t_{\mathrm{coll}} \approx 2.6R_{\mathrm{coll}}\mathcal{M}/a$. The range of core masses at the time of collapse at different $\mathcal{M}$ is consistent with observed core masses, although the specific dependence of core mass on $\mathcal{M}$ found in the present work may be sensitive to the spherical converging-flow geometry we have adopted.

6. The durations of the collapse (supercritical) stage and the infall stage of evolution are comparable for all $\mathcal{M}$, and are close to t_{ff}. This is consistent with observations indicating similar lifetimes for prestellar cores and embedded Class 0/I accreting protostars (Beichman et al. 1986; Enoch et al. 2008; Evans et al. 2008; Hatchell et al. 2007; Jessop & Ward-Thompson 2000; Jørgensen et al. 2007; Kirk et al. 2005; Lee et al. 1999). These stages are preceded by an extended core-building stage, during most of which the core would not be observable because its center-to-edge density contrast is low.

7. The mass accretion rate onto the protostar (or, more realistically, star–disk system if angular momentum were included) peaks at the beginning of the infall stage at a value $\gg a^3/G$, and then declines steeply afterwards as the material stored in the envelope is exhausted. This result appears to hold regardless of how cores form, as it is consistent with earlier work (see, e.g., Foster & Chevalier 1993; Hennebelle et al. 2003; Motoyama & Yoshida 2003; Ogino et al. 1999; Vorobyov & Basu 2005) for cores initiated from

unstable equilibria or which undergo externally induced compression. Later accretion from the ambient medium depends on how long the large-scale cloud maintains a focused converging flow.

As noted above, some of our specific conclusions are likely to change for non-spherical geometry, and for time-dependent rather than steady large-scale inflow. Furthermore, other elements that are present in real star formation have been entirely omitted in these models; these elements include rotation, which would lead to disk formation; protostellar winds, which would sweep up and remove a portion of the envelope during the infall stage, and could prevent late accretion altogether; and magnetic fields, which would alter the timescales and details of the evolutionary stages.

We expect, however, that many of our basic results will carry over even if the idealizations we have adopted are relaxed. While large-scale supersonic converging flows in real GMCs are not generally spherical, the association of observed cores with high–density surroundings suggests that the dense gas in post-shock stagnation regions is still the raw material out of which cores are built. We expect that in general core masses and collapse timescales will decrease with increasing density of the post-shock flow, which itself increases with increasing Mach number. Preliminary simulations of planar converging flows that we have conducted indeed bear out this expectation, showing $M_{\mathrm{core}} \propto \mathscr{M}^{-1}$. For planar converging flows, many cores simultaneously grow and then collapse in the post-shock gas layer; unless this sheet was viewed exactly edge-on, the density jump at the shock front would not be apparent, and cores would be seen as surrounded by moderate-density gas.

We also expect outside-in collapse followed by inside-out infall to be a generic feature of core evolution. Although the duration of this pressure-mediated collapse is $\sim t_{\mathrm{ff}}$, it is *unlike* free fall collapse in a crucial way: the core does not remain nearly uniform. We speculate that the development of stratification during outside-in collapse will suppress

55

growth of perturbations and subfragmentation for the nonspherical case. Even though the increase in density implies that the local Jeans mass becomes smaller and smaller, this is only true in the very center of the core. Instead, we expect that collapse of cores built within shocked converging flows will produce single systems, which may be binary (or multiple) if the angular momentum is sufficient. Nonspherical converging flows that create sheets and filaments of shocked gas and produce many such cores simultaneously could be the progenitors of stellar clusters.

Acknowledgements

Chapter 3

Dense Core Formation in Supersonic Turbulent Converging Flows

Abstract

We use numerical hydrodynamic simulations to investigate prestellar core formation in the dynamic environment of giant molecular clouds (GMCs), focusing on planar post-shock layers produced by colliding turbulent flows. A key goal is to test how core evolution and properties depend on the velocity dispersion in the parent cloud; our simulation suite consists of 180 models with inflow Mach numbers $\mathcal{M} \equiv v/c_s = 1.1 - 9$. At all Mach numbers, our models show that turbulence and self-gravity collect gas within post-shock regions into filaments at the same time as overdense areas within these filaments condense into cores. This morphology, together with the subsonic velocities we find inside cores, is similar to observations. We extend previous results showing that core collapse develops in an "outside-in" manner, with density and velocity approaching the Larson-Penston asymptotic solution. The time for the first core to collapse depends on Mach number as $t_{\mathrm{coll}} \propto \mathcal{M}^{-1/2}\rho_0^{-1/2}$, for ρ_0 the mean pre-shock density, consistent with analytic estimates. Core building takes 10 times as long as core collapse, which lasts a few

$\times 10^5$ yrs, consistent with observed prestellar core lifetimes. Core shapes change from oblate to prolate as they evolve. To define cores, we use isosurfaces of the gravitational potential. We compare to cores defined using the potential computed from projected surface density, finding good agreement for core masses and sizes; this offers a new way to identify cores in observed maps. Cores with masses varying by three orders of magnitude ($\sim 0.05 - 50 M_\odot$) are identified in our high-$\mathcal{M}$ simulations, with a much smaller mass range for models having low $\mathcal{M}$. We halt each simulation when the first core collapses; at that point, only the more massive cores in each model are gravitationally bound, with $E_{\text{th}} + E_g < 0$. Stability analysis of post-shock layers predicts that the first core to collapse will have mass $M \propto v^{-1/2} \rho_0^{-1/2} T^{7/4}$, and that the minimum mass for cores formed at late times will have $M \propto v^{-1} \rho_0^{-1/2} T^2$, for T the temperature. From our simulations, the median mass lies between these two relations. At the time we halt the simulations, the M vs. v relation is shallower for bound cores than unbound cores; with further evolution the small cores may evolve to become bound, steeping the M vs. v relation.

3.1   Introduction

Star formation begins with the creation of dense molecular cores, and understanding how cores grow and evolve is essential to identifying the origin of stellar properties (André et al. 2008; McKee & Ostriker 2007; Shu et al. 1987). Through the 1990s, the prevailing theoretical picture was of slow core formation and evolution mediated by ambipolar diffusion, followed by core collapse initiated from a quasistatic, centrally-concentrated state (e.g., Mouschovias 1987; Mouschovias & Ciolek 1999). Current observations, however, indicate that magnetic field strengths are insufficient to provide the dominant support of molecular cores (Troland & Crutcher 2008). In addition, over the past decade, a conception of star formation has emerged in which supersonic turbulence drives structure

and evolution within giant molecular clouds (GMCs) on a wide range of scales (e.g., Ballesteros-Paredes et al. 2007; McKee & Ostriker 2007). Because supersonic turbulence can compress gas to densities at which gravitational collapse can rapidly occur, it is likely to be important in the initiation of prestellar cores. Ultimately, models of core formation and evolution must take into account both moderate magnetic fields (with diffusion) and strong turbulence (Kudoh & Basu 2008; Nakamura & Li 2008). In order to gain insight into the physics involved, however, it is informative to focus on individual limiting cases and explore dependence on parameters. Here, following Gong & Ostriker (2009) but generalizing to three dimensions, we consider core building and evolution in the turbulence-dominated, unmagnetized limit.

Observations of dense cores in GMCs have provided detailed information on individual core properties as well as statistics of core populations (see e.g., the reviews of André et al. 2008; Bergin & Tafalla 2007; di Francesco et al. 2007; Ward-Thompson et al. 2007). These properties, including internal structure and kinematics, durations of different evolutionary stages, and distribution of core masses, constrain core formation theories. In terms of structure, cores are observed to be centrally concentrated at all stages, with the specific profile fits differing depending on the stage of evolution. Cores can generally be fit with a uniform-density inner region surrounded by a power law $\propto r^{-2}$ (e.g., Alves et al. 2001; Bacmann et al. 2000; Kandori et al. 2005; Kirk et al. 2005; Shirley et al. 2000); this shape is consistent with expectations for both static Bonnor-Ebert (BE) pressure-supported isothermal equilibria (Bonnor 1956; Ebert 1955), and for collapsing isothermal spheres (Bodenheimer & Sweigart 1968; Larson 1969; Penston 1969). The center-to-edge density contrast is frequently larger than the maximum possible for a stable BE sphere, however, and the inferred temperatures based on static BE fits are also often larger than observed temperatures. Although in principle some support could be provided by magnetic fields (e.g., Ciolek & Mouschovias 1994), another possibility is

that these "supercritical" cores are in fact collapsing rather than static (Dapp & Basu 2009; Gong & Ostriker 2009).

In terms of kinematics, dense, low-mass cores generally have subsonic internal velocity dispersions, whether for isolated cores or for cores found in clusters (e.g., André et al. 2007; Caselli et al. 2002; Goodman et al. 1998; Kirk et al. 2007; Lada et al. 2008; Myers 1983; Tafalla et al. 2004). Some prestellar cores also show indications of subsonic inward motions throughout their interiors based on asymmetry of molecular lines that trace dense gas (e.g., Lee & Myers 1999; Lee et al. 2001; Sohn et al. 2007). For cores containing protostars, signatures of supersonic inward motions on small scales ($\sim 0.01 - 0.1$ pc) have been observed (e.g., Di Francesco et al. 2001; Gregersen et al. 1997); these are believed to be indicative of gravitationally-induced infall. In very recent work, Pineda et al. (2010) have used NH_3 observations to identify a sharp transition from supersonic to subsonic velocity dispersion from outer to inner regions in the core B5 in Perseus.

Several recent statistical studies have reached similar conclusions regarding the durations of successive stages of core evolution (e.g., Enoch et al. 2008; Evans et al. 2009; Ward-Thompson et al. 2007), with prestellar and protostellar (class 0) stages having comparable lifetimes. The typical duration for each of these stages is a few times the gravitational free-fall time

$$t_{ff} = \left(\frac{3\pi}{32G\bar{\rho}} \right)^{1/2} = 4.3 \times 10^5 \text{ yr} \left(\frac{\bar{n}_H}{10^4 \text{ cm}^{-3}} \right)^{-1/2} \tag{3.1}$$

at the mean core density $\bar{\rho} = 1.4 m_H \bar{n}_H$, amounting to $\sim 1 - 5 \times 10^5$ yr for typical conditions. With prestellar lifetimes considerably below the ambipolar diffusion time for strong magnetic field $t_{AD} \approx 10 t_{ff}$ (e.g. Mouschovias & Ciolek 1999), this suggests that observed cores are trans-critical or supercritical (see Ciolek & Basu 2001) with respect to the magnetic field. The critical mass-to-magnetic-flux defines the minimum that permits gravitational collapse in the field-freezing limit (e.g. Mestel & Spitzer 1956; Mouschovias & Spitzer 1976; Nakano & Nakamura 1978). This conclusion is also supported by mag-

netic field Zeeman observations (Troland & Crutcher 2008), indicating that cores have mean mass-to-magnetic-flux ratios twice the critical value. Thus, magnetic field effects appear to be sub-dominant in terms of supporting cores against collapse, and ambipolar diffusion does not appear to control the dynamics of core formation and evolution. As magnetic fields are non-negligible, however, magnetohydrodynamic (MHD) stresses may still affect GMC and core dynamics.

Empirical measurements of core mass functions (CMFs) (e.g., Alves et al. 2007; Beuther & Schilke 2004; Enoch et al. 2006; Ikeda & Kitamura 2009; Ikeda et al. 2009, 2007; Johnstone et al. 2000, 2001; Könyves et al. 2010; Motte et al. 1998, 2001; Nutter & Ward-Thompson 2007; Onishi et al. 2002; Reid & Wilson 2005, 2006; Simpson et al. 2008; Stanke et al. 2006; Testi & Sargent 1998) show that CMFs have a remarkable similarity in shape to stellar initial mass functions (IMFs, see e.g. Chabrier 2005; Kroupa 2001), with a shift toward lower mass by a factor of $3 - 4$ (see e.g., Alves et al. 2007; Rathborne et al. 2009). The characteristic/turnover mass of observed CMFs ranges from $0.1 - 3$ $M_\odot$, although there are uncertainties in this associated with lack of spatial resolution at the low mass end.

Many theoretical efforts have contributed to interpreting the observed properties of cores. The classic work of Bonnor (1956) and Ebert (1955) provided the foundation of later studies, by determining the maximum mass of a static isothermal sphere that is dynamically stable. In terms of the boundary pressure $P_{\text{edge}} = \rho_{\text{edge}} c_s^2$ or mean internal density $\bar{\rho} = 2.5 \rho_{\text{edge}}$, this maximum stable mass is

$$M_{BE} = 1.2 \frac{c_s^4}{(G^3 P_{\text{edge}})^{1/2}} = 1.9 \frac{c_s^3}{(G^3 \bar{\rho})^{1/2}} = 2.3 \text{ M}_\odot \left(\frac{\bar{n}_H}{10^4 \, \text{cm}^{-3}} \right)^{-1/2} \left(\frac{T}{10K} \right)^{3/2} . \quad (3.2)$$

Here, $c_s = (kT/\mu)^{1/2}$ is the internal sound speed in the core.

Over many years, numerical simulations have been used to investigate isothermal collapse of individual, pre-existing cores (Bodenheimer & Sweigart 1968; Burkert & Alves 2009; Foster & Chevalier 1993; Gómez et al. 2007; Hennebelle et al. 2003; Hunter 1977;

Larson 1969; Motoyama & Yoshida 2003; Ogino et al. 1999; Penston 1969; Vorobyov & Basu 2005). These simulations include initiation from static configurations that are unstable, and initiation from static, stable configurations that are subjected to imposed compression, either from enhanced external pressure or a converging velocity field, or a core-core collision. A common feature of the results is that the collapse generally starts from outside and propagates in as the central density increases. At the time of singularity formation, the density profile approaches the "Larson-Penston" asymptotic solution $\rho = 8.86c_s^2/(4\pi G r^2)$ and the central velocity is comparable to the value $-3.28c_s$ derived by Larson (1969) and Penston (1969). However, these previous studies have not considered core evolution within the larger context, in particular including the process of *core formation*. Since the formation process may affect later evolution, it is important to develop unified models.

At GMC scales, a number of groups have investigated the CMFs that result from numerical simulations of turbulent, self-gravitating systems (see e.g., Basu et al. 2009; Bonnell et al. 2003; Clark et al. 2008; Gammie et al. 2003; Heitsch et al. 2008; Klessen 2001; Li et al. 2004; Offner et al. 2008; Smith et al. 2009; Tilley & Pudritz 2004). These models have shown – for certain parts of parameter space – features that are in accord with observed CMFs: mass functions dominated by the low end with a peak and turnover near 1 M$_\odot$, and a high-mass power-law slope (at least marginally) consistent with the Salpeter value. These simulations have not, however, had sufficient resolution to investigate the internal properties of individual cores that form. In addition, these studies have not quantified how the core masses depend on the large-scale properties of the turbulent medium (see below).

Taking the previous numerical simulations of individual cores one step further, Gong & Ostriker (2009) initiated a study of dynamically induced core formation and evolution in supersonic converging flows, focusing on the spherical case. In these simulations,

the density is initially uniform everywhere: no initial core structure is assumed. Instead, dense cores form inside a spherical shock that propagates outward within the converging flow. Over time, cores become increasingly stratified as their masses grow. Eventually, the core collapses to create a protostar following the same "outside-in" pattern as in models initiated from static conditions. Subsequently, the dense envelope falls into the center via an inside-out rarefaction wave (Hunter 1977; Shu 1977); this is followed by a stage of late accretion if the converging flow on large scales continues to be maintained. The unified formation and evolution model of Gong & Ostriker (2009) explains many observed core properties, including BE-sphere-like density profiles, subsonic internal velocities within cores, and short core lifetimes with comparable prestellar and protostellar durations. Gong & Ostriker (2009) also found that the inflow velocity of the converging flows affects core lifetimes, masses, sizes and accretion histories. Realistic supersonic inflows in clouds are not spherical, however, while mass inflow rates are affected by geometry. Thus, the quantitative results for masses, lifetimes, etc., as a function of Mach number and ambient density may differ for more realistic geometry.

Numerical results on core formation have not reached consensus on how the characteristic mass in the CMF, M_c, depends on the bulk properties of the cloud – its mean density $\rho_0 = \langle \rho \rangle$, sound speed c_s, and turbulent velocity dispersion v_{turb}. Some have suggested that the Jeans mass of the cloud at its mean density ($M_J = c_s^3 \pi^{3/2} (G^3 \rho_0)^{-1/2}$) determines M_c in the CMF (e.g,. Bonnell et al. 2006; Klessen 2001), while others have found values of M_c well below M_J (see e.g., Gammie et al. 2003; Li et al. 2004). As noted by McKee & Ostriker (2007), the difference between these conclusions is likely related to the Mach number of turbulence: the value found for M_c/M_J is lower in simulations where the Mach number $\mathscr{M} \equiv v_{\text{turb}}/c_s$ is higher. Indeed, more recent simulations by Clark et al. (2008) provide some indication that increasing $\mathscr{M}$ lowers the value of M_c in the CMF; they did not, however, conduct a full parameter study.

Supersonic turbulence makes the density in a GMC highly non-uniform, creating a log-normal probability distribution function (PDF) in which most of the volume is at densities below ρ_0 and most of the mass is at densities above ρ_0 (e.g., Ostriker et al. 1999; Padoan et al. 1997; Vazquez-Semadeni 1994). Given that the log-normal PDF allows for a range of Jeans masses (or Bonnor-Ebert masses; $M_{BE} \propto M_J$), Padoan & Nordlund (2002, 2004) proposed that the CMF is set by dividing the total available gas mass at each density into unstable cores. Padoan et al. (2007) propose that the peak mass in the CMF is given by $M_c = 3M_{BE,0}/M_A^{1.1}$ for $M_A \equiv v_{\text{turb}}/v_A$ the Alfvén Mach number in a cloud, and $M_{BE,0}$ the Bonnor-Ebert mass evaluated at the mean cloud density n_0. Here, $v_A \equiv B/(4\pi\rho)^{1/2}$ is the Alfvén speed. For realistic mean GMC density $n_0 \sim 100\,\text{cm}^{-3}$ and $\mathscr{M}_A \sim 1-4$, from Equation (3.2) the Padoan et al formula in fact yields $M_c > 15\ \text{M}_\odot$; only if one chooses a much higher reference density does this agree with observations. For the unmagnetized case, Padoan et al. (2007) propose that $M_c = 4M_{BE,0}/\mathscr{M}^{1.7}$. Hennebelle & Chabrier (2008) point out that shock compression is underestimated in the magnetized case by Padoan et al. (2007), and advocate a formula similar to their unmagnetized one: $M_c \sim M_{BE,0}/\mathscr{M}^{3/2}$. Since $\mathscr{M} \geqslant 10$ in massive GMCs, these formulae yield more realistic values $M_c \sim\ \text{M}_\odot$. Neither the Padoan et al. (2007) or the Hennebelle & Chabrier (2008) proposal has, however, been tested directly using self-gravitating numerical simulations.

In this contribution, we present results on core formation and evolution based on a large suite of 3-dimensional numerical simulations. Each simulation models a localized region of a turbulent cloud in which there is an overall convergence in the velocity field. Under the assumption that there is a dominant convergence direction locally, we choose inflow along a single axis, so that convergence is planar. With the more realistic geometry afforded by the current simulations, we are able to check the results obtained by Gong & Ostriker (2009) for core building and collapse in supersonic flows. We are also able to explore how the characteristic core mass is related to the velocity of the converging

64

flows. Since the speed of converging flow is assumed to reflect the amplitude of the largest-scale (dominant) motions in a GMC, this relates the characteristic core mass to the turbulent Mach number in its parent GMC. Although a number of previous studies of core formation have been conducted, the present investigation is distinguished by our systematic study of Mach number dependence, together with our focus on internal structure and kinematics of the cores that form.

The plan of this chapter is as follows: In Section 2 we provide a physical discussion of self-gravitating core formation in the post-shock dense layers, identifying the mass, size, and time scales expected to be important. In Section 3, we summarize the governing equations and methods used in our numerical simulations. Section 4 describes the development of core structure and evolution in our models, paying particular attention to the influence of Mach number $\mathscr{M}$ on the evolution, and comparing collapse of individual cores with Gong & Ostriker (2009). Section 5 describes our method of core-finding, in which the largest closed contour of the gravitational potential determines the core size. We demonstrate that this method can be used for both three dimensional and two dimensional data with similar results, and can thus be applied to find cores in observed clouds. Section 6 describes the relations between core properties (core mass, core radius and core collapse time) and the large-scale Mach number of the converging flow, relating to the expectations from gravitational instability discussed in Section 2. In Section 6, we also quantify core shapes, and explore the relationship between core structure and kinematics. Section 7 summarizes our new results and discusses our findings in the context of previous theories and observations.

3.2 The Characteristic Core Mass and Size

Prior to describing our numerical model prescription and results, it is useful to summarize the scales that are likely to be relevant for formation of self-gravitating cores in GMCs. We shall assume approximately isothermal conditions, consistent with observations (e.g. Blitz et al. 2007). The isothermal sound speed at a temperature T is

$$c_s = 0.20 \text{ km s}^{-1} \left(\frac{T}{10 \text{ K}} \right)^{1/2}. \tag{3.3}$$

If the density within clouds were uniform, the spatial scale relevant for gravitational instability would be the Jeans length

$$L_J \equiv c_s \left(\frac{\pi}{G\rho_0} \right)^{1/2} = 2.76 \text{ pc} \left(\frac{n_{H,0}}{10^2 \text{ cm}^{-3}} \right)^{-1/2} \left(\frac{T}{10 \text{ K}} \right)^{1/2}, \tag{3.4}$$

evaluated at the mean density ρ_0. The corresponding Jeans mass is

$$M_J \equiv \rho_0 L_J^3 = c_s^3 \left(\frac{\pi^3}{G^3 \rho_0} \right)^{1/2} = 72 \text{ M}_\odot \left(\frac{n_{H,0}}{10^2 \text{ cm}^{-3}} \right)^{-1/2} \left(\frac{T}{10 \text{ K}} \right)^{3/2}. \tag{3.5}$$

Note that $\rho_0(L_J/2)^3$ or $\rho_0 4\pi (L_J/2)^3/3$ is sometimes used for the Jeans mass. The Bonnor-Ebert mass (eq. 3.2) for $P_{\text{edge}} = P_0 \equiv \rho_0 c_s^2$ is $M_{\text{BE}} = 0.22 M_J(\rho_0)$. The Jeans time at the mean cloud density is

$$t_J \equiv \frac{L_J}{c_s} = \left(\frac{\pi}{G\rho_0} \right)^{1/2} = 3.27 t_{\text{ff}}(\rho_0) = 1.4 \times 10^7 \text{ yr} \left(\frac{n_{H,0}}{10^2 \text{ cm}^{-3}} \right)^{-1/2}. \tag{3.6}$$

We shall use the Jeans length, mass, and time at the unperturbed density as our code units of length, mass, and time: $L_0 = L_J$, $M_0 = M_J$, and $t_0 = t_J$.

Of course, GMCs are highly inhomogeneous, with core formation taking place in the overdense regions that have the shortest gravitational times. If the overdense regions within GMCs are produced by shocks in the turbulent, supersonic flow, their density, and therefore the mass scale and length scale for growth of self-gravitating structures, will be related to the shock strength. Strongly magnetized shocks have less compression

than weakly magnetized shocks (while both will be present in a turbulent flow), so we concentrate on the latter case.

If gravitationally unstable cores develop only in gas that has been strongly compressed by shocks, the actual bounding pressure will be much larger than $P_0 = \rho_0 c_s^2$. In particular, an isothermal shock with Mach number $\mathcal{M}$ will produce a post-shock region with pressure $P_{\text{post-shock}} = \rho_0 v^2 = \mathcal{M}^2 \rho_0 c_s^2 \gg P_0$. Thus, if cores preferentially form in stagnation regions between shocks of Mach number $\mathcal{M}$, then one can define an effective Bonnor-Ebert mass for these core-forming regions within the turbulent flow by setting $P_{\text{edge}} = P_{\text{post-shock}}$ in equation (3.2):

$$M_{BE,\text{post-shock}} \equiv 1.2 \frac{c_s^3}{(G^3 \rho_0)^{1/2}} \frac{1}{\mathcal{M}} = 2.8 \ \text{M}_\odot \left(\frac{v}{1 \text{kms}^{-1}}\right)^{-1} \left(\frac{n_{H,0}}{10^2 \, \text{cm}^{-3}}\right)^{-1/2} \left(\frac{T}{10 \, \text{K}}\right)^2. \tag{3.7}$$

The above simple argument suggests $M \propto v^{-1} \rho_0^{-1/2} T^2$ for the minimum mass of a star that forms via collapse of a core in a turbulent cloud with velocity dispersion v, mean density ρ_0, and temperature T.

Equation (3.7) provides a mass scale for fragmentation within post-shock regions, but in fact instabilities take some time to develop. Thus, it is useful to consider the evolution of a simple system consisting of a planar shocked layer formed by a converging flow (see e.g. Elmegreen & Elmegreen 1978; Iwasaki & Tsuribe 2008; Lubow & Pringle 1993; Vishniac 1994; Whitworth et al. 1994).

For inflow Mach number $\mathcal{M}$, the surface density of the post-shock layer at time t is

$$\Sigma(t) = \rho_0 \left(v_{z,+} - v_{z,-}\right) t = 2\rho_0 \mathcal{M} c_s t, \tag{3.8}$$

where $v_{z,+}$ and $v_{z,-}$ are the upward and downward converging velocities. If the sheet is not vertically self-gravitating, its half-thickness is $H = \Sigma(t)/2\rho_p$ where $\rho_p \approx \rho_0 \mathcal{M}^2$ is the post-shock density. The non-self-gravitating half-thickness is thus

$$H_{\text{nsg}} \approx \frac{2\rho_0 \mathcal{M} c_s t}{2\rho_0 \mathcal{M}^2} = \frac{c_s t}{\mathcal{M}}. \tag{3.9}$$

As the surface density of the sheet increases, self-gravity will become increasingly important in confining the gas. In the limit of hydrostatic equilibrium, the height approaches

$$H_{\text{sg}} = \frac{c_s^2}{\pi G \Sigma} = \frac{c_s}{2\pi G \rho_0 \mathcal{M} t}. \tag{3.10}$$

Note that the transition from non-self-gravitating ($H_{\text{nsg}} \propto t$) to self-gravitating ($H_{\text{sg}} \propto t^{-1}$) occurs at a time near

$$t_{\text{sg}} \equiv \frac{1}{(2\pi G \rho_0)^{1/2}} = 0.22 t_J, \tag{3.11}$$

defined by the condition $H_{\text{sg}} = H_{\text{nsg}}$.

The dispersion relation for in-plane modes in a slab, allowing for non-zero H (e.g. Kim et al. 2002), is

$$\omega^2 \approx c_s^2 k^2 - \frac{2\pi G \Sigma k}{1 + kH}. \tag{3.12}$$

For the critical mode $\omega^2 = 0$, so that

$$k_{\text{crit}} H \left(1 + k_{\text{crit}} H\right) = 2\pi H \frac{G\Sigma}{c_s^2} = 2\pi \frac{H}{L_{\text{J,2D}}}, \tag{3.13}$$

where

$$L_{\text{J,2D}} \equiv \frac{c_s^2}{G\Sigma} \tag{3.14}$$

is the Jeans length for an infinitesimally-thin layer. The solution to equation (3.13) is

$$k_{\text{crit}} = \frac{2\pi}{L_{\text{J,2D}}} \frac{2}{1 + \left(1 + 8\pi \frac{H}{L_{\text{J,2D}}}\right)^{1/2}} = \frac{4\pi G \rho_0 t \mathcal{M}}{c_s} \frac{2}{1 + \left(1 + 8\pi \frac{H}{L_{\text{J,2D}}}\right)^{1/2}}, \tag{3.15}$$

so that

$$\lambda_{\text{crit}} = L_{\text{J,2D}} \frac{1 + \left(1 + 8\pi \frac{H}{L_{\text{J,2D}}}\right)^{1/2}}{2} = \frac{c_s}{2 G \rho_0 t \mathcal{M}} \frac{1 + \left(1 + 8\pi \frac{H}{L_{\text{J,2D}}}\right)^{1/2}}{2}. \tag{3.16}$$

The corresponding critical mass $(\lambda_{\text{crit}}/2)^2 \Sigma$ is

$$M_{\text{crit}} \equiv \frac{c_s^3}{32 G^2 \rho_0 \mathcal{M}} \frac{\left[1 + (1 + 8\pi \frac{H}{L_{\text{J,2D}}})^{1/2}\right]^2}{t}. \tag{3.17}$$

Note that $H/L_{J,2D}$ initially increases in time, during the non-self-gravitating stage ($H_{nsg}/L_{J,2D} = 2G\rho_0 t^2$), and then approaches a constant ($H_{sg}/L_{J,2D} = 1/\pi$). At any time, all wavelengths $\lambda > \lambda_{crit}$ have $\omega^2 < 0$, so that overdense regions of the corresponding sizes and masses $M > M_{crit}$ grow relative to their surroundings.

During the non-self-gravitating stage, the critical mass has a minimum value at time

$$t_{crit,nsg,min} = \left(\frac{3}{16\pi G\rho_0}\right)^{1/2} = 0.14t_J = 0.61t_{sg} \tag{3.18}$$

given by

$$M_{crit,nsg,min} = \frac{3\sqrt{3\pi}}{8}\frac{c_s^3}{(G^3\rho_0)^{1/2}}\frac{1}{\mathcal{M}} \tag{3.19}$$

$$= 3.0 \text{ M}_\odot \left(\frac{v}{1\text{kms}^{-1}}\right)^{-1}\left(\frac{n_{H,0}}{10^2\,\text{cm}^3}\right)^{-1/2}\left(\frac{T}{10\text{ K}}\right)^2. \tag{3.20}$$

The numerical coefficient in equation (3.19) is 1.15; note that this is almost the same as in equation (3.7).

At late time, the critical mass from Equation (3.17) with $H_{sg}/L_{J,2D} = 1/\pi$ becomes

$$M_{crit,sg} = \frac{c_s^3}{2G^2\rho_0\mathcal{M}t} = \frac{c_s^4}{G^2\Sigma}. \tag{3.21}$$

Expressing $M_{crit,sg}$ in terms of the virial parameter $\alpha_{vir} = 5\sigma_v^2 R/GM_{GMC}$ of the GMC, and using $\sigma_v = \mathcal{M}c_s$ and $M_{GMC} = \pi R^2\Sigma_{GMC} = 4\pi R^3\rho_0/3$, we have

$$M_{crit,sg} = \left(\frac{3\pi\alpha_{vir}}{20}\right)^{1/2}\frac{c_s^3}{(G^3\rho_0)^{1/2}}\frac{1}{\mathcal{M}}\frac{\Sigma_{GMC}}{\Sigma}. \tag{3.22}$$

Here σ_v is the large-scale one-dimensional velocity dispersion in GMCs, which will be responsible for the largest scale, strongest shocks. Taking $\alpha_{vir} = 2$, the coefficient in Equation (3.22) is 0.97, so this is very similar to equations (3.7) and (3.19) if $\Sigma \sim \Sigma_{GMC}$. In dimensional units, the critical mass (for $\Sigma = \Sigma_{GMC}$) is

$$M_{crit,sg} = 2.5 \text{ M}_\odot \left(\frac{v}{1\text{kms}^{-1}}\right)^{-1}\left(\frac{n_{H,0}}{10^2\,\text{cm}^{-3}}\right)^{-1/2}\left(\frac{T}{10\text{ K}}\right)^2. \tag{3.23}$$

As noted above, equations (3.7), (3.19) – (20) and (3.22) – (3.23) all have a similar form. An important task for numerical simulations is therefore to test the hypothesis that the characteristic mass scale of collapsing cores formed in turbulent, self-gravitating GMCs follows this scaling, i.e.

$$M_c = \psi \frac{c_s^4}{(G^3 \sigma_v^2 \rho_0)^{1/2}} = \psi \times 2.6 \; \mathrm{M_\odot} \left(\frac{\sigma_v}{1\mathrm{kms}^{-1}}\right)^{-1} \left(\frac{n_{H,0}}{10^2 \, \mathrm{cm}^{-3}}\right)^{-1/2} \left(\frac{T}{10 \, \mathrm{K}}\right)^2, \quad (3.24)$$

where ψ is a dimensionless coefficient.

The critical mass given above is the smallest mass that can collapse, given infinite time. Since the growth rate depends on scale (and is formally zero for critical perturbations), at any finite time only cores that have grown sufficiently rapidly will be non-linear enough to collapse. It is therefore useful to consider how much growth has occurred at a given time. Consider a perturbation of wavenumber k that instantaneously has $d^2 \delta\Sigma/dt^2 = -\omega^2 \delta\Sigma$ so that $\delta\Sigma = \delta\Sigma_{\mathrm{init}} e^\Gamma$ where $\Gamma = \ln(\delta\Sigma/\delta\Sigma_{\mathrm{init}}) = \int (-\omega^2)^{1/2} \, dt$. Using equation (3.12),

$$\Gamma = \int_{t_{\mathrm{min}}}^t (-\omega^2)^{1/2} dt = \int_{t_{\mathrm{min}}}^t \left(\frac{2\pi G \Sigma k}{1 + kH} - c_s^2 k^2\right)^{1/2} dt, \quad (3.25)$$

where t_{min} is the instant when Σ is large enough that perturbations of wavenumber k start to grow ($-\omega^2 \geqslant 0$). With $\Sigma = 2\rho_0 c_s \mathscr{M} t$, $t_{\mathrm{min}} = c_s k(1 + kH)/(4\pi G \rho_0 \mathscr{M})$. If we assume $kH \ll 1$ (see below), then

$$\Gamma = \frac{2\sqrt{2}}{3} \kappa^{1/2} (\tau - \kappa/2)^{3/2}, \quad (3.26)$$

where $\kappa = kc_s/\sqrt{2\pi G \rho_0 \mathscr{M}}$ and $\tau = t\sqrt{2\pi G \rho_0 \mathscr{M}}$.

At a given time t (or τ) during the evolution, the mode k_m (or κ_m) that has grown the most has $\partial \ln \Gamma/\partial k = 0$, which gives

$$\kappa_m = \frac{\tau}{2}, \quad (3.27)$$

and $\Gamma_{\mathrm{max}} = \Gamma(k_m) = \sqrt{3}\kappa_m^2 = \sqrt{3}\pi G \rho_0 \mathscr{M} t^2/2$. The mass of this most-amplified mode is:

$$M_m \equiv \left(\frac{\lambda_m}{2}\right)^2 \Sigma = \left(\frac{2\sqrt{3}\pi}{\Gamma_{\mathrm{max}}}\right)^{1/2} \frac{c_s^3}{(G^3 \rho_0)^{1/2}} \frac{1}{\mathscr{M}^{1/2}}, \quad (3.28)$$

70

where the time is

$$t = \left(\frac{2\Gamma_{\max}}{\sqrt{3}\pi} \right)^{1/2} \left(\frac{1}{G\rho_0} \right)^{1/2} \frac{1}{\mathcal{M}^{1/2}}, \tag{3.29}$$

and $k_m = (\Gamma_{\max}/\sqrt{3})^{1/2} (2\pi G\rho_0 \mathcal{M})^{1/2}/c_s$, so that

$$\lambda_m = \left(\frac{2\sqrt{3}\pi}{\Gamma_{\max}} \right)^{1/2} \frac{c_s}{(G\rho_0)^{1/2}} \frac{1}{\mathcal{M}^{1/2}}. \tag{3.30}$$

With $\Gamma_{\max} = 1$, the numerical coefficient for M_m in Equation (3.28) is 3.30, and Equation (3.29) gives $t = 0.34 t_J \mathcal{M}^{-1/2}$, corresponding to $\tau = 1.5$. Note that for low Mach number, this time exceeds t_{sg} (see eq. 3.11), whereas for high Mach number it does not. Also, note that with $H < c_s t_{sg}/\mathcal{M} \equiv H_{\max}$ (see eqs. 3.9 - 3.11), $k_m H < k_m H_{\max} = \Gamma_{\max}^{1/2}(\sqrt{3}\mathcal{M})^{-1/2}$. Taking $\Gamma_{\max} = 1$, $k_m H < 0.8$ for $\mathcal{M} > 1$, with $k_m H \ll 1$ for $\mathcal{M} \gg 1$. This verifies self-consistency of the assumption made in obtaining equation (3.26).

Written in terms of v, ρ_0, and T, the most-amplified mass is

$$M_m = 19.1 \ \mathrm{M}_\odot \left(\frac{v}{1\mathrm{kms}^{-1}} \right)^{-1/2} \left(\frac{n_{H,0}}{10^2 \, \mathrm{cm}^{-3}} \right)^{-1/2} \left(\frac{T}{10 \ \mathrm{K}} \right)^{7/4} (\Gamma_{\max})^{-1/2}. \tag{3.31}$$

Comparing equation (3.31) with equation (3.23), we see that a different dependence on velocity (or Mach number) is expected for the first core to collapse (equation 3.31), compared to the typical core to form eventually (equation 3.23). Similar results to equation (3.28) have previously been discussed by other authors. Whitworth et al. (1994) point out that the fastest-growing scale $\sim L_{J,2D} \sim c_s/(G\rho_0 \mathcal{M}t)$ will become nonlinear if the time exceeds the growth time $\sim L_{J,2D}/c_s \sim (G\rho_0 \mathcal{M}t)^{-1}$, which occurs for $t \sim (G\rho_0 \mathcal{M})^{-1/2}$ (cf. our eq. 3.29). This corresponds to a length scale $L_{\mathrm{fragment}} \sim c_s(G\rho_0 \mathcal{M})^{-1/2}$ (cf. our eq. 3.30), and a mass scale $M_{\mathrm{fragment}} \sim c_s^3 (G^3 \rho_0 \mathcal{M})^{-1/2}$ (cf. our eq. 3.28). By direct integration of the perturbation equation of the converging-flow system, Iwasaki & Tsuribe (2008) find that the fastest-growing mode becomes nonlinear at time $0.96\delta_0^{-0.1}(G\rho_0 \mathcal{M})^{-1/2}$, for δ_0 the initial amplitude (cf. our eq. 3.29, which has a coefficient 0.6 if $\Gamma_{\max} = 1$).

Finally, we note that the characteristic mass scale at late times given in equation (3.24) can be connected to observed core mass scales using the empirical relationships among turbulence level, size, and mass for GMCs. In terms of the viral parameter $\alpha_{\mathrm{vir}} \equiv 5\sigma_v^2 R/(GM_{\mathrm{GMC}})$ and the GMC surface density $\Sigma_{\mathrm{GMC}} \equiv 4\rho_0 R/3$, equation (3.24) can be re-expressed as

$$M_c = 1.5\psi \frac{c_s^4}{\alpha_{\mathrm{vir}}^{1/2} G^2 \Sigma_{\mathrm{GMC}}} = \psi \times 1 \ \mathrm{M_\odot} \left(\frac{T}{10K}\right)^2 \left(\frac{\Sigma_{\mathrm{GMC}}}{100 \ \mathrm{M_\odot \ pc^{-2}}}\right)^{-1} \alpha_{\mathrm{vir}}^{-1/2}. \quad (3.32)$$

With $\alpha_{\mathrm{vir}} \sim 1 - 2$ and $\Sigma_{\mathrm{GMC}} \sim 100 \ \mathrm{M_\odot \ pc^{-2}}$ for observed clouds (Heyer et al. 2009; McKee & Ostriker 2007; Solomon et al. 1987), the mass scale is intriguingly similar to the characteristic (peak) mass of CMFs within nearby molecular clouds. This relation potentially also offers a prediction for the peak of the CMF (and ultimately the IMF) when stars form under conditions different from those in most Milky Way GMCs. In particular, high temperature (up to ~ 70 K) may hold in starburst regions where the radiation field is strong and turbulent dissipation rates are high; since the temperature dependence of equation (3.32) is steeper than the dependence on surface density, this could imply higher masses under those conditions.

3.3 Methods for Numerical Simulations

The numerical simulations we present here are conducted with the *Athena* code (Gardiner & Stone 2005, 2008; Stone et al. 2008; Stone & Gardiner 2009), using the HLLC solver (Toro 1999) and second order reconstruction (Stone et al. 2008). To calculate the self-gravity of our slab domains, which are periodic in-plane and open in the z direction, the Fast Fourier Transformation (FFT) method developed by Koyama & Ostriker (2009) is used. We solve the three-dimensional equations of hydrodynamics,

$$\frac{\partial \rho}{\partial t} + \nabla \cdot (\rho \boldsymbol{v}) = 0, \quad (3.33)$$

$$\frac{\partial \mathbf{v}}{\partial t} + \mathbf{v} \cdot \nabla \mathbf{v} = -\frac{\nabla P}{\rho} - \nabla \Phi; \tag{3.34}$$

and the Poisson equation,

$$\nabla^2 \Phi = 4\pi G \rho, \tag{3.35}$$

where Φ is the gravitational potential. The isothermal assumption $P = c_s^2 \rho$ is adopted. Pavlovski et al. (2006) found the isothermal approximation is adequate for simulations of the interstellar medium even with strong turbulence, which implies strong shocks in GMCs.

The code unit of density ρ_0 is a fiducial density representing the volume-averaged ambient density in a cloud on large scales; this characterizes the mean density of converging flows. For the code unit of velocity, we adopt the isothermal sound speed c_s (see eq. 3.3). For the unit of length, we adopt $L_0 = L_J$, the Jeans length at the fiducial density (see eq. 3.4). The mass and time units for the simulation are then $M_0 = M_J$ (see eq. 3.5) and $t_0 = t_J$ (see eq. 3.6).

In making comparison to observations, the total surface density integrated through the domain

$$\Sigma = \int \rho(x,y,z)dz = \Sigma_0 \int \frac{\rho}{\rho_0} \frac{dz}{L_J} \tag{3.36}$$

is useful, for $\Sigma_0 \equiv \rho_0 L_J = 9.49 \ M_\odot \ \mathrm{pc}^{-2}(T/10K)^{1/2}(n_{H,0}/10^2 \,\mathrm{cm}^{-3})^{1/2}$. In terms of the column density of hydrogen,

$$N_H = \frac{\Sigma}{1.4 m_p} = N_0 \int \frac{n_H}{n_{H,0}} \frac{dz}{L_J} \tag{3.37}$$

for $N_0 \equiv n_0 L_J = 8.51 \times 10^{20} \,\mathrm{cm}^{-2}(T/10K)^{1/2}(n_{H,0}/10^2 \,\mathrm{cm}^{-3})^{1/2}$. The mean line-of-sight velocity is calculated by

$$\langle v_{\mathrm{los}} \rangle = \frac{\int \rho v_{\mathrm{los}} ds}{\int \rho ds}, \tag{3.38}$$

and the corresponding dispersion of $\langle v_{\mathrm{los}} \rangle$ is defined as

$$\sigma_{\mathrm{los}}^2 = \frac{\int \rho (v_{\mathrm{los}} - \langle v_{\mathrm{los}} \rangle)^2 ds}{\int \rho ds}, \tag{3.39}$$

where $ds = sec\theta\, dz$ and θ is the tilt angle of the observer with respect to the z axis.

Our model prescription consists of a converging flow augmented with turbulent velocity perturbations. In our parameter survey, the Mach number $\mathscr{M}$ of the inflow velocity ranges from 1.1 to 9. Thus, two flows converge toward the central plane $z = 0$ from the upper z-boundary (with mean velocity $-\mathscr{M}c_s$) and the lower z-boundary (with mean velocity $\mathscr{M}c_s$). The initial density is uniform and set to ρ_0, and the density at the inflowing z-boundaries is also set to ρ_0 throughout the simulation. The boundaries in the x and y directions are periodic.

For both the whole domain initially and the inflowing gas subsequently, we apply perturbations following a Gaussian random distribution, with a Fourier power spectrum of the form

$$\langle |\delta \boldsymbol{v}_k|^2 \rangle \propto k^{-2}, \tag{3.40}$$

for $|kL/2\pi| < N/2$, where N is the resolution and L is the size of the simulation box in x and y. The power spectrum is appropriate for supersonic turbulence as observed in GMCs (McKee & Ostriker 2007). The perturbation velocity fields are pre-generated with resolution 256^3 in a box of size L^3. The perturbation fields are advected inward from the z-boundaries at inflow speed $\mathscr{M}c_s$: at time intervals $\Delta t = \Delta z/(\mathscr{M}c_s)$, slices of the pre-generated perturbation fields for v_x, v_y and v_z are read in to update values in the ghost zones at the z-boundaries.

In addition to exploring dependence on the mean inflow Mach number $\mathscr{M}$, we also test dependence on the amplitude of turbulent perturbations on top of this converging flow. From the scaling law (see e.g., Heyer & Brunt 2004; Larson 1981) of self-gravitating molecular clouds, $\delta v(l) \propto l^{1/2}$, we can write the velocity dispersion at scale l in terms of cloud-scale one-dimensional velocity dispersion σ_v and cloud radius R as $\delta v_{1D}(l) = \sigma_v(l/2R)^{1/2}$. The velocity dispersion at the scale of the simulation box L is

$$\frac{\delta v_{1D}(L)}{c_s} = \frac{\sigma_v}{c_s}\left(\frac{L}{2R}\right)^{1/2} = \frac{\sigma_v}{c_s}\left(\frac{L}{L_J}\right)^{1/2}\left(\frac{2R}{L_J}\right)^{-1/2}. \tag{3.41}$$

In terms of the viral parameter $\alpha_{\text{vir}} \equiv 5\,\sigma_v^2 R/(GM)$, where $M = 4\pi R^3 \rho_0/3$ is the cloud mass, the ratio between σ_v and c_s is

$$\frac{\sigma_v}{c_s} = 2\pi \left(\frac{\alpha_{\text{vir}}}{15}\right)^{1/2} \frac{R}{L_J}. \tag{3.42}$$

Solving equation (3.42) for $2R/L_J$ and substituting into equation (3.41), we have the amplitude of perturbation for the simulation box:

$$\frac{\delta v_{1D}(L)}{c_s} = \left(\frac{\alpha_{\text{vir}}\pi^2}{15}\right)^{1/4} \left(\frac{\sigma_v}{c_s}\right)^{1/2} \left(\frac{L}{L_J}\right)^{1/2}. \tag{3.43}$$

Thus, if the size of the simulation box is $L = L_J$ and $\alpha_{vir} = 1 - 2$, the perturbation amplitude would be

$$\frac{\delta v_{1D}(L_J)}{c_s} \approx \left(\frac{\sigma_v}{c_s}\right)^{1/2}. \tag{3.44}$$

If we take the Mach number of the inflow, $\mathcal{M}$, as comparable to the value σ_v/c_s of the whole cloud, then equation (3.44) implies that higher converging velocities would be associated with higher amplitudes for the perturbation fields, for a given simulation box size L_J. To test the influence of the perturbation amplitude, we conduct two sets of simulations with 10% and 100% of the value $\delta v_{1D}(L_J) = (\mathcal{M}/3)^{1/2}c_s$. Hereafter, we denote these cases as low amplitude and high amplitude initial perturbations, respectively.

For each Mach number $\mathcal{M}$ at each amplitude, we run 20 simulations with different random realizations of the same perturbation power spectrum, in order to collect sufficient statistical information on the core properties that result. The whole set of simulations therefore consists of 180 separate runs. The resolution for low amplitude perturbation simulations is $N_x \times N_y \times N_z = 256 \times 256 \times 96$, with domain size $L_x \times L_y \times L_z/L_J^3 = 1 \times 1 \times 0.375$; for high amplitude the resolution is $N_x \times N_y \times N_z = 256 \times 256 \times 160$, with domain size $L_x \times L_y \times L_z/L_J^3 = 1 \times 1 \times 0.625$. The domain in the z direction is smaller than in the x and y directions since the reversed shock generated by the inflow only propagates a relatively short distance and the post-shock dense layer is thin, i.e., the basic geometry

remains planar. The domain in the *z* direction is large enough so that the post-shock layer does not evolve to reach the *z* boundaries.

We note that our assumption of perturbed velocities but uniform densities in the inflowing gas is not fully realistic, since the flow entering a strong shock within a GMC will in general have internal density structure. Other recent simulations of post-shock structure formation in converging flows have similarly assumed uniform density for the inflow (see e.g. Banerjee et al. 2009; Heitsch et al. 2008, and references therein). In fact, the velocity perturbations we introduce do lead to moderate (order-unity) density fluctuations, as we have found by conducting comparison simulations with self-gravity turned off. These density fluctuations are what seed the growth of self-gravitating structures. The main emphasis of the current work is to investigate how the development of self-gravitating structures depends on the inflow Mach number, which sets the mean density (and hence the gravitational timescale) in the post-shock layer; previous studies have not tested the Mach number dependence of gravitational fragmentation. By varying the velocity perturbation amplitudes of the inflow, we have begun to explore the effect of pre-existing density structure on self-gravitating core development in shocked regions. This exploration can be extended and made more realistic (in terms of upstream structure) by investigating internal evolution of shocked layers within larger fully-turbulent clouds having a range of mean Mach number; we are currently pursuing a numerical study along these lines. The models presented here may be thought of as investigating self-gravitating structure growth within the first strong shocks to develop inside a cloud.

3.4 Development of Structure and Core Evolution

As discussed in Section 1, Gong & Ostriker (2009) proposed a unified model for core formation and evolution in supersonic turbulent environments. Based on spherical-symmetry numerical simulations, four stages were identified: core building, core collapse, envelope infall and late accretion. The duration of each stage, and the structure and kinematics of cores at varying stages were also analyzed. While the comparison of those results to observations is very encouraging, the assumption of spherical symmetry is clearly unrealistic. One of the key goals of this work is to check if core building and collapse still develop in a similar manner when the spherical-symmetry assumption is relaxed. Because the time step becomes very short in late stages, we halt the simulations; thus the current models do not address envelope infall and late accretion stages.

Figure 3.1 shows evolution of the surface density (eq. 3.36) for models with $\mathcal{M} = 1.1$ (left column), $\mathcal{M} = 5$ (middle column) and $\mathcal{M} = 8$ (right column), all with same realization for the perturbation velocities. The top panel of each column shows the surface density very early on; the patterns are identical but the amplitudes are different. The bottom panel shows the surface density when the most evolved core collapses for each case. Hereafter we shall use t_{coll} to denote the total time to reach collapse of the most evolved core, in terms of the code unit t_0 (eq. 3.6). The four images from top to bottom in the same column show the surface density at four instants: $t = 0.001 t_0$, $1/3 t_{\mathrm{coll}}$, $2/3 t_{\mathrm{coll}}$, and t_{coll}. Note that $t_{\mathrm{coll}} = 0.636 t_0, 0.280 t_0$ and $0.232 t_0$ for the $\mathcal{M} = 1.1, 5$ and 8, respectively. These three simulations have low initial perturbation amplitude (cf. eq. 3.44).

From Figure 3.1, two features are immediately apparent. First, the input perturbation field patterns determine the later structural evolution and there is a "family resemblance" for the models at different Mach number. This is because the post-shock dense layer retains a memory of the perturbation velocity fields in the direction parallel to the plane

of the layer since v_x and v_y are unchanged across the shock interface. Comparing the first plot to the last plot of each column, cores form in regions where the density perturbation amplitudes are initially higher than the surroundings as a result of convergence in the $x - y$ plane. These overdense regions develop into long, thin filaments, within which cores grow and then collapse.
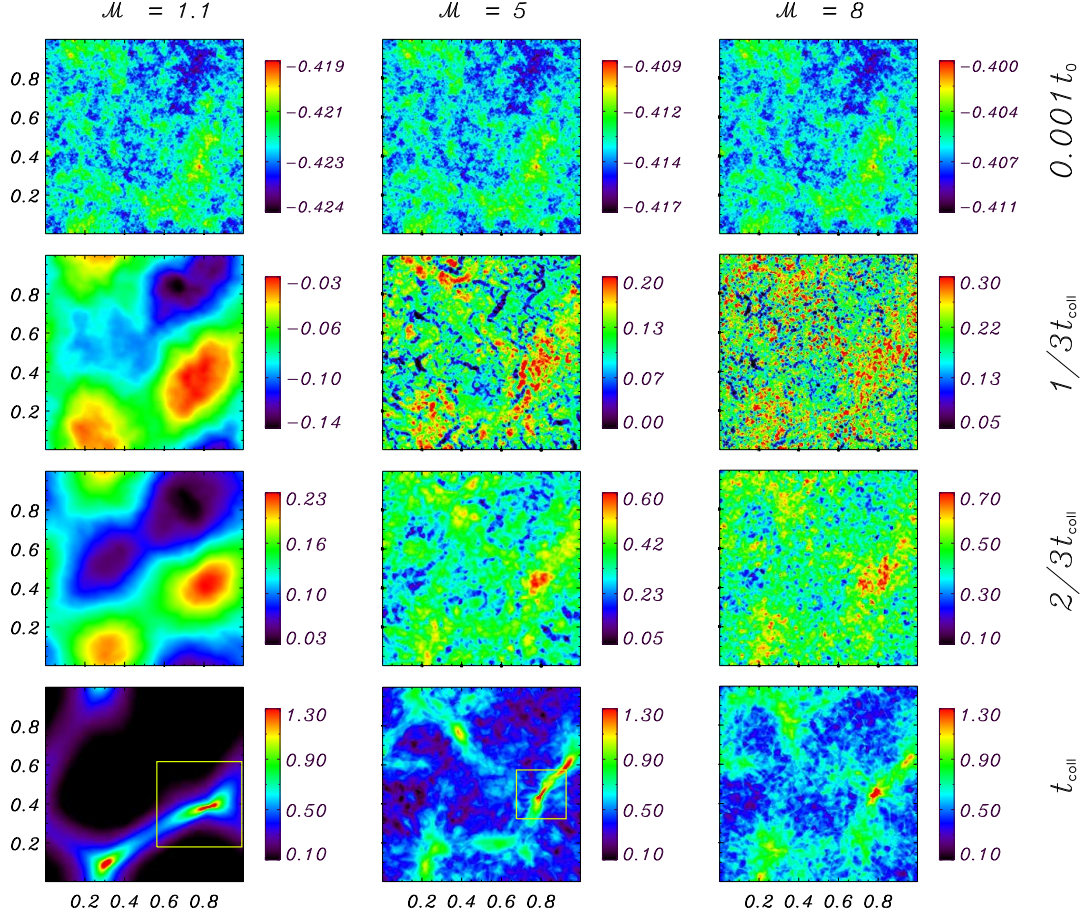
Figure 3.1: Evolution of surface density projected in the z direction $\mathcal{M} = 1.1$ (left column), $\mathcal{M} = 5$ (middle column) and $\mathcal{M} = 8$ (color scale $\log\Sigma/\Sigma_0 = \log N/N_0$; see eqs. 3.36, 3.37) for converging-flow Mach number $\mathcal{M} = 1.1$ (left column), $\mathcal{M} = 5$ (middle column) and $\mathcal{M} = 8$ (right column) models with the same initial perturbation patterns. The four panels from top to bottom in the each column show surface density snapshots at four instants: $t = 0.001 t_0$, $1/3t_{\mathrm{coll}}$, $2/3t_{\mathrm{coll}}$, and t_{coll}, with t_{coll} the duration of the whole simulation. These three simulations have 10% initial perturbation amplitude (see eq. 3.43). The values of t_{coll} are $0.636t_0, 0.280t_0$ and $0.232t_0$ for $\mathcal{M} = 1.1, 5$ and 8 respectively (see eq. 3.6 for definition of t_0). Cores are clearly smaller and more irregular for high-$\mathcal{M}$ models. The squares indicate the most evolved cores for $\mathcal{M} = 1.1$ and 5.

Second, the specific properties of cores, such as the total number and individual volumes (as well as their masses), are determined by $\mathcal{M}$. The dense cores for $\mathcal{M} = 1.1$ are smoother than the cores for $\mathcal{M} = 8$, and they cover larger areas. During the middle and late stages of evolution, more small scale filamentary structures are evident in the higher Mach number cases. At a given scale, the input v_x and v_y perturbations are higher for larger $\mathcal{M}$, with the resulting compressions making more prominent "burrs" around cores. The "burrs" are also less smoothed for the high Mach number cases, because the shorter free-fall time at the higher post-shock density means that the core collapses sooner. Thus, as the velocity of the converging flow and additional perturbations increases, the result is smaller, denser, more irregular, and more "hairy" cores.

Figure 3.2 shows evolution of surface density and the mean in-plane velocities $\langle v_x \rangle$ and $\langle v_y \rangle$ for the $\mathcal{M} = 5$ model shown in Figure 3.1. The mean velocities are calculated by $\langle v \rangle = \int \rho v \, dz / \int \rho \, dz$ with $v = v_x$ or v_y. The left column shows surface density, and the middle and the right columns show $\langle v_x \rangle$, $\langle v_y \rangle$ respectively. At early stages, only scattered high surface density spots appear. The large-scale spatial correlation of these overdense regions is evident, however, even at early times. The mean velocities also have small amplitudes at early stages. The large-scale converging (in-plane) velocity regions that eventually lead to the most prominent filaments are already evident from the first frames, however. At late stages, the overdense regions start to collect into filaments. The converging (in-plane) velocities grow due to self-gravity of the forming filaments; in addition, purely hydrodynamic instabilities (such as the nonlinear thin-shell instability, e.g. Heitsch et al. 2007; Vishniac 1994) in the shock-bounded layer may enhance early growth of perturbations. We have conducted comparison tests of selected models without self-gravity, finding that surface density fluctuations can grow to order-unity level in high Mach number cases. When converging in-plane flows become supersonic, discontinuities in the density and velocity develop. These sharp fronts, as well as the collapsing motions
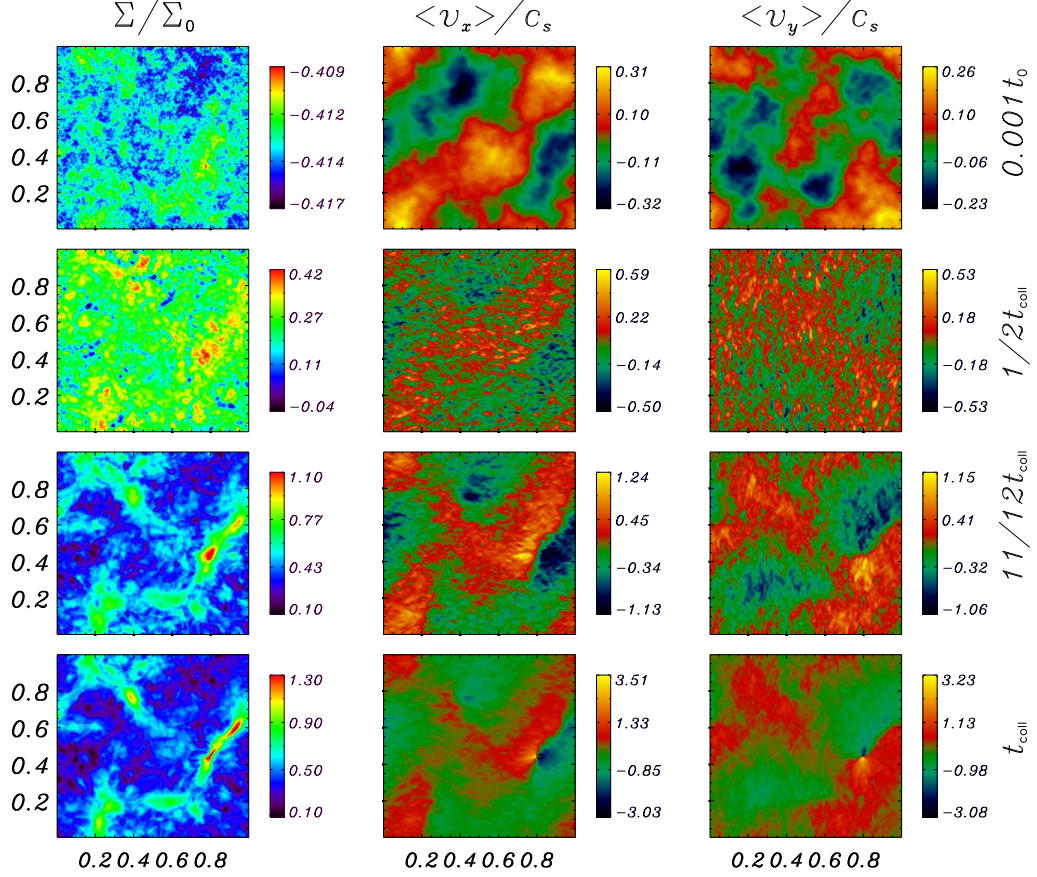
Figure 3.2: Evolution of surface density (left column, log color scale) and the in-plane velocity components $\langle v_x \rangle$ (middle column) and $\langle v_y \rangle$ (right column) projected in the z direction for the Mach number $\mathcal{M} = 5$ model shown in Figure 3.1, where $\langle v \rangle = \int \rho v \, dz / \int \rho \, dz$. The four panels from top to bottom in the each column show four instants: $t = 0.001 t_0$, $1/2 t_{\rm coll}$, $11/12 t_{\rm coll}$, and $t_{\rm coll}$, with $t_{\rm coll} = 0.28 t_0$ the duration of the simulation (see eq. 3.6 for definition of t_0). In-plane velocity fields are initially low, but grow to become supersonic, creating filaments that fragment into cores.

centered on the most evolved cores, are evident in Fig. 3.2 at $t = 11/12 t_{\rm coll}, t_{\rm coll}$.

Thus, we see that turbulent motions even at sub-pc scales seed the growth of structures, and self-gravity reinforces and amplifies these motions. The growth of dense cores and larger scale filaments is simultaneous, both a consequence of turbulence and self-gravity.

Similar to our results in Gong & Ostriker (2009) for spherical symmetry, we find that core building lasts most of the time up to $t_{\rm coll}$, while the core collapse itself is rapid

for the most evolved cores. Defining the "supercritical" period as the stage at which $\rho_{\text{center}}/\rho_{\text{edge}} \geq 10$ for the most evolved core, this first occurs at $0.589 t_0, 0.240 t_0$ and $0.209 t_0$ respectively for the $\mathcal{M} = 1.1, 5$ and 8 models shown in Figure 3.1 (we note that ρ_{edge} is close to the post-shock density). Taking the difference with t_{coll}, $\Delta t_{\text{supcrit}}/t_0 = 0.047, 0.040$ and 0.023. From Gong & Ostriker (2009), the supercritical stage lasts about 10% of t_{coll} for cores found in shocked converging spherical flows. For the three cases shown here, $\Delta t_{\text{supcrit}}/t_{\text{coll}}$ is 7%, 14%, and 10%, consistent with our previous results. The core building stage lasts about 90% of t_{coll}.
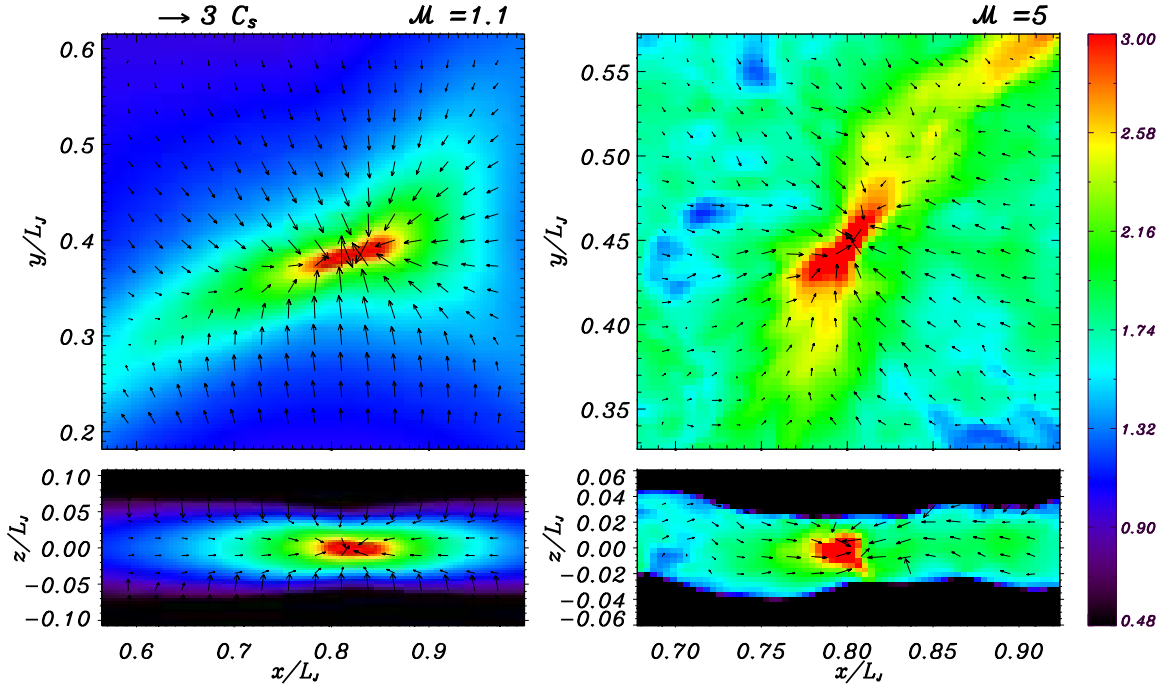
Figure 3.3: Density and velocity field cross-sections at the time t_{coll} in the most evolved core, for $\mathcal{M} = 1.1$ (left column) and $\mathcal{M} = 5$ (right column). These correspond to the most evolved cores (as indicated with boxes) in Figure 3.1 for $\mathcal{M} = 1.1, 5$ respectively. The color scale represents $x - y$ and $x - z$ slices through the volume density ($\log \rho/\rho_0$). The direction and length of arrows indicate the direction and magnitude of the local velocity, with scale as indicated in the upper left. At this stage of collapse, velocities increase toward the center.

To express $\Delta t_{\text{supcrit}}$ in terms of observables, we renormalize using the mean core density ρ_{mean} at the instant of collapse. This quantity, $\Delta t_{\text{supcrit}}/t_{ff}(\rho_{\text{mean}}) = \Delta t_{\text{supcrit}}/t_0 \times$

$3.27(\rho_{\mathrm{mean}}/\rho_0)^{1/2}$ is measured to be $0.9, 2.1$ and 0.8 for $\mathscr{M} = 1.1, 5$ and 8 respectively; i.e. $\Delta t_{\mathrm{supcrit}}$ is comparable to $t_{ff}(\rho_{\mathrm{mean}})$. The values of $\Delta t_{\mathrm{supcrit}}$ are 6.6×10^5 yr, 5.6×10^5 yr and 3.2×10^5 yr for $\mathscr{M} = 1.1, 5$ and 8 respectively, if we take the inflowing ambient medium density as $n_{H,0} = 100\,\mathrm{cm}^{-3}$; these are reduced to 2×10^5 yr, 1.7×10^5 yr and 1×10^5 yr for $n_{H,0} = 1000\,\mathrm{cm}^{-3}$.

Figure 3.3 shows the cross-sections of the density and velocity field across the center of the most evolved cores (the locations of these cores are indicated in Figure 3.1) for $\mathscr{M} = 1.1, 5$ during the late collapse phase. The instants of the plot for $\mathscr{M} = 1.1, 5$ are $0.625\,t_0$ and $0.273\,t_0$ respectively. The top panels show the $x - y$ cross-section of density and velocity vectors composed of v_x and v_y in the same plane. The bottom part shows the $x - z$ cross-section and velocity vectors composed of v_x and v_z. The velocity field clearly shows inward collapse. The amplitudes of the velocity field are smaller in the outer part and larger in the inner part, indicating the core is at a very late stage of the "outside-in" collapse.

Figure 3.4 and Figure 3.5 show the evolution of the density and velocity profiles of the cores in Figure 3.3. The density profiles are azimuthally-averaged over the $x - y$ plane. The velocity profiles are along each cardinal axis $(\hat{x}, \hat{y}, \hat{z})$ through the core center. The instants for the four profiles have equal intervals $0.027\,t_0$ for $\mathscr{M} = 1.1$ and equal intervals $0.019\,t_0$ for $\mathscr{M} = 5$ respectively. The first instant for both cases is subcritical (i.e. $\rho_{\mathrm{center}}/\rho_{\mathrm{edge}} \leq 10$) and the second instant is close to t_{supcrit}. The dramatic increase of the central density during collapse is clearly evident for both cases, and the collapse develops in an "outside-in" manner with the maximum in v moving inward in time. The density profile approaches the asymptotic "Larson-Penston" profile $\rho/\rho_0 = 8.86(r/L_J)^{-2}/(2\pi)^2$ at the instant of central singularity formation, and the in-plane velocities v_x, v_y approach $-3.3\,c_s$, which is the "Larson-Penston" limit. Before the time t_{supcrit} is reached, the velocity is subsonic throughout the core region. For all of the simulations we have conducted,
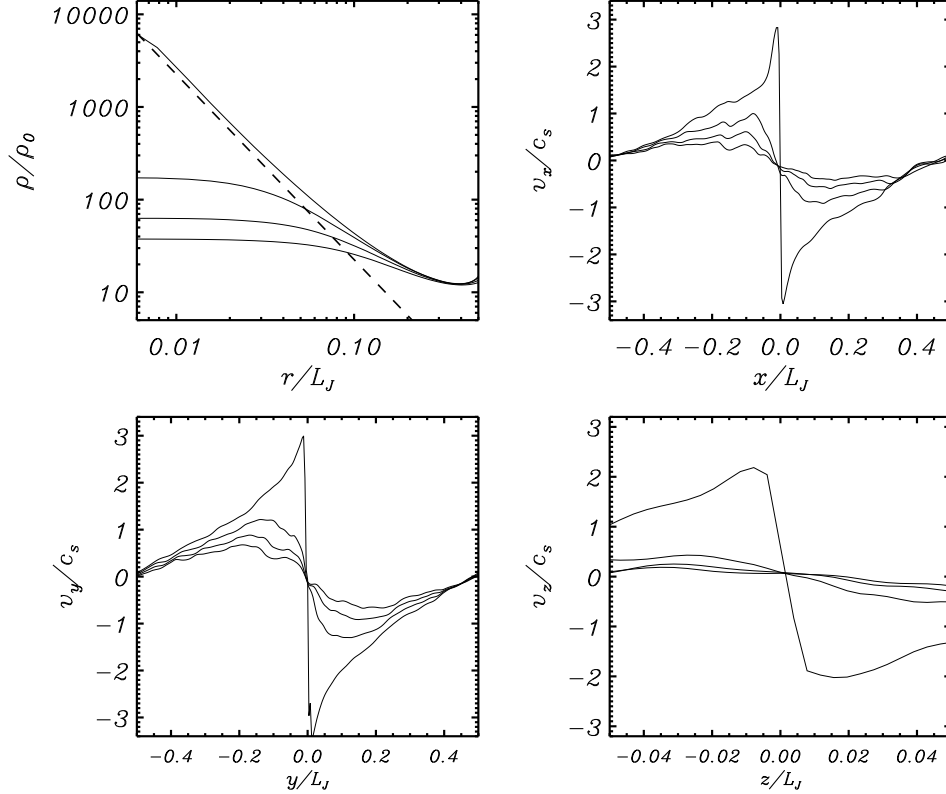
Figure 3.4: Radial density and velocity profiles during collapse, for the most evolved core shown in Figure 3.1 and Figure 3.3 for $\mathcal{M} = 1.1$. The density profiles are averaged azimuthally in the $x - y$ plane about the center of the core. The dashed line is the Larson-Penston asymptotic density profile $\rho/\rho_0 = 8.86(r/L_J)^{-2}/(2\pi)^2$ (i.e. $\rho = 8.86c_s^2/[4\pi Gr^2]$). The other three plots show the corresponding velocity profiles versus distance in the x, y and z direction, respectively. The instants shown are $0.549t_0, 0.576t_0, 0.603t_0, 0.632t_0 \approx t_{\mathrm{coll}}$, with the most evolved profiles in each case having the largest excursions. The collapse develops in an "outside-in" manner with the maximum in v moving inward with time. The density profile approaches the Larson-Penston profile with time.

the peak of the velocity profile becomes supersonic only at the very end of the collapse stage, similar to the results shown here.

Overall, we conclude that the evolution of individual cores in these 3D simulations follows a similar progression to the spherically-symmetric 1D simulations of Gong & Ostriker (2009). The core building stage lasts over 90% of the time to collapse, and cores become more stratified over time. The onset of the collapse is in an "outside-in" manner, and leads to a dramatic increase in the central density. As a central singularity is

approached, the density and velocity profiles approach the "Larson-Penston" asymptotic solution. These cores form and collapse within larger-scale filaments that also grow in contrast over time.
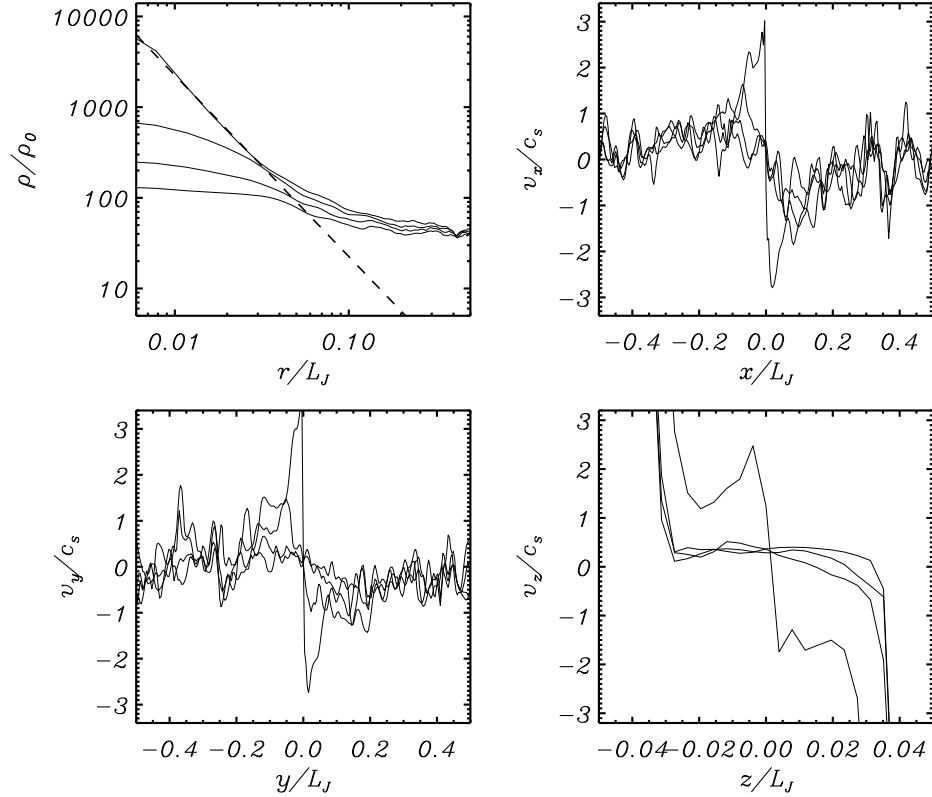
Figure 3.5: Same as in Figure 3.4 for the most-evolved core of the $\mathcal{M} = 5$ model shown in Fig. 3.1. The profiles are shown at $t = 0.219t_0, 0.238t_0, 0.257t_0, 0.276t_0$, with the density at the final time reaching the Larson-Penston solution.

3.5   Core-finding Method

The algorithm adopted for core-finding can either subtly or more seriously affect the core properties that result (e.g. Pineda et al. 2009). The most commonly-used methods in observational work are based on contouring column density or emission intensity (e.g. the popular *Clumpfind* method of Williams et al. 1994). For theoretical work, density-contouring methods, sometimes incorporating further tests to determine if a structure is

gravitationally bound, have frequently been used (e.g. Gammie et al. 2003). Here we shall instead use the gravitational potential isosurfaces to identify cores. In very recent work, Smith et al. (2009) took a similar approach, noting that one advantage of the gravitational potential is that it yields smoother core boundaries than the density. Another advantage is that the gravitational potential connects more directly to the fundamental physics that determines core evolution. During formation stages, self-gravity gathers material to build up cores, and later it drives the collapse of supercritical cores.

To identify cores via the gravitational potential, we first find and mark all the local minima of the gravitational potential; second, we find the largest closed potential contour (or isosurface) surrounding each individual minimum. In the second step, we increase the contour level from the bottom of a given potential well step by step until it violates another minimum's marked territory. We define the region enclosed by the largest closed contour as a core. The contour interval $\Delta\Phi$ has negligible effect on the results as long as it is small enough (typically $\leq 0.03c_s^2$). If the distance between two minima is smaller than 10 pixels (corresponding to a physical distance $\sim 0.03 - 0.1$pc for $n_{H,0} \sim 10^2 - 10^3$cm^{-3}), the regions associated with these two minima are merged and treated as a single core. Since we do not continue the simulation after the most evolved core collapses, we apply the algorithm to the last output from each simulation.

Since gas with sufficient thermal and kinetic energy need not be permanently (or even temporarily) bound to a given core, the gravitational potential is not the final word. The lower density outer parts of a core are the most subject to loss. We can test this effect on core identification by adding thermal energy to the gravitational energy, and only assigning a given fluid element to a core if $E_{\mathrm{th}} + E_g < 0$. For any fluid element, the specific thermal energy is taken to be $E_{\mathrm{th}} = 3/2c_s^2$, and the specific gravitational potential energy is taken to be $E_g = \Phi - \Phi_{\mathrm{max}}$, where Φ_{max} is the potential of the largest closed contour that defines the core. We note that $|E_g|$ for a core embedded within a dense filament (or

sheet) may be much lower than $|E_g|$ for the same core in isolation. In assessing whether a core is bound, it is crucial to take tidal gravity effects into account. If these tidal effects are neglected, $|E_g|$ will be overestimated by a factor $\sim \Sigma_{\text{core}}/(\Sigma_{\text{core}} - \Sigma_{\text{filament}})$, which is quite large if the contrast between a core and its surroundings is modest. Including a thermal energy condition in core definition decreases the volume (or area in 2D) of the cores. Of course, the thermal energy can in fact be radiated away, so that gas that is initially near the largest closed contour may become more strongly bound after the interior of a core collapses. In this case, the potential alone could determine the final core mass. Short of following cores through the final stages of star formation, we consider it useful to compare cores with and without a thermal - gravitational energy criterion. Hereafter, we term our core-finding method "gravitational identification" (GRID). We refer to the region within the largest closed gravitational potential isosurface surrounding each local minimum as a GRID-core. For each GRID-core, the region which has $E_{\text{th}} + E_g < 0$ is referred to as a bound GRID-core.

Because volume density data cubes are not directly accessible in observations, three-dimensional gravitational potential contouring is only applicable to model data from numerical simulations. It is therefore interesting to explore gravitational potential contouring of surface density maps, which are direct observables. To identify cores in a surface density map, we have to calculate the gravitational potential first. For a layer of half-thickness H, the gravitational potential component $\Phi_{k,\text{2D}}$ of surface density component Σ_k (Fourier transform of equation (3.36)) in phase space is

$$\Phi_{k,\text{2D}} = -\frac{2\pi G \Sigma_k}{|k|\,(1 + |kH|)},$$
(3.45)

where $|k| = \sqrt{k_x^2 + k_y^2}$. Note that for $|kH| \gg 1$, $\Phi_{k,\text{2D}} \sim -4\pi G \rho_k/k^2$, which is the solution of the Poisson equation in three dimensions, for $\rho_k = \Sigma_k/2H$. For $|kH| \ll 1$, eq. (3.45) is the solution of the Poisson equation for an infinitesimally thin layer. The gravitational potential $\Phi_{\text{2D}}(x,y)$ is the inverse Fourier transform of $\Phi_{k,\text{2D}}$. Given the 2D gravitational

86

potential field $\Phi_{2D}(x,y)$, we can apply the GRID procedure as for 3D. In Section 6, we will compare the results from GRID using $\Phi(x,y,z)$ and $\Phi_{2D}(x,y)$ (using $H = \delta z$). Hereafter we use "2D" to denote the results from applying the GRID method to surface density and "3D" for applying the GRID method to the volume density.
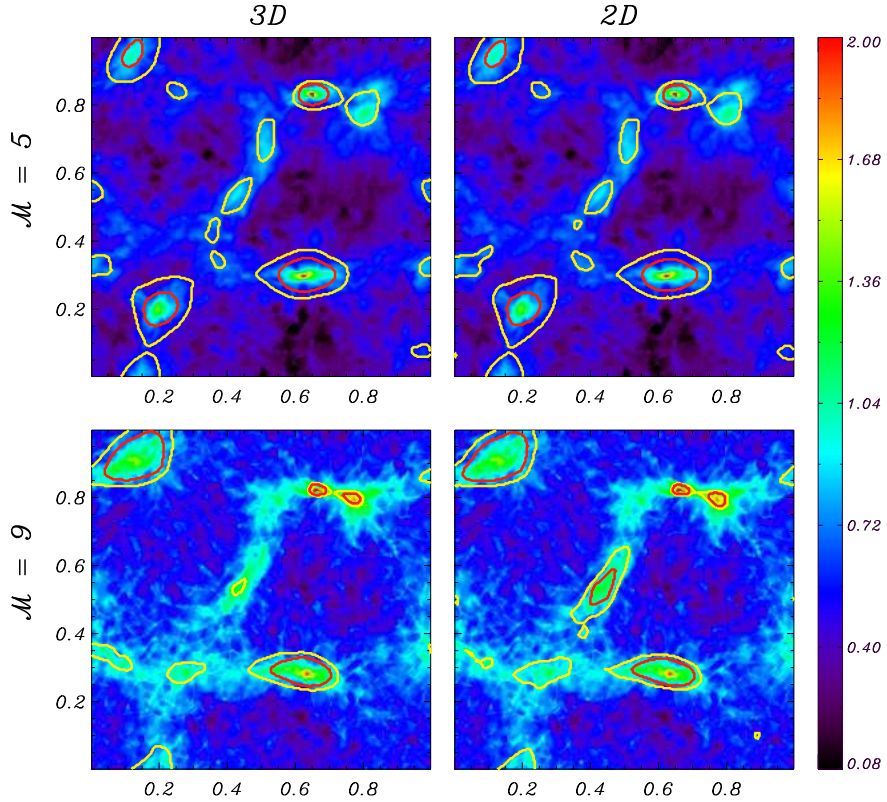
Figure 3.6: Comparison of GRID-cores defined via the gravitational potential computed from 3D volume density (Φ, left column) and 2D projected surface density (Φ_{2D}, right column). The top row shows $\mathcal{M} = 5$ and bottom row $\mathcal{M} = 9$. The areas enclosed by yellow curves are the GRID-cores determined by the largest closed gravitational potential (Φ or Φ_{2D}) contour surrounding a local potential minimum, and the areas enclosed by red curves are the bound GRID-cores. Color scale shows projected surface density ($\log\Sigma/\Sigma_0$) in all panels. Cores identified using Φ and Φ_{2D} agree quite well.

As an example, Figure 3.6 shows the comparison of GRID-cores and bound GRID-cores between 3D and 2D for $\mathcal{M} = 5$ and 9. The top portion shows core areas identified for the $\mathcal{M} = 5$ model using Φ (top left) and Φ_{2D} (top right). The bottom portion shows the same comparison for $\mathcal{M} = 9$ with cores found from Φ (bottom left) and from Φ_{2D} (bottom right). (Note that the $\mathcal{M} = 5$ and $\mathcal{M} = 9$ simulations have the same initial

velocity perturbations patterns, which is why the overall structure is similar). In all plots, the areas enclosed by yellow contours are the GRID-cores and the areas enclosed by red contours are the bound GRID-cores. The core areas for the 3D plots are the projection of the 3D core volume onto the $z = 0$ plane. For the $\mathcal{M} = 5$ model, the 2D and 3D core-finding procedures identify 12 and 13 cores respectively; the cores and the bound regions are located at nearly the same positions. For the $\mathcal{M} = 9$ model, 7 cores are identified for both cases. One bound core in 2D lacks a 3D counterpart, implying the corresponding potential well in 3D is too shallow (see discussion of potential well depths in Section 6).

$$\mathcal{M} = 5$$
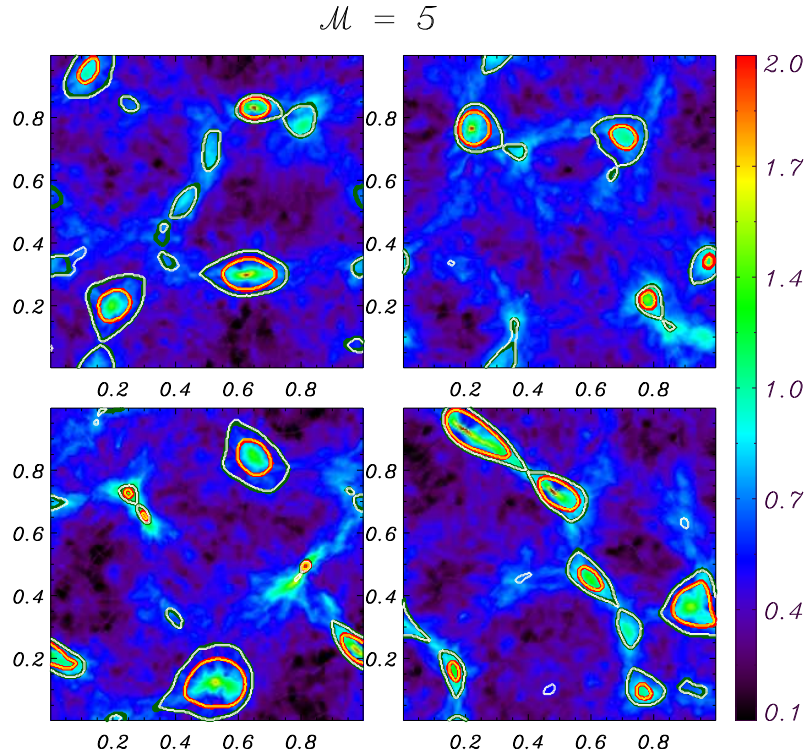
Figure 3.7: Late stage surface density ($\log\Sigma/\Sigma_0$) and GRID-core comparison for four different random perturbation realizations of the $\mathcal{M} = 5$ model. The snapshots are at $t = 0.282t_0, 0.304t_0, 0.304t_0, 0.302t_0$ from left to right and top to bottom. The corresponding maximum densities are $1.0 \times 10^5 \rho_0, 1.53 \times 10^5 \rho_0, 8.18 \times 10^4 \rho_0, 1.34 \times 10^5 \rho_0$. The white and green curves are GRID-cores defined by the largest closed contour of the gravitational potential (Φ and Φ_{2D} respectively) surrounding each potential minimum. The red and yellow curves are the bound GRID-cores obtained using Φ and Φ_{2D}, respectively. Except for a few small, shallow cores, the core-finding algorithms in 2D and 3D give quite similar results.

In addition to finding almost all of the same core centers (defined by the potential minimum), the areas marked by the 3D and 2D GRID algorithms are almost the same. Figure 3.7 show the results of GRID for four simulations for $\mathcal{M} = 5$. The white contours mark GRID-cores from 3D density and the green contours mark GRID-cores from 2D surface density. The red and yellow contours mark the bound GRID-cores for 3D and 2D respectively. The areas identified for the cores agree quite well. Over all, we conclude that the 2D GRID algorithm can give nearly identical core-finding areas as the 3D GRID algorithm.

In spite of the overall similarity between 2D and 3D GRID-core finding, there are minor differences in the results. In the each panel of Figure 3.7, a few GRID-cores in relatively low density regions are identified in 2D but not in 3D. In comparing core properties between 2D and 3D, we shall apply additional resolution criteria to eliminate these small, shallow cores.

3.6   Core Properties

To obtain a sufficient statistical sample, we conduct 20 simulations for each value of the Mach number ($\mathcal{M} = 1.1, 2, 3, 4, 5, 6, 7, 8, 9$) and compute GRID-core masses and radii for each model (180 models total). Each of the 20 simulations for a given $\mathcal{M}$ is perturbed by a different realization of the velocity field. As an example of the differences with different random realizations of the power spectrum, Figure 3.7 shows the snapshots of surface density at a late stage for four different $\mathcal{M} = 5$ simulations. The 3D GRID core numbers are 9, 6, 9 and 7. The corresponding core mass ranges are $[0.00151, 0.158]\, M_0$, $[0.0051, 0.128]\, M_0$, $[0.0013, 0.242]\, M_0$ and $[0.031, 0.250]\, M_0$. The core numbers and core masses from simulations with different seeds are in a similar range; the same is true for cases with other Mach numbers.

The GRID-core masses for 3D and 2D are $M_{3D} = \int \rho\ dxdydz$ and $M_{2D} = \int \Sigma\ dxdy$, respectively. The GRID-core radius for 3D is defined as the equivalent radius of a 3D sphere with the same volume V_{3D}: $r_{3D} \equiv (3V_{3D}/4\pi)^{1/3}$. The effective 2D GRID-core radius is calculated from the area S_{2D} of the core region as: $r_{2D} \equiv (S_{2D}/\pi)^{1/2}$. To ensure that identified GRID-cores are numerically well-resolved, we only retain cores with effective radii ≥ 4 zones. We define a background surface density as the mean of the bottom 10% of the surface density; this mean value can be subtracted from the surface density in the core region when calculating M_{2D}. As mentioned in Section 2, a more restrictive definition includes only gas with thermal plus gravitational energy negative; these bound GRID-cores are first identified by the gravitational potential, and then pixels are excluded if the sum of thermal energy and gravitational potential is greater than 0.
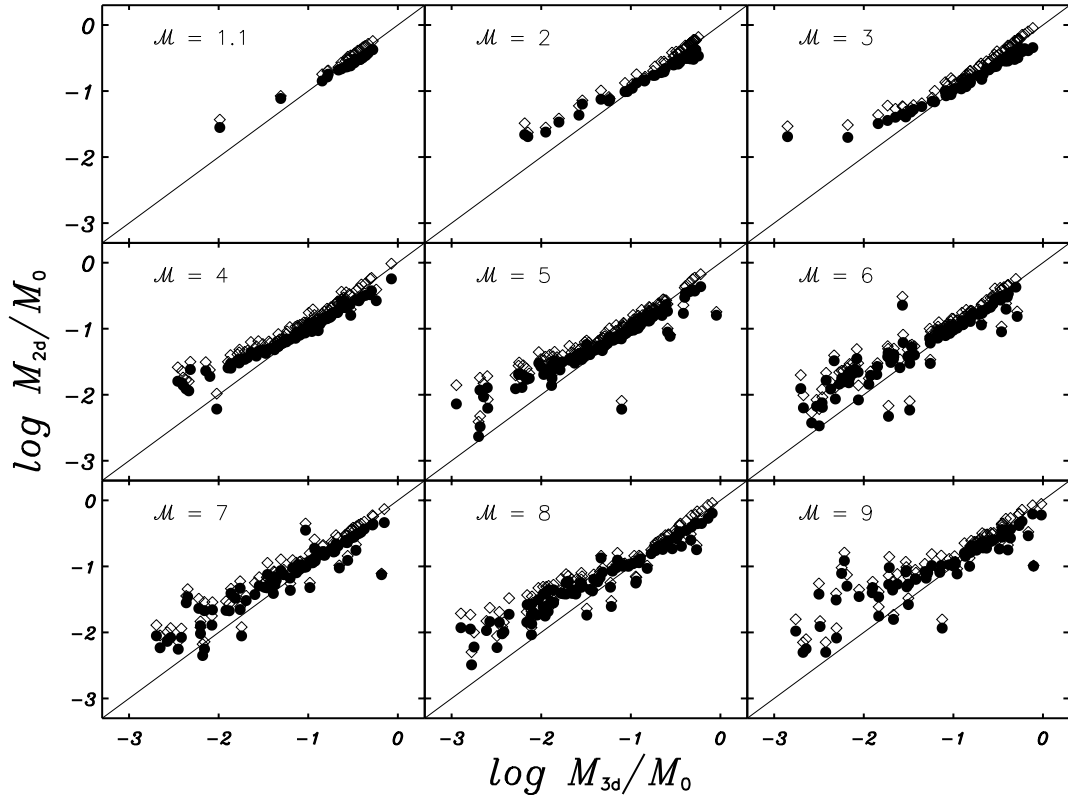
Figure 3.8: GRID-core mass obtained from 2D (M_{2D}) versus 3D (M_{3D}). Diamonds are M_{2D} for 2D GRID-cores without background subtraction, and dots are $M_{2D,bs}$ for 2D GRID-cores with background subtraction. The mass unit M_0 is given in equation (3.5). Solid lines represent $M_{2D} = M_{3D}$; higher-mass cores are consistent with this.

Figure 3.8 shows M_{2D} versus M_{3D} for GRID-cores, for each Mach number of the low amplitude perturbation set. Note that only cores with same center of the local potential minima are shown here. Both 2D GRID-core masses without background subtraction (M_{2D}, diamonds in the figure) and 2D GRID-core masses with background subtraction ($M_{2D,bs}$, dots in the figure) are shown versus M_{3D}. For large masses, M_{2D} agrees well with M_{3D} while $M_{2D,bs}$ is slightly lower than M_{3D}. For small masses, $M_{2D,bs}$ agrees better than M_{2D} with M_{3D}. Both M_{2D} and $M_{2D,bs}$ agree with M_{3D} better for high mass than low mass.
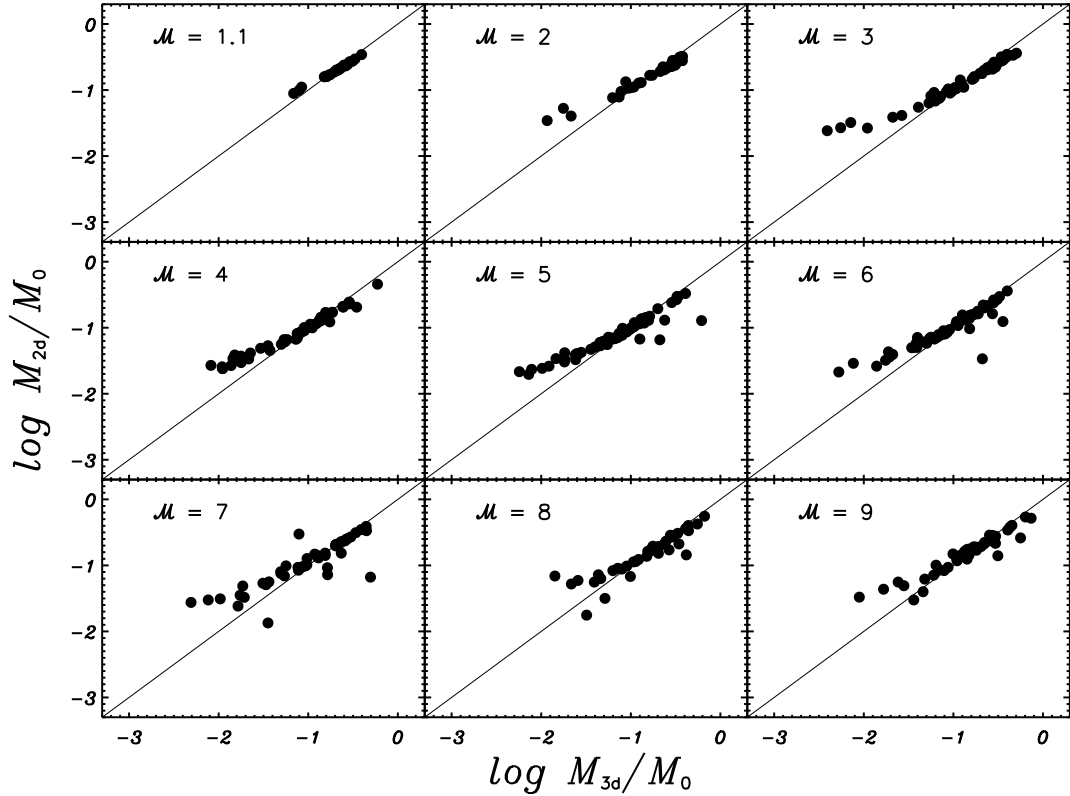
Figure 3.9: Bound GRID-core mass for 2D with background subtraction ($M_{2D,bs,th}$), versus bound GRID-core mass for 3D ($M_{3D,th}$). When the condition $E_{th} + E_g < 0$ is included in the core definition, the lowest mass cores are eliminated and $M_{2D,bs,th}$ agrees well with $M_{3D,th}$ down to $\sim 10^{-2} M_0$.

Figure 3.9 shows a similar comparison of bound GRID-cores for 2D and 3D. The background surface density is subtracted for 2D GRID-core masses, so that we show

$M_{\text{2D,bs,th}}$ versus $M_{\text{3D,th}}$. Here, the subscript "th" represents inclusion of a thermal energy criterion in defining bound GRID-cores, which eliminates most of the small cores. At high masses, $M_{\text{2D,bs,th}}$ agrees with $M_{\text{3D,th}}$ for bound GRID-cores better than $M_{\text{2D,bs}}$ agrees with M_{3D} for the whole set of GRID-cores. This is because only zones sufficiently near the potential minimum where $E_{\text{th}} + E_g < 0$ are included in bound GRID-cores; these regions are not sensitive to projection effects. At low masses, $M_{\text{2D,bs,th}}$ exceeds $M_{\text{3D,th}}$ for bound GRID-cores, meaning that imposing the thermal - gravitational energy criterion affects $M_{\text{3D,th}}$ more than $M_{\text{2D,bs,th}}$.

To understand the difference between the 2D and 3D GRID-core masses, we consider the shape of the gravitational potential well for surface density and volume density. From equation (3.45), $\Phi_{\text{2D},k} \propto -k^{-1}$ whereas $\Phi_{\text{3D},k} \propto -k^{-2}$. At larger k, corresponding to smaller scales, $|\Phi_{3D}|$ decreases faster than $|\Phi_{2D}|$. That means that the small 2D GRID-cores cover more area than small 3D GRID-cores, evident at the low end of each panel in Fig. 3.8. Also, gravitational potential wells of middle-sized 2D GRID-cores are deeper than those of 3D middle-sized GRID-cores. If the shallow parts of the potential are excluded by applying a thermal energy requirement, 3D GRID-cores are affected more than 2D GRID-cores. Moderate-mass GRID-cores that have $M_{\text{2D,bs}}$ and M_{3D} comparable will thus have $M_{\text{3D,th}}$ lower than $M_{\text{2D,bs,th}}$, as is evident in Fig. 3.9. As mentioned in Section 5, we include the term $|\boldsymbol{k}|H$ to allow for the non-zero thickness of the layer perpendicular to the plane. This can, in principle, help decrease the gap between the 2D and 3D gravitational potentials. In practice, however, we find that the value for H to make the central-to-edge value of Φ_{2D} comparable to that for Φ is smaller than δz. Although the 2D and 3D gravitational potentials are not exactly the same, Figure 3.9 shows that 2D and 3D bound GRID-cores masses are generally close down to $\sim 10^{-2} M_0$ (which is $\lesssim 1$ M$_\odot$ for typical conditions, from eq. 3.5).

Figure 3.10 shows histograms for the distributions of $M_{\text{2D,bs}}$ and M_{3D} (all GRID-
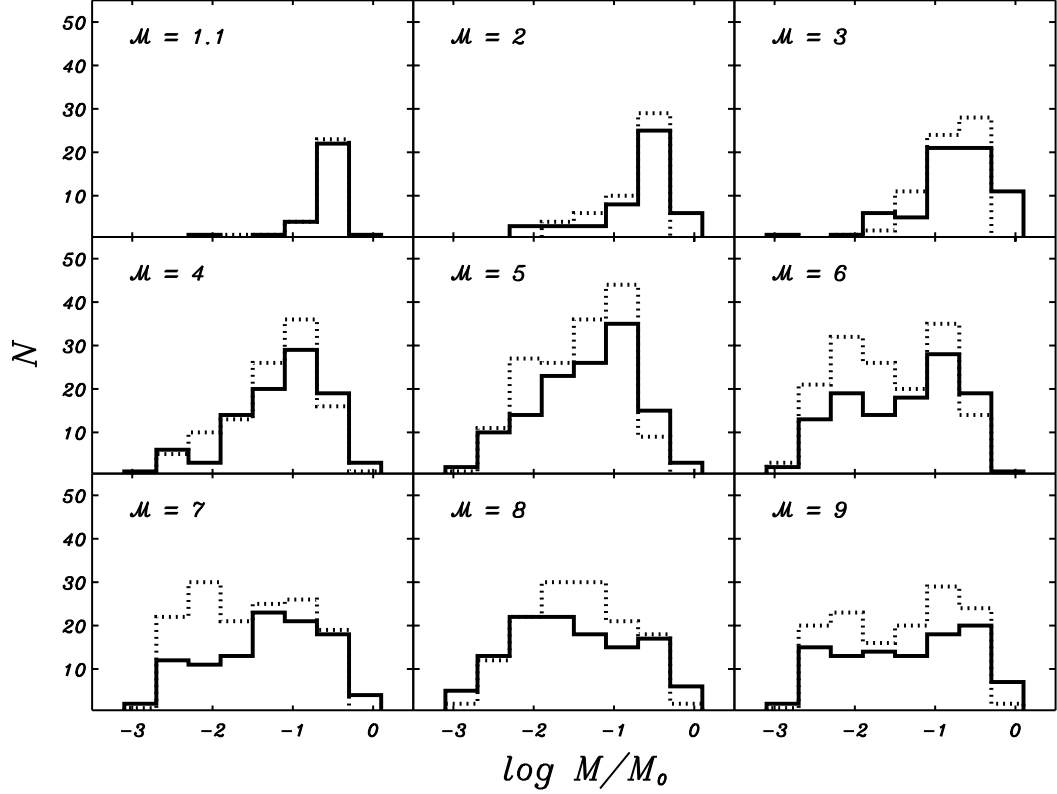
Figure 3.10: Histograms of all GRID-core masses found in all simulations for each Mach number $\mathcal{M}$ for low amplitude perturbations. Solid lines are for 3D GRID-cores (M_{3D}) and dashed lines are for 2D GRID-cores with background subtraction ($M_{2D,bs}$). The 2D and 3D distributions are similar for all Mach numbers.

cores) for each $\mathcal{M}$, while Figure 3.11 shows the histograms of $M_{2D,bs,th}$ and $M_{3D,th}$ (bound GRID-cores), both for low perturbation amplitudes. The distributions of $M_{2D,bs}$ and M_{3D} are quite similar for all $\mathcal{M}$, except slightly more low mass cores are identified for 2D at large $\mathcal{M}$. When the thermal - gravitational energy condition is included in defining cores, the low-mass end of the distribution is removed; in Fig. 3.11, the 2D bound GRID-cores have almost exactly the same distributions as 3D bound GRID-cores.

Figure 3.12 (all GRID-cores) and Figure 3.13 (bound GRID-cores) show the median core mass (squares in figures) versus $\mathcal{M}$ from Figure 3.10 and 3.11, respectively. (We do not measure the peak because some of the histograms are irregular.) Figure 3.14 (all GRID-cores) and Figure 3.15 (bound GRID-cores) show the same median mass – $\mathcal{M}$

relation for high amplitude initial perturbations. The breadth of the distributions at each $\mathcal{M}$ is indicated by vertical bars: the lower bar is the difference between the median and the first quartile, and the higher bar is the difference between the third quartile and the median. In Fig. 3.12, 3.13 and Fig. 3.14, 3.15, we overlay lines showing the predicted critical mass at late stages (eq. 3.22 or 3.23, dashed line with $M \propto \mathcal{M}^{-1}$), and the prediction for the mass that has grown the most at early time (eq. 3.28 or 3.31, dot-dashed with $M \propto \mathcal{M}^{-1/2}$). The post-shock Bonnor-Ebert mass ($M \propto \mathcal{M}^{-1}$ from eq. 3.7) is similar to the late-stage critical mass.
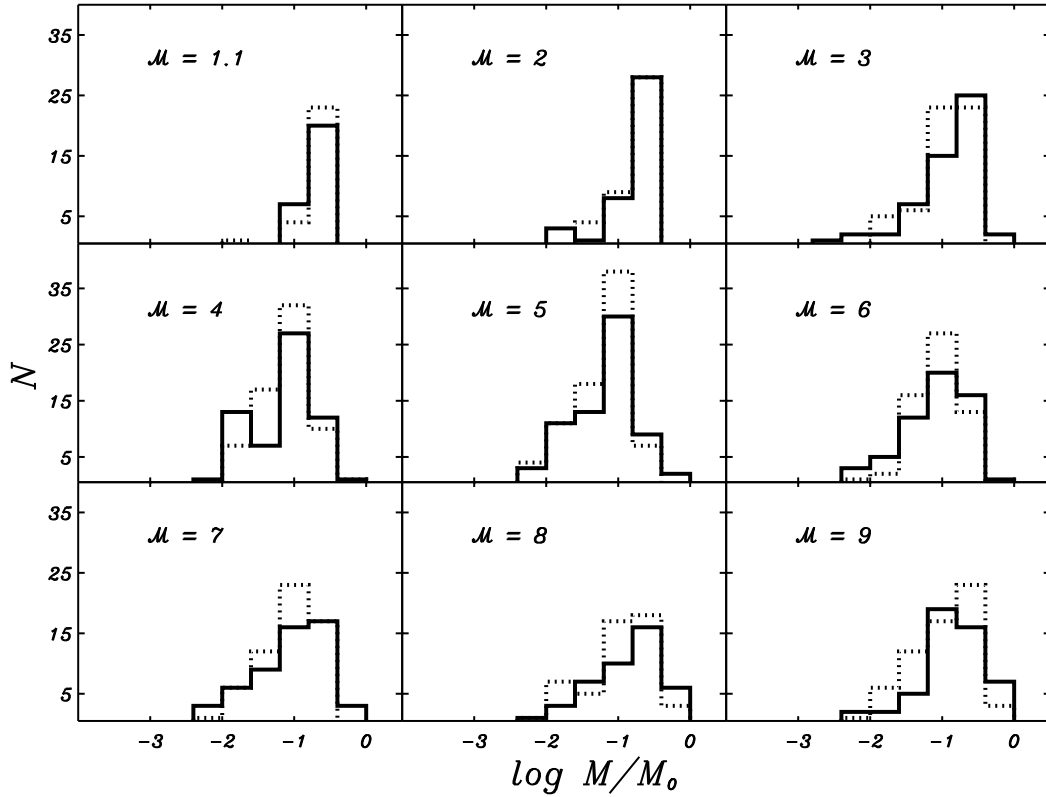
Figure 3.11: Same as in Figure 3.10, except for bound GRID-cores (i.e mass is $M_{3D,th}$ and $M_{2D,bs,th}$). When the condition $E_{th} + E_g < 0$ is applied, most of the low mass cores are eliminated, for every Mach number. The 2D bound GRID-cores have almost the same mass distribution as 3D bound GRID-cores.

As the Mach number increases, the post-shock density $\rho \approx \rho_0 \mathcal{M}^2$ is higher. This lowers the Jeans length (as well as the Jeans mass and Bonnor-Ebert mass), permitting
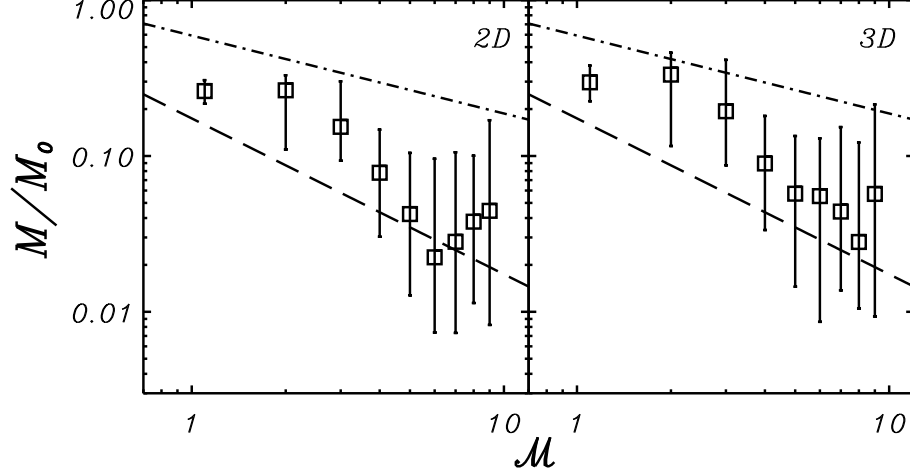
Figure 3.12: Median GRID-core mass M versus Mach number $\mathcal{M}$ of the inflow. The left panel is for 2D GRID-cores ($M_{2D,bs}$) and the right panel for 3D GRID-cores (M_{3D}). Vertical bars indicate quartiles of the distribution. Also shown is the expected mass dependence for early gravitational fragmentation given by equation (3.28) (with $M \propto \mathcal{M}^{-1/2}$, dot-dashed), and late gravitational fragmentation given by equation (3.22) (with $M \propto \mathcal{M}^{-1}$, dashed). The critical Bonnor-Ebert mass at the post-shock density (see eq. 3.7) is similar to the late-stage prediction ($M \propto \mathcal{M}^{-1}$, dashed). The relation between median core mass and $\mathcal{M}$ is quite similar for 2D and 3D cores. Core mass declines with increasing Mach number $\mathcal{M}$, lying between the $M \propto \mathcal{M}^{-1/2}$ (early stage) and $M \propto \mathcal{M}^{-1}$ (late stage) fragmentation predictions.

smaller (but denser) cores to form at high $\mathcal{M}$ compared to low $\mathcal{M}$. However, high mass cores can still form at high $\mathcal{M}$, as is evident in Figure 3.10 and 3.11 and the quartiles shown in Figures 3.12 – 3.15: at high $\mathcal{M}$, the histograms extend to low mass, but the high mass part of the distribution is still present. This is consistent with the expectation that any scale above the critical scale can grow more nonlinear due to self-gravity (see eqs. 3.12 - 3.17).

Based on Figures 3.12 – 3.15, we also note that the median mass versus $\mathcal{M}$ relations are quite similar whether cores are identified with the 2D or 3D gravitational potential. This is true for low or high amplitude perturbations, for both all GRID-cores and bound GRID-cores. This evidently shows that 2D cores have similar statistical properties to the 3D cores. Since the GRID algorithm is easy to implement for observational data, it appears to be a promising method for finding cores. An IDL implementation of our
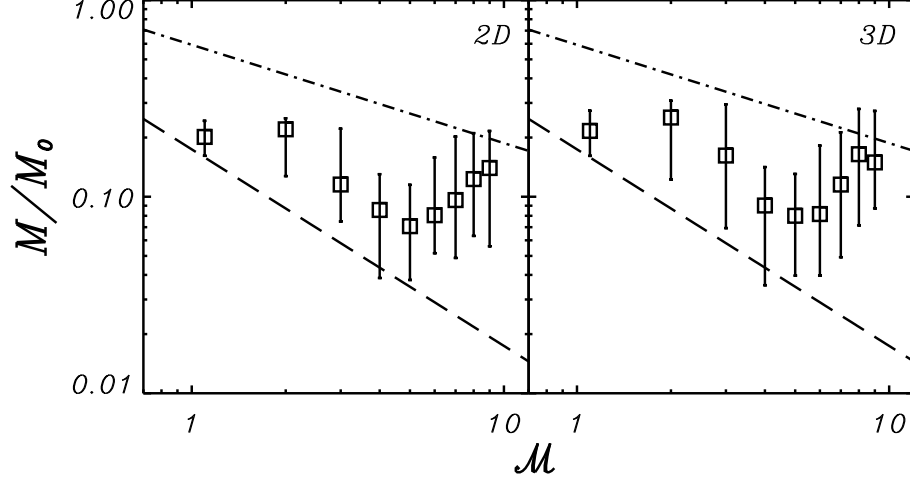
Figure 3.13: Same as in Figure 3.12, but for bound GRID-cores ($E_{\text{th}} + E_g < 0$, i.e. M is $M_{\text{2D,bs,th}}$ or $M_{\text{3D,th}}$).

GRID-core algorithm for use with observed data (FITS files containing surface density maps) is available from the authors.
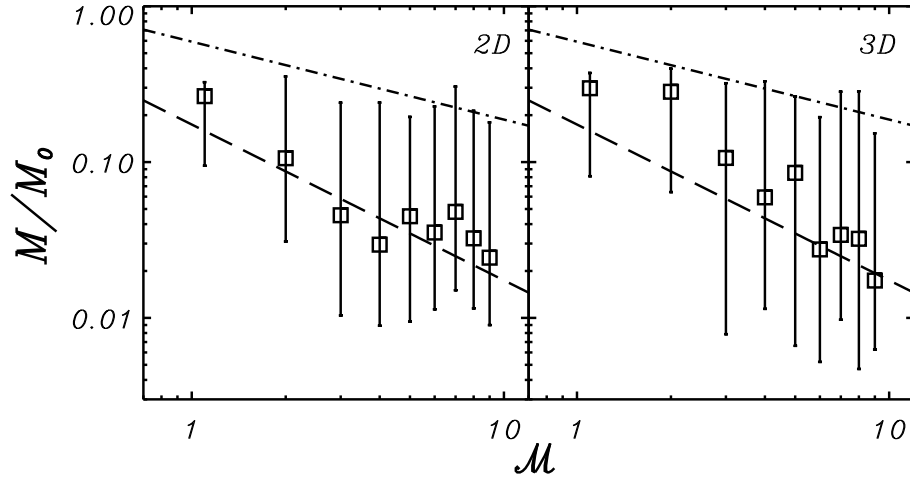
Figure 3.14: Median GRID-core mass $M_{\text{2D,bs}}$ and M_{3D}, as shown in Figure 3.12, but for high amplitude initial perturbations. The median masses are slightly smaller than for low amplitude initial perturbations, but follow a similar trend.

Median masses for GRID-cores decline with increasing Mach number for both low and high amplitude perturbations (see Figs. 3.12, 3.14). These median masses generally lie above the values predicted from equations (3.7), (3.19) and (3.22) ($M \propto \mathcal{M}^{-1}$) at late stages and below the values predicted from equation (3.28) ($M \propto \mathcal{M}^{-1/2}$) at early stages.

The median GRID-core masses for high amplitude perturbations are slightly smaller than those for low amplitude perturbations, and the range of core masses for a given Mach number are larger. This reflects the fact that the percentage of small cores is higher when the perturbation amplitudes are higher. GRID-cores are identified based on the gravitational potential, and this potential reflects density structure, which arises from both turbulent and gravitational processes. Even without gravity, smaller scale masses would be expected in the higher-$\mathcal{M}$ models because of their high turbulent amplitudes. For our simulations, the input perturbation amplitude at scale l is $\delta v_{1D}(l) = (l/L_J)^{1/2}(\mathcal{M}/3)^{1/2} c_s$ at 100% amplitude of perturbation (cf. eq. 3.43). Structures at scales l for which turbulent perturbations are supersonic will, even in the absence of gravity, be more prominent than those at smaller scale. For our adopted scaling of input perturbations with $\mathcal{M}$, the sonic scale varies as $l_{sonic} \propto L_J/\mathcal{M}$, so that the mass at the sonic scale varies $\propto \Sigma(t) l_{sonic}^2$. With $\Sigma(t) \propto \mathcal{M} t_{coll}$ and $t_{coll} \propto \mathcal{M}^{-1/2}$ (see eq. 3.29 and below), this predicts $M_{sonic} \propto \mathcal{M}^{-3/2}$. For later time $t \sim t_J$ (comparable to the flow crossing time for a cloud with $\alpha_{vir} = 1 - 2$), $M_{sonic} \propto \mathcal{M}^{-1}$. Thus, the sonic mass scale, and hence the mass scale of nonlinear structures induced purely by turbulence, is expected to decline with increasing $\mathcal{M}$.
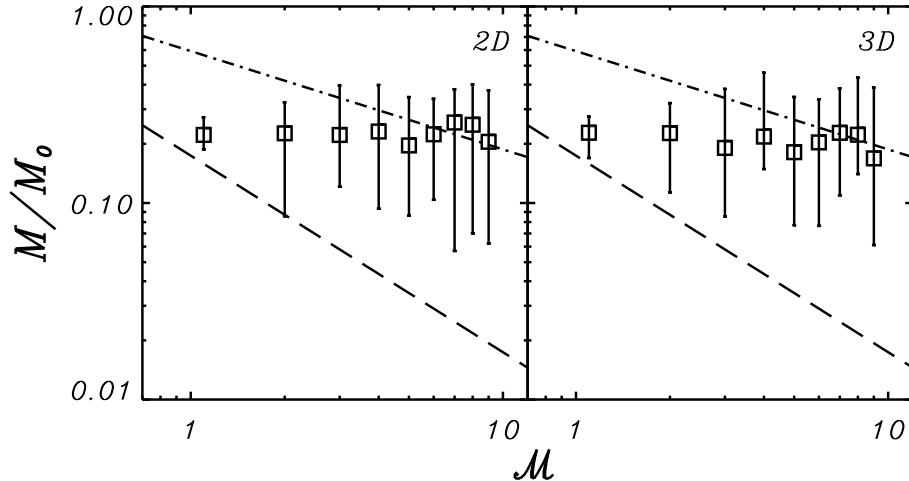
Figure 3.15: Median bound GRID-core mass $M_{2D,bs,th}$ and $M_{3D,th}$ (i.e. $E_{th} + E_g < 0$) as in Figure 3.13, but for high amplitude initial perturbations.

For bound GRID-cores, the median mass vs. $\mathcal{M}$ decreases and then increases, for low amplitude perturbations (Fig. 3.13), and is nearly flat for high amplitude perturbations (Fig. 3.15). The high median mass at high $\mathcal{M}$ for bound GRID-cores may be due to a combination of effects, including numerical resolution and nonlinearity. The characteristic scale for self-gravitating perturbations decreases with increasing Mach number (either as $r \propto \mathcal{M}^{-1/2}$ for the most-grown core or $r \propto \mathcal{M}^{-1}$ for critical perturbations; see Section 2). At high $\mathcal{M}$, this may approach or fall below the minimum scale $r_{\min} = 4$ zones $= 0.016 L_J$ that we require for the GRID-core radius to be well resolved. Since the post-shock density is $\propto \mathcal{M}^2$, the GRID-core mass would then increase at least $\propto \mathcal{M}^2 r_{\min}^3$ at sufficiently high $\mathcal{M}$. In addition, larger-scale, higher-mass regions initially have higher amplitude perturbations than smaller-scale regions, because of the input power spectrum with $\delta v \propto l^{1/2}$. If this initial "head start" allows the larger, more massive cores to become highly nonlinear before more rapidly-growing smaller-scale cores, the more massive cores will collapse (halting the simulation) before the lower-mass cores become strongly concentrated (with $E_{\rm th} < |E_g|$) internally. With implementation of sink particles such that the simulations need not to be halted when the most evolved core collapses, and $|E_g|$ can grow for low-mass cores, it will be possible to test whether the median mass of bound cores decreases with increasing $\mathcal{M}$, similar to Figs. 3.12 and 3.14.

Figure 3.16 shows the GRID-core radii (as defined in Section 3) versus Mach number, and Figure 3.17 shows the bound GRID-core radii versus Mach number; these are for cases with low amplitude initial perturbations. Overall, the median radii for all GRID-cores and bound GRID-cores decrease towards higher $\mathcal{M}$. This is consistent with expectations: high Mach number yields high post-shock density, and hence a smaller Jeans length; in addition, the higher amplitude of input turbulence at higher $\mathcal{M}$ makes the sonic scale smaller. The prediction for core radius based on turbulence alone would be the sonic scale from Equation (3.43): $r_{\rm eff} \propto l_{\rm sonic} \propto L_J / \mathcal{M}$. The first core to collapse is predicted to
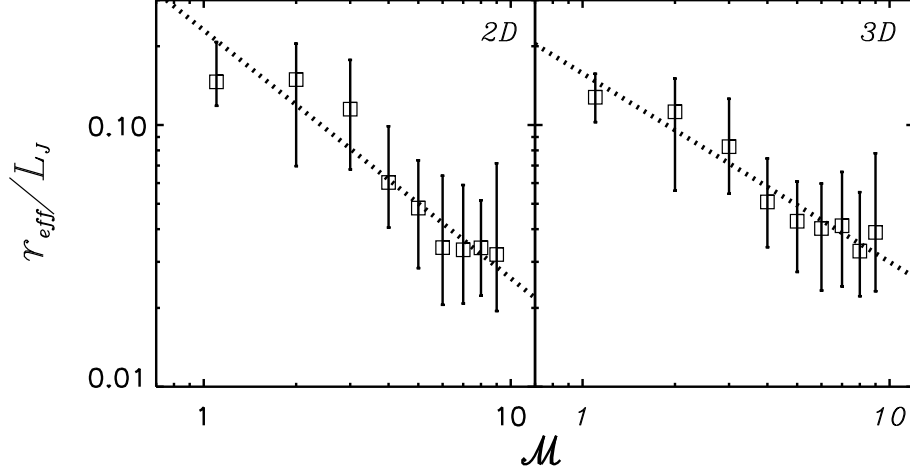
Figure 3.16: Median GRID-core radius versus Mach number $\mathcal{M}$ for low amplitude initial perturbations. Core sizes are defined using the largest closed contours of the gravitational potential in 2D (Φ_{2D}, left) and 3D (Φ, right). Vertical bars indicate quartiles of the distribution. The dotted lines are power-law fits: $r_{\text{eff,2D,bs}}/L_J = 0.23_{0.18}^{0.29}\mathcal{M}^{-0.95\pm0.13}$ and $r_{\text{eff,3D}}/L_J = 0.16_{0.14}^{0.18}\mathcal{M}^{-0.72\pm0.07}$.
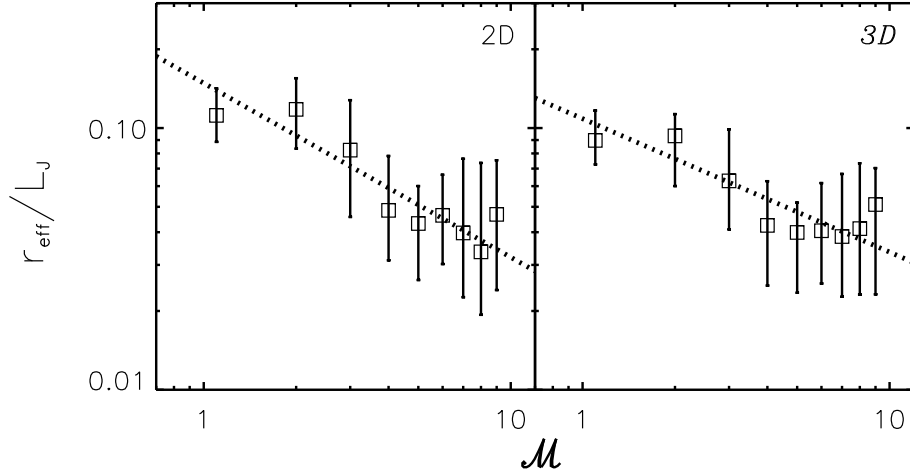
Figure 3.17: Same as in Figure 3.16 but for bound GRID-cores ($E_{\text{th}} + E_g < 0$). The power-law fits are $r_{\text{eff,2D,bs,th}}/L_J = 0.15_{0.12}^{0.18}\mathcal{M}^{-0.67\pm0.10}$ and $r_{\text{eff,3D,th}}/L_J = 0.11_{0.10}^{0.12}\mathcal{M}^{-0.61\pm0.08}$

.

have $\lambda_m \propto \mathcal{M}^{-1/2}$ from equation (3.30). For late-time fragmentation, the relevant scale is the Jeans length in post-shock gas, which varies $\propto \mathcal{M}^{-1}$. For GRID-cores, the slopes are between these values, equal to -0.95 ± 0.13 for $r_{\text{eff,2D,bs}}$ and -0.72 ± 0.07 for $r_{\text{eff,3D}}$, for low amplitude initial perturbations. For bound GRID-cores, the power-law fit for me-

dian radius as a function of Mach number gives slope -0.67 ± 0.10 and -0.61 ± 0.08 for 2D and 3D respectively. These are comparable to the result $\lambda_m \propto \mathcal{M}^{-1/2}$ from Equation (3.30). Although the overall slopes are close to -0.5, we note that the relation flattens at $\mathcal{M} \gtrsim 5$, possibly due to our requirement that the effective radius must exceed 4 zones, or because the initial power spectrum favors larger cores.
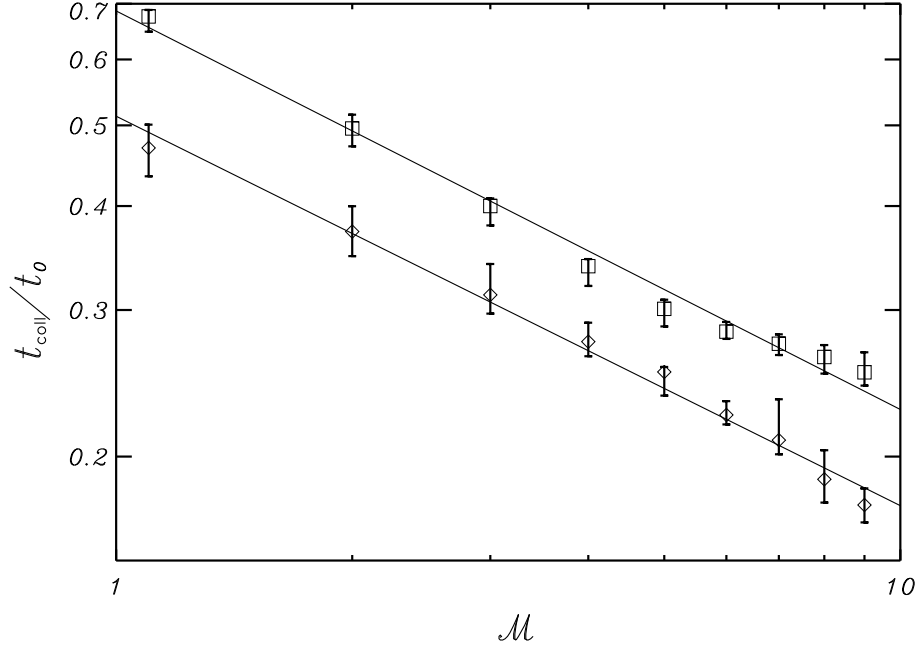
Figure 3.18: Collapse time of the most evolved core, t_{coll}, versus inflow Mach number $\mathcal{M}$ for low amplitude (squares) and high amplitude (diamonds) initial perturbations. Each value is the median of t_{coll} for 20 simulations for each $\mathcal{M}$. Vertical bars indicate quartiles of these 20 values of t_{coll}. The solid line least-squares fits are: $t_{\text{coll}}/t_0 = 0.69 \mathcal{M}^{-0.48}$ (low amplitude) and $t_{\text{coll}}/t_0 = 0.51 \mathcal{M}^{-0.47}$ (high amplitude). The scaling is comparable to $t_{\text{coll}} \propto \mathcal{M}^{-0.5}$, as predicted by equation (3.29). The simulation time unit t_0, based on the mean inflow density, is given in equation (3.6).

Figure 3.18 shows the median collapse time of the most evolved core vs. Mach number, for both low and high amplitude initial perturbations. They both follow power laws close to $t_{\text{coll}} \propto \mathcal{M}^{-1/2}$, consistent with the time scale (see eq. 3.29) predicted for growth of self-gravitating modes up to a given amplification Γ_{max}. The coefficients for low amplitude initial perturbations and high amplitude initial perturbations are 0.69 and 0.51, respectively, compared to 0.34 from equation (3.29) taking $\Gamma_{\text{max}} = 1$. With high am-

plitude initial perturbations, cores collapse earlier because the seed perturbations need not grow as much. Note that the naive expectation based on the Jeans time, taking $\rho_{\text{post-shock}} \propto \mathscr{M}^{-2}$, would yield a steeper dependence $t \propto \rho_{\text{post-shock}}^{-1/2} \propto \mathscr{M}^{-1}$. Based on Fig. 3.18, it is evident that the first cores in higher $\mathscr{M}$ cases collapse when the layer as a whole is only barely self-gravitating ($t_{\text{coll}}/t_0 \sim 0.2 - 0.3$, compared to $t_{\text{sg}} \approx 0.22 t_0$ from eq. 3.11), whereas the layer is more strongly self-gravitating at the first collapse for low-$\mathscr{M}$ cases.
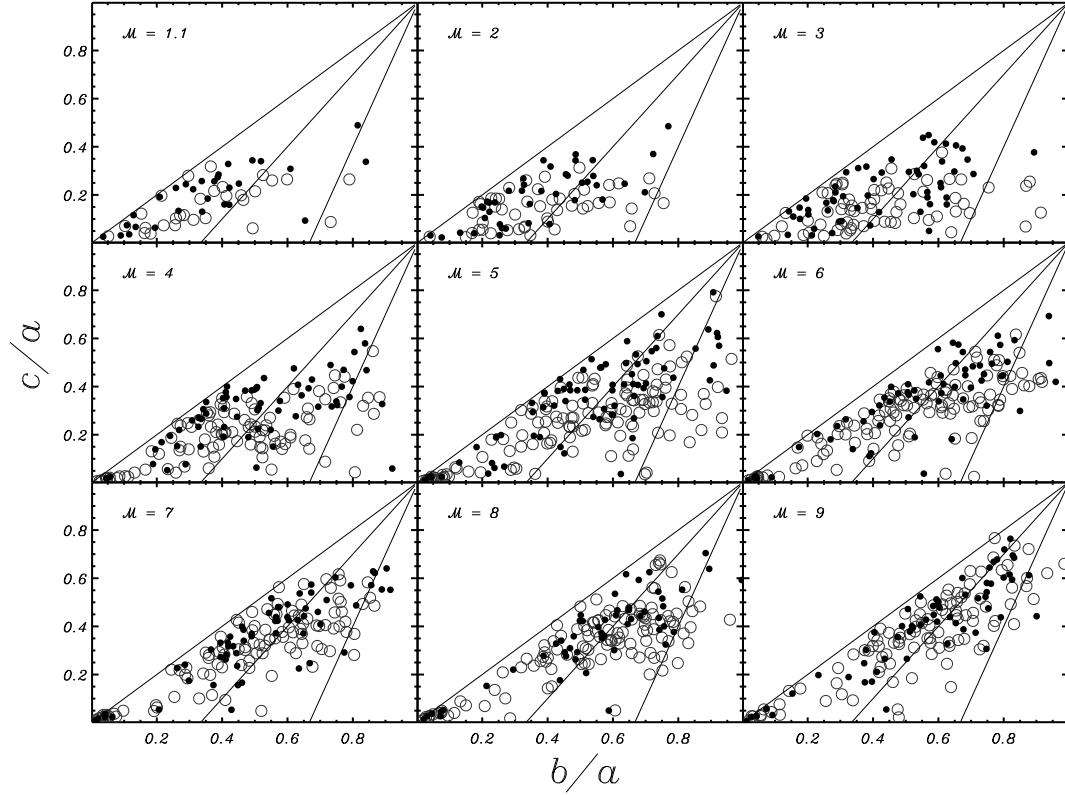
Figure 3.19: Distribution of three-dimensional core aspect ratio for each Mach number for low amplitude initial perturbations. Cores lying on $c/a = b/a$ are formally prolate and along $b/a = 1$ are formally oblate. We subdivide (see diagonal lines) and classify as follows: approximately prolate (between $c/a = 1$ and $c/a = 1.5b/a - 0.5$), triaxial (between $c/a = 1.5b/a - 0.5$ and $c/a = 3b/a - 2$) and approximately oblate (between $c/a = 3b/a - 2$ and $b/a = 1$). Open circles are GRID-cores defined by the gravitational potential contours alone. Dots are bound GRID-cores, with the additional requirement $E_{\text{th}} + E_g < 0$.

The shape of a core can be characterized by the eigenvalues of the moment of inertia

tensor $I_{ij} \equiv \int \rho x_i x_j d^3 \mathbf{x}$ (e.g. Gammie et al. 2003; Nakamura & Li 2008). Let a, b and c be the lengths of the principal axes and $a \geq b \geq c$. Then a prolate core has $b/a = c/a$, and an oblate core has $b/a = 1$. We have computed the moment of inertia and aspect ratios for all the cores identified in our simulations. For example, the aspect ratios of the most evolved cores shown in Figures 3.1 and 3.3 are $b/a = 0.39, c/a = 0.25$ for the $\mathcal{M} = 1.1$ model and $b/a = 0.28, c/a = 0.25$ for the $\mathcal{M} = 5$ model. They are both (approximately) prolate according to the classification of Gammie et al. (2003).
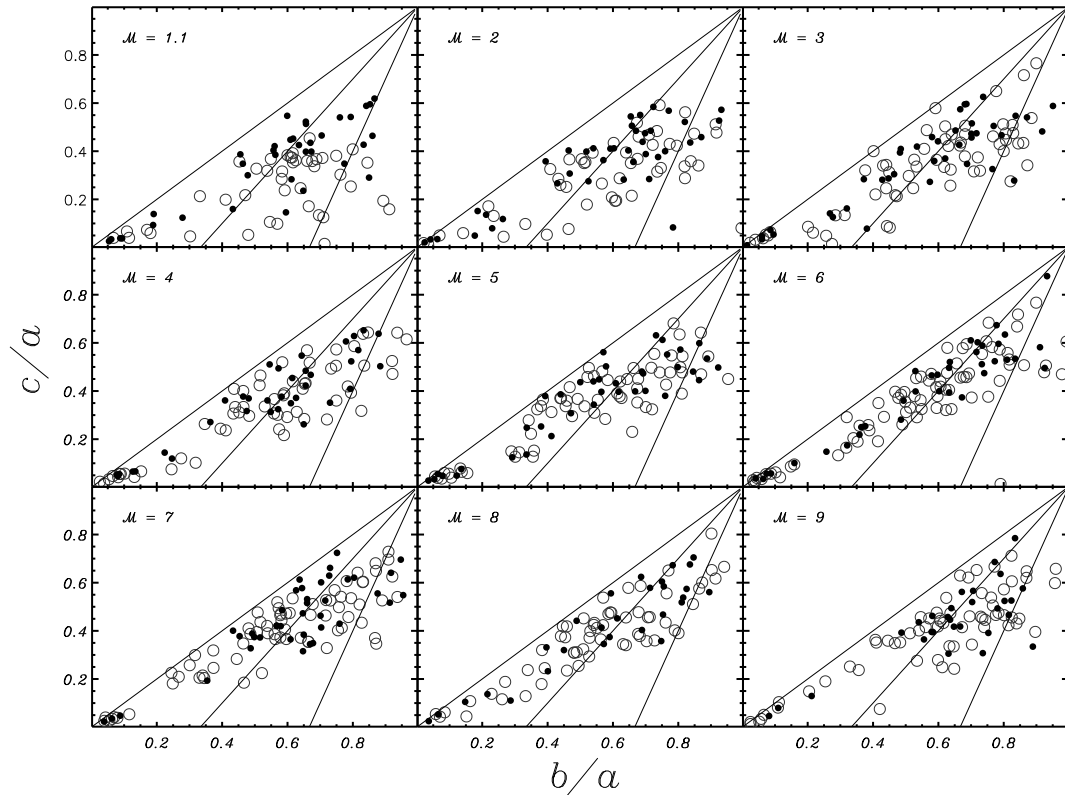
Figure 3.20: Same as Figure 3.19 but for high amplitude initial perturbations.

Figure 3.19 and Figure 3.20 show the distribution of core aspect ratios for each $\mathcal{M}$ for low and high amplitude initial perturbations respectively. Open circles represent GRID-cores, and dots represent bound GRID-cores. These distributions show a number of interesting features and trends. First, only a small portion of cores are oblate for each $\mathcal{M}$, for both low and high amplitude perturbations. Second, more oblate-like cores appear

when the initial perturbation amplitudes are higher. For low amplitude perturbations, at $\mathcal{M} = 1.1$ and 2, c/a and b/a are mostly ≤ 0.5, i.e. approximately prolate. But at larger $\mathcal{M}$ for low amplitude initial perturbations, and all $\mathcal{M}$ for high amplitude perturbations, there are many cores in the triaxial and oblate regions. Also, large and massive cores tend to be more prolate. For low amplitude perturbations, at $\mathcal{M} = 1.1$, almost all the cores formed are prolate and no small cores form (compared to high Mach number cases). The reason that the distribution is more oblate for higher amplitude perturbation (large $\mathcal{M}$ for low amplitude initial perturbations, and all $\mathcal{M}$ for high amplitude initial perturbations) is that more of the cores are at earlier stages of evolution. Figure 3.1 shows development of cores for $\mathcal{M} = 1.1, 5$ and 8. As is particularly clear for the stages shown in the $\mathcal{M} = 1.1$ model, structures are more oblate during the core-building stage than during the collapse stage. Cores evolve to become prolate when they collapse because the collapse happens first in the directions perpendicular to the larger scale filaments. For $\mathcal{M} = 1.1, 2$ models with low amplitude perturbations, only large cores form and they have evolved to the collapse stage and become prolate. Models with higher amplitude perturbations have a greater percentage of small cores that have not yet collapsed.

We can also examine the relationship between core structure and kinematics in our simulations. Figure 3.21 shows the projected density field, velocity field and the velocity dispersion field along the line-of-sight for the $\mathcal{M} = 5$ model shown in Fig. 3.6. We "view" the simulation at angles $0°, 30°$ and $60°$ with respect to the z axis, tilting toward the x-axis. The white contours mark the regions identified as GRID-cores, and the orange contours mark the bound GRID-cores. The projected density field is smeared as the tilt angle θ increases. Since $\langle v_{\text{los}} \rangle = \langle v_x \rangle \sin(\theta) + \langle v_z \rangle \cos(\theta)$, with $\langle v_z \rangle = 0$ and the contribution from $\langle v_x \rangle$ small at θ small, no obvious pattern is seen for $\langle v_{\text{los}} \rangle$ at $\theta = 0°$ and $30°$. At $\theta = 60°$, when the $\langle v_x \rangle$ contribution becomes larger, converging flow patterns similar to those seen in Fig. 3.2 become apparent, especially surrounding the diagonal line of small cores. As

previously discussed, converging flows in the *x-y* plane create this high density filament, which then fragments into small cores.
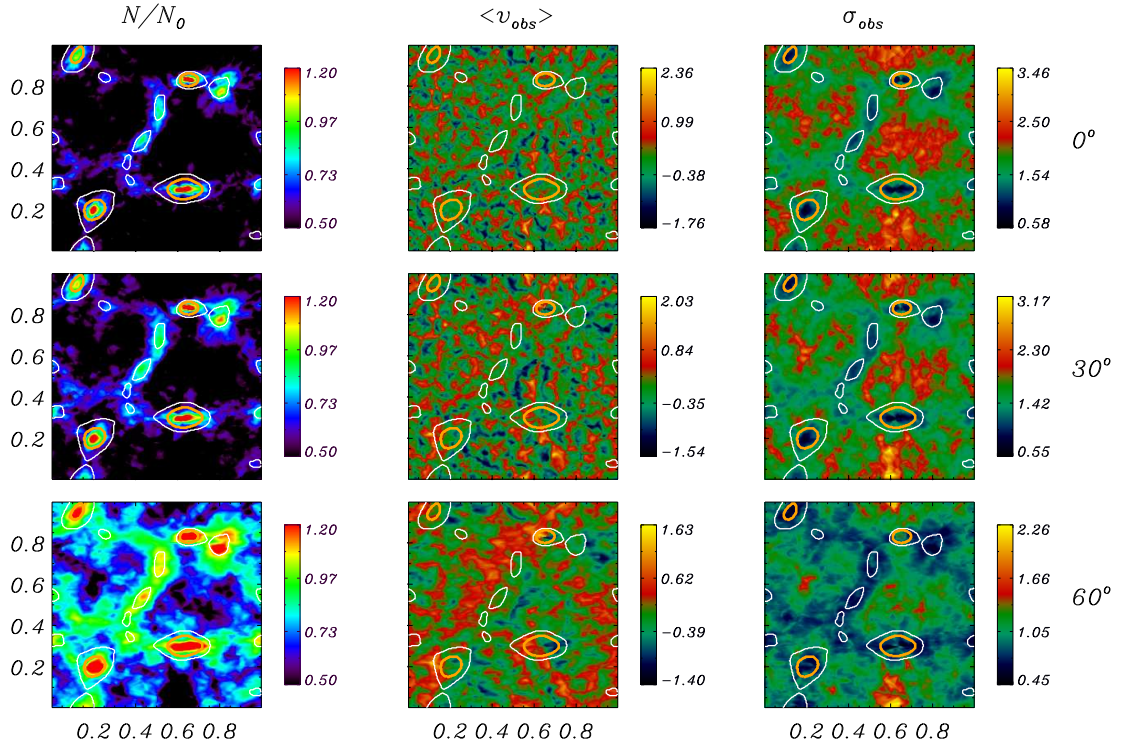
Figure 3.21: Observations of one of the $\mathcal{M} = 5$ models shown in Fig. 3.6 from different angles. The first column shows the surface density (color scale $\log\Sigma/\Sigma_0$); the second column shows the line-of-sight velocity and the third column shows the dispersion of the line-of-sight velocity (linear color scale, in units of c_s). The three rows from top to bottom show the observed fields for $\theta_{\text{tilt}} = 0°, 30°$ and $60°$ respectively. The white curves are the GRID-cores, and the orange curves are the bound GRID-cores. Note that core regions have low internal velocity dispersions.

As Figure 3.21 shows, the dispersions of the line-of-sight velocity of high density regions are generally subsonic, and are even smaller in the cores. Velocity dispersions are low in high-density regions for two reasons. First, if filaments lie between supersonic converging flows in the *x-y* plane, then post-shock velocities within the filaments will be subsonic. Second, weighting by density picks out regions that are physically small along the line-of-sight. The increase of linewidth with size means that if a region is smaller than its surroundings along the line-of-sight, then the linewidth will be smaller than that of its

surroundings. Thus, from a combination of low post-shock velocities (in the *x-y* plane), and spatially-limited scale (in the *z* direction), σ_{los} is low in filaments and lower in cores, as seen in Fig. 3.21.

3.7 Summary and Discussion

Stars form in GMCs pervaded by supersonic turbulence, and core formation theory must take these supersonic turbulent flows into account. In this work, we explore the physics of core formation in a dynamic environment, focusing on post-shock layers generated by collisions of supersonic flows. The framework we adopt – three-dimensional planar converging flows containing multi-scale turbulence – enables us to analyze the internal structure and kinematics of cores, and to investigate the relation between core properties and the inflow Mach number $\mathcal{M}$. We consider a range $\mathcal{M} = 1.1 - 9$, and conduct 180 simulations with different realizations of the initial turbulent power spectrum, in order to obtain a sizable statistical sample. In addition to core masses and sizes, we measure aspect ratios. To define cores, we introduce a new method based on the gravitational potential, and compare properties of cores identified using Φ (from the volume density) and Φ_{2D} (from the plane-of sky projected surface density).

Unlike previous studies of core evolution that begin with pre-existing cores, the present models include formation stages. Our initial density is uniform everywhere, and cores grow, via self-gravity, from turbulence-induced perturbations within the post-shock layer; when the Mach number is high, initial growth of density perturbations is aided by shock-driven hydrodynamic instabilities. Based on a set of spherically-symmetric numerical simulations, Gong & Ostriker (2009) proposed four stages for core evolution in dynamic environments: core building, core collapse, envelope infall, and late accretion. The key features during core building and collapse described in Gong & Ostriker (2009) are ver-

ified here, for more realistic geometry. As the supersonic flows converge in a plane, two reversed shocks propagate outwards. With its high mean density, the stagnation layer between these two shock fronts becomes an incubator for self-gravitating cores. When these cores become sufficient stratified, they collapse. We halt the simulations at the instant of singularity formation in the most evolved core, because the time step becomes very short.

Based on the analysis of our simulations, our chief conclusions are as follows:

1. Cores with realistic properties are able to form in post-shock dense layers within turbulent GMCs. Core building to become supercritical takes ~ 10 times as long as the subsequent "outside-in" collapse stage, which lasts a few $\times 10^5$ yr. The duration of the supercritical stage is consistent with observations of prestellar core lifetimes (Enoch et al. 2008; Evans et al. 2009; Ward-Thompson et al. 2007).

2. At the time of singularity formation, the radial density profile within cores approaches the Larson-Penston asymptotic solution $\rho = 8.86c_s^2/(4\pi G r^2)$ and the velocity approaches the Larson-Penston limit $-3.28c_s$. This is consistent with previous studies of spherical core collapse (see Section 1 for references). Tilley & Pudritz (2004) also found that $\rho \propto r^{-2}$ in their most massive cores, for turbulent simulations. As in Gong & Ostriker (2009), we therefore conclude that the Larson-Penston asymptotic solution is an "attractor" for core collapse, no matter how the collapse is initiated.

3. Prior to collapse, the velocities within dense cores remain subsonic, in spite of the highly-supersonic flows that create them. This is true both for the ordered inflow, and for the mean internal velocity dispersion. This result is consistent with observations that most cores have subsonic non-thermal velocity dispersions (André et al. 2007; Caselli et al. 2002; Goodman et al. 1998; Kirk et al. 2007; Lada et al. 2008; Myers 1983; Tafalla et al. 2004). The velocity dispersion can increase quite sharply at the edge of the core in our models (see Fig. 3.21), intriguingly similar to a sharp transition seen in NH_3 observations by Pineda et al. (2010) for the B5 core in Perseus. From some orientations, velocity

106

dispersions in filaments containing cores may also be lower than in the surrounding gas (cf. Fig. 3.21).

4. At sub-pc scales, turbulent velocity perturbations (whether super- or subsonic) induce density perturbations that can grow strongly if the density is high enough for self-gravity to be important. In post-shock layers, turbulence and self-gravity collect gas into long, thin filamentary structures at the same time as the highest density regions within the filaments grow to become centrally-condensed cores. These filamentary structures containing embedded cores are similar to the structures in the Aquila rift and Polaris Flare clouds observed by *Herschel* (André et al. 2010; Men'shchikov et al. 2010).

5. Using the gravitational potential to identify cores is advantageous because it enables a core definition based on dynamical principles. For numerical simulations, the gravitational potential may be computed from the volume density (yielding Φ) or from the projected surface density (yielding Φ_{2D}). We show for our models that cores defined using Φ and Φ_{2D} are nearly the same, both for GRID-cores (defined by the largest closed potential isosurfaces) and bound GRID-cores (which additionally require $E_{th} + E_g < 0$). Since Φ_{2D} can be computed for observed clouds, using potential contours offers a promising new core identification method for application to high-resolution molecular cloud maps. IDL code implementing our GRID-core algorithm, suitable for application to observed data, is available from the authors.

6. We find that the range of core masses that forms increases as the Mach number $\mathcal{M}$ increases. Physically, this is because a larger range of spatial scales has significant perturbations when the turbulence amplitude is higher, and because the minimum mass to be gravitationally unstable decreases as the density in the shocked layer increases. Basu et al. (2009) also found broader mass distributions when the turbulent amplitude is increased. At high Mach number, GRID-core masses range between $\sim 10^{-3} - 1 M_J$, corresponding to $\sim 0.05 - 50$ M$_\odot$ for typical GMC conditions.

7. Analytical arguments (see Section 2) suggest that the first core to collapse will have mass $M \propto \mathcal{M}^{-1/2}$, and that at late times, the minimum mass core will vary as $M \propto \mathcal{M}^{-1}$. Our numerical results for median core masses as a function of $\mathcal{M}$ lie between these two relations. When the core definition includes the condition that $E_{\text{th}} + E_g < 0$, the median mass increases at the largest Mach number. This may be due to the nonlinear "head start" of massive cores, such that lower mass cores have not yet become concentrated when the first core collapses (and the simulation is stopped).

8. Analytical arguments (see Section 2) suggest that the effective core radius will decline with increasing Mach number, with powers between $r_{\text{eff}} \propto \mathcal{M}^{-1/2}$ and $r_{\text{eff}} \propto \mathcal{M}^{-1}$. Our numerical results show a decrease of r_{eff} with $\mathcal{M}$ in this range. For bound GRID-cores ($E_{\text{th}} + E_g < 0$), the relation is shallower than for GRID-cores defined by gravitational potential alone.

9. The time for the first core to collapse in our simulations depends on Mach number, with $t_{\text{coll}} \propto \mathcal{M}^{-1/2}$, and a slightly smaller coefficient for high-amplitude initial perturbations (see Fig. 3.18). This scaling is consistent with analytic predictions for gravitational instability in a shocked converging flow (see eq. 3.29). For high $\mathcal{M}$, as is observed in GMCs, the first cores could collapse within a few Myr of cloud formation. For high $\mathcal{M}$, the first cores collapse when the shocked layer containing them is only barely self-gravitating; this suggests that collections of stars can begin to form individually before they collapse together to create a cluster.

10. A very small portion of cores are oblate, while most cores are prolate or triaxial. Large cores are preferentially prolate. The triaxiality of most cores is consistent with previous results from turbulent hydrodynamic and MHD simulations (Gammie et al. 2003; Li et al. 2004; Nakamura & Li 2008; Offner et al. 2008). We also find that core shapes change as they evolve, from more oblate during early stages to more prolate during collapse. For high initial perturbation amplitudes, the distributions have a higher proportion

of oblate cores because small cores are less evolved (at the time the first core collapses),
compared to those in models with low initial perturbation amplitudes.

As noted above, the current models have provided evidence that the masses of cores
that form depend not just on the mean Jeans mass in a cloud, but also on the cloud's level
of internal turbulence at large scales, σ_v. Equations (3.22) and (3.23) suggest that at late
times, the characteristic core mass will follow $M_c \propto \sigma_v^{-1} \rho_0^{-1/2} T^2$, where ρ_0 is the mean
density in the cloud. For the current simulations, however, we halt at the instant when the
most evolved core collapses (because the time step becomes very short). This limits the
condensation of small cores; they are present, but not yet strongly bound. In order to fully
test the dependence of M_c on cloud parameters, it is necessary to implement sink particles
(e.g. Federrath et al. 2010; Krumholz et al. 2004) so that the simulation can run until all
the "eligible" cores in the post-shock region have had the opportunity to collapse. Includ-
ing sink particles, as well as studying shocked converging flows within larger turbulent
clouds via mesh-refined simulations, represent important avenues for future research.

acknowledgments

Chapter 4

Implementation of Sink Particles in the *Athena* Code

Abstract

We describe implementation and tests of sink particle algorithms in the Eulerian grid-based code *Athena*. Introduction of sink particles enables long-term evolution of systems in which localized collapse occurs, and it is impractical (or unnecessary) to resolve the accretion shocks at the centers of collapsing regions. We discuss similarities and differences of our methods compared to other implementations of sink particles. Our criteria for sink creation are motivated by the properties of the Larson-Penston collapse solution. We use standard particle-mesh methods to compute particle and gas gravity together. Accretion of mass and momenta onto sinks is computed using fluxes returned by the Riemann solver. A series of tests based on previous analytic and numerical collapse solutions is used to validate our method and implementation. We demonstrate use of our code for applications with a simulation of planar converging supersonic turbulent flow, in which multiple cores form and collapse to create sinks; these sinks continue to interact and accrete from their surroundings over several Myr.

110

4.1 Introduction

Gravitational collapse is a common feature of many gaseous astrophysical systems, and specialized methods are required in order to follow collapse in time-dependent hydrodynamic simulations. These numerical issues are particularly important in studies of star formation. As gravitational collapse develops, material converges to a central point from all directions to create a large density peak. For simulations that follow the formation of multiple self-gravitating prestellar cores within large-scale clouds, the true structures that form as a consequence of core collapse are generally so small that the profile surrounding each collapse center becomes un-resolvable for grid-based codes, even if adaptive mesh refinement (AMR) is adopted. For example, stellar radii are $\sim 10^{11}$cm, whereas that of a giant molecular cloud (GMC) is $\sim 10^{20}$cm. With a dynamic range $> 10^9$, it is not possible to spatially resolve a central post-shock protostar at the same time as capturing the large scale flows that lead to its formation, when multiple collapse centers are simultaneously present. When the central density in a collapsing region becomes too large, gradients in gas pressure and gravity from the central cell to the neighboring cells cannot be resolved, such that correct mass and momentum fluxes cannot be computed by the numerical solvers. A simulation cannot continue under these conditions.

The huge dynamic range involved in gravitational collapse can also lead to difficulties due to the time step restriction by the Courant condition (Richtmyer & Morton 1994). The time-scale set by self-gravity varies $\propto \rho^{-1/2}$, so that an increase by a factor of $> 10^6$ in density relative to ambient conditions (as would apply within the centers of collapsed cores) implies a decrease in the time step by a factor $\sim 10^3$.

A practical way to deal with the above difficulties, for numerical models that are focused on large-scale dynamics, is to establish a minimum spatial resolution and introduce sink particles. When gravitational collapse occurs, the unresolved high density peaks are

eliminated from the grid and replaced with sink particles. After a sink is created, the material can flow smoothly toward the center of collapse, with the profile remaining well resolved near the sink. Subsequent to the creation of sinks, gas and sink particles are integrated simultaneously, including mutual gravitational forces. Provided that the flow onto sinks is supersonic, introducing them will not affect the dynamics of the upstream flow. Accretion onto sinks should be implemented in a way that conserves total mass and momentum of the system.

Bate et al. (1995) first introduced sink particle techniques in a smoothed particle hydrodynamics (SPH) code. Krumholz et al. (2004) and Federrath et al. (2010) implemented sink particles in the grid-based codes ORION and FLASH, respectively, and extensively discuss tests of their methods. In the past several years, similar implementations have been made for a number of other well-established codes, such as ENZO (Wang et al. 2010), RAMSES (Dubois et al. 2010; Teyssier et al. 2011), and GADGET (Jappsen et al. 2005). Krumholz et al. (2004), Wang et al. (2010), Dubois et al. (2010), Teyssier et al. (2011) adopt the same methodology, including the criteria for creation of sink particles and the accretion rate onto sink particles. Vázquez-Semadeni et al. (2011) used an early version of the implementation in FLASH described by Federrath et al. (2010). In these implementations, Krumholz et al. (2004), Federrath et al. (2010), Wang et al. (2010), Padoan & Nordlund (2011), Vázquez-Semadeni et al. (2011) mainly focus on star formation simulations; Dubois et al. (2010), Teyssier et al. (2011) create sink particles to replace super-massive black holes in cosmological simulations.

In this chapter, we present details of our implementation and tests of sink particles in the grid-based code *Athena* (Gardiner & Stone 2005, 2008; Stone et al. 2008; Stone & Gardiner 2009). In Section 2, we begin by introducing the Eulerian code and outlining our methods for implementing sink particles. We physically motivate criteria we adopt for creating sinks, and describe our methods for treating gravity, accretion, merg-

ing, and orbit integration of sink particles. In Section 3, we present a series of tests of our methods. These include orbits of two particles, collapse of self-gravitating spheres with a range of initial conditions (including self-similar solutions, and converging supersonic flows). We demonstrate Galilean invariance of our methods. To illustrate the capabilities of our methods for typical applications, in Section 4 we consider evolution of a turbulent medium with a large-scale supersonic flow converging to create a dense slab. We follow the fragmentation of the slab into multiple cores, and the subsequent evolution of the system as sink particles are created and grow. Finally, Section 5 summarizes our presentation.

4.2   Numerical Methodology

4.2.1   *Athena* Code

For the simulations presented in this chapter we use the three-dimensional (3D) code *Athena* (Gardiner & Stone 2005, 2008; Stone et al. 2008; Stone & Gardiner 2009). *Athena* is a grid-based code that uses higher order Godunov methods to evolve the time-dependent equations of compressible hydrodynamics and magnetodynamics (MHD), allowing for self-gravity, radiative heating and cooling, and other microphysics, on either a Cartesian or cylindrical (Skinner & Ostriker 2010) grid. In this chapter, we only refer to the hydrodynamics and self-gravity capabilities of the code, with Cartesian coordinates. The hydrodynamics equations solved are the mass, momentum, and energy equations:

$$\frac{\partial \rho}{\partial t} + \nabla \cdot (\rho \, \boldsymbol{v}) = 0, \tag{4.1}$$

$$\frac{\partial (\rho \boldsymbol{v})}{\partial t} + \nabla \cdot (\rho \boldsymbol{v} \boldsymbol{v} + \mathbf{P}^*) = -\nabla(\Phi + \Phi_{\text{ext}}), \tag{4.2}$$

$$\frac{\partial E}{\partial t} + \nabla \cdot [(E + P)\boldsymbol{v}] = \rho \boldsymbol{v} \cdot \nabla(\Phi + \Phi_{\text{ext}}), \tag{4.3}$$

113

and the Poisson equation,

$$\nabla^2 \Phi = 4\pi G \rho, \tag{4.4}$$

where $\mathbf{P}^*$ is a diagonal tensor with $P^* \equiv P \overset{\leftrightarrow}{\mathrm{I}}$, and P is the gas pressure, E is the total energy density

$$E = \frac{P}{\gamma - 1} + \frac{1}{2}\rho v^2, \tag{4.5}$$

Φ is the gravitational potential of the gas, and Φ_{ext} is an external gravitational potential. In this chapter, we shall consider isothermal flows, in which the energy equation (4.3) is replaced by the relation $P = c_s^2 \rho$. Here $c_s^2 = kT/\mu$ is the square of the isothermal sound speed, for T the temperature and μ the mean mass per-particle.

To solve the Poisson equation under varying boundary conditions, we adopt three different gravity solvers. For periodic boundary conditions in all directions, we use the fast Fourier transformation (FFT) method. For boundary conditions that are periodic in-plane $(x-y)$ and open in the z-direction, we use the FFT method developed by Koyama & Ostriker (2009). For open boundaries in all directions, we use a new solver based on the method described in Hockney & Eastwood (1981), which employs FFTs in a zero-padded domain eight times as large as the computational box (see Appendix).

Athena also includes static mesh refinement (SMR), but we do not refer to these capabilities in the current work. Implementation of our sink particle algorithm with SMR will be discussed in a future publication.

4.2.2 Creation of Sink Particles

Different criteria for the creation of sink particles have been discussed in the past decade. A density threshold (Jappsen et al. 2005; Krumholz et al. 2004; Padoan & Nordlund 2011) is the simplest criterion for creation of a sink particle. High density regions may form in astronomical systems as a consequence of different physical processes, most importantly

strong supersonic shocks and gravitational collapse. If a high density region is not grav-itationally bound, it might subsequently be destroyed by large scale motions that induce rarefactions. Thus, care must be taken to select an appropriate density threshold, and to include additional criteria that must be satisfied before creating sink particles (Federrath et al. 2010).

Using AMR simulations, Truelove et al. (1997) showed that grid-scale numerical noise could grow to cause artificial self-gravitating fragmentation if the local Jeans scale $(L_J \equiv c_s(\pi/G\rho)^{1/2})$ is not resolved by at least four cells. This criterion gives a density threshold

$$\rho_{\text{Tr}} = \frac{\pi}{16} \frac{c_s^2}{G\Delta x^2}, \tag{4.6}$$

for Δx the simulation cell size.

The implementation of Krumholz et al. (2004) sets the threshold density for sink par-ticle creation in a cell to ρ_{Tr}. Banerjee et al. (2009) and Vázquez-Semadeni et al. (2011) adopt criteria that first checks whether density exceeds a threshold density and then checks if the zone in question is a local gravitational potential minimum. Bate et al. (1995) and Federrath et al. (2010) perform a series of checks including a density threshold check, a converging flow check, a local gravitational potential minimum check, and additional checks that evaluate whether a region is strongly self-gravitating. The converging-flow check of Federrath et al. (2010) requires that the flow surrounding a candidate zone is converging along all directions, stricter than the condition $\nabla \cdot v < 0$.

For simulations involving gravitational collapse, a sink particle should only be cre-ated at the center of a region that is collapsing. As the sink particle creation criteria of Krumholz et al. (2004) do not specifically limit particle creation to a single collapse center, they adopt the approach of merging the spurious sink particles within a given col-lapsing region so that one final sink particle is created inside each potential well. The extra criteria— checks for a local potential minimum or a gravitationally bound state —

adopted by Banerjee et al. (2009), Federrath et al. (2010) and Vázquez-Semadeni et al. (2011) further limit the initial creation of sink particles, so that only one sink particle is created for each local potential minimum. We shall adopt similar criteria to Federrath et al. (2010) to ensure that single sink particles are created inside regions that are collapsing.

Density threshold

Our choice of density threshold, ρ_{thr}, for sink particle creation is motivated by the well-known solution for self-gravitating collapse first obtained by Larson (1969) and Penston (1969) (hereafter LP). For collapse of an initially-static, gravitationally-unstable isothermal sphere, LP showed that a singular density profile

$$\rho_{\text{LP}}(r) = \frac{8.86 c_s^2}{4\pi G r^2} \tag{4.7}$$

is reached. Numerical studies with a range of initial conditions have shown that the LP asymptotic solution is in fact an "attractor" for isothermal core collapse, no matter how the collapse is initiated (Bodenheimer & Sweigart 1968; Burkert & Alves 2009; Foster & Chevalier 1993; Gómez et al. 2007; Hennebelle et al. 2003; Hunter 1977; Larson 1969; Motoyama & Yoshida 2003; Ogino et al. 1999; Penston 1969; Vorobyov & Basu 2005). Some of the above models start from static unstable configurations, and others from static, stable configurations that are subjected to an imposed compression, either from enhanced external pressure or a converging velocity field, or a core-core collision. These models all show that collapse starts from outside and propagates in, and that the central velocity is comparable to the value $-3.28 c_s$ at the time of singularity formation, when the density profile approaches the inverse-square LP asymptotic solution ρ_{LP}. Gong & Ostriker (2009, 2011) showed that the collapse of cores forming inside converging supersonic flows also approaches the LP solution, whether the flow is spherically symmetric or is turbulent, with no special symmetry. Gong & Ostriker (2009, 2011) also showed that the

duration of collapse (starting when the core is ~ 10 times the ambient density) is typically a free-fall time at the mean core density.

When collapse occurs, the LP profile would result in a density

$$\rho_{\text{LP}}(0.5\Delta x) = \frac{8.86}{\pi} \frac{c_s^2}{G\Delta x^2}.$$

(4.8)

at a distance $\Delta x/2$ from the center. We take this as the density threshold (ρ_{thr}) for sink particle creation. We note that this value is 14.4 times the value ρ_{Tr} of Equation (4.6). A potential concern is that this might lead to artificial fragmentation. However, we find (see section 4.3) that using the threshold from Equation (4.8), no additional particles are created compared to cases in which we instead adopt Equation (4.6) (ρ_{Tr}) for the sink particle density threshold. After a sink particle is created, all cells centered at $r < 2\Delta x$ become part of a "sink region" (see below), such that the density of cells exterior to the sink region satisfy the Truelove criterion, with $\rho_{\text{LP}}(2\Delta x) = 8.86c_s^2/(16\pi G\Delta x^2) < \rho_{\text{Tr}}$.

Our standard choice of density threshold is given by Equation (4.8). However, we have also tested other choices, as discussed in Section 4.3, and found similar results.

Control volume

Surrounding each sink particle is a sink control volume where the gas flow cannot be resolved. As a sink particle moves from one cell to another, the control volume moves with the sink particle, such that the sink particle is always located within the central zone of the cubic control volume. The sink control volume is generally set to $(3\Delta x)^3$ although we find similar results for value $(5\Delta x)^3$ and $(7\Delta x)^3$. The effective radius of the control volume is $\sim r_{\text{ctrl}}$, with $r_{\text{ctrl}} \equiv 1.5\Delta x$ for a control volume $(3\Delta x)^3$. As gravity is unresolved at the same scale, the same control volume is adopted for the particle-mesh algorithm we use to compute the sink particle's gravity (see section 2.4). Once a control volume has been created, it acts similar to ghost zones bounding the simulation domain. At every time step, the density, momentum, and energy of the cells inside each control volume are

reset using "outflow" boundary conditions (i.e. flow in the inward radial direction off the grid at the smallest radius) from the active grid (i.e. via extrapolation from surrounding non-sink zones).

Gravitational potential minimum check

If the density of a cell with integer indexes (i, j, k) exceeds ρ_{thr}, and its distance to any existing sink particle is larger than $2r_{\text{ctrl}}$, a "temporary" control volume is created surrounding it. This temporary control volume has same size as the real control volume for a sink particle. We then check if the central cell is a potential minimum inside this control volume (Federrath et al. 2010). If the potential minimum test is satisfied, we apply further tests.

Converging flow check

As in Federrath et al. (2010) but less restrictive, we test whether the candidate sink cell at the center of the control volume is surrounded by a converging flow: $\nabla \cdot v < 0$. Under most circumstances, the tests for high density, a gravitational potential minimum, and a converging flow would guarantee the region surrounding this cell is under gravitational collapse. However, under the special circumstance of a strong shock produced by a converging flow, all of the above criteria might be met, but a region would still disperse if the converging flow were not sustained until the region becomes gravitationally bound (Federrath et al. 2010); this would occur when the volume of the high-density post-shock region becomes sufficiently large.

Gravitationally bound state check

As a last check before sink particle creation, we test whether the total energy inside the temporary control volume is negative (Federrath et al. 2010):

$$E_{\text{grav}} + E_{\text{th}} + E_{\text{kin}} < 0, \qquad (4.9)$$

where E_{grav} is the gravitational potential energy, E_{th} is the thermal energy, and E_{kin} is the kinetic energy.

The control-volume gravitational energy is calculated as

$$E_{\text{grav}} = \sum_{ijk} \rho(i,j,k) \Delta\Phi(i,j,k), \qquad (4.10)$$

where $\Delta\Phi(i,j,k) = \Phi(i,j,k) - \Phi_0$ is the potential difference between the cell with integer index (i,j,k) and the potential at the "edge" of the local potential well, Φ_0. For Φ_0, we compute the average value of the potential in all zones immediately outside the temporary control volume.

The thermal energy and kinetic energy are calculated as follows:

$$E_{\text{th}} = \frac{3}{2} \sum_{ijk} \rho(i,j,k) c_s^2(i,j,k), \qquad (4.11)$$

$$E_{\text{kin}} = \frac{1}{2} \sum_{ijk} \rho(i,j,k) |v(i,j,k) - v_{\text{cm}}|^2; \qquad (4.12)$$

here v_{cm} is the velocity of the center of mass of the control volume.

If a cell passes all the checks above, a sink particle is created and a permanent control volume is tagged around it. The initial mass and momentum of the sink particle are set by the sums over all zones within the control volume. Note that the cells within the sink control volume are not modified either at the moment of sink creation or by subsequent accretion because they are effectively ghost zones; their values are updated at the same time as other boundary conditions (see Section 2.2.2). Also, as noted above, the sink

119

control volume is redefined whenever the sink particle moves to a new zone within the computational grid. However, the particle can move within a given cell without redefining the sink control volume.

4.2.3 Gas Accretion Onto Sinks

A key aspect of any sink particle implementation is to ensure that the gas accretion rate onto sinks is accurate. Krumholz et al. (2004) use the Bondi-Hoyle accretion formula to approximate the accretion rate, with the sound speed and flow velocity set by host cell values. The density ρ_∞ in the Bondi-Hoyle formula is set based on the mean density in a local accretion zone (see their section 2.4). Federrath et al. (2010) take a simpler approach, removing mass from any cell within the control volume to the sink particles if the density in that cell exceeds ρ_{Tr}.

Motivated by the concept of the sink region as "internal" ghost zones, in our algorithm the accretion rates of mass and momentum to each sink particle are calculated based on the fluxes returned by the Riemann solver at the interfaces between the control volume and the surrounding computational grid. Tests to confirm that the accretion rate agrees with analytic solutions are discussed in Section 3. As sink particles cross the border of one cell to enter the next cell, the mass and momentum differences between the new and old ghost zones are combined with the fluxes returned by the Riemann solver to conserve the mass and momentum of the whole simulation domain, including both gas and particles.

4.2.4 Integration and Merging of Sink Particles

Once they have been created, sink particle position and velocities must be integrated in time. To do this, we use the leapfrog method (e.g. Springel 2005), with updates over time

Δt given by:

$$U(\Delta t) = D\left(\frac{\Delta t}{2}\right) K(\Delta t) D\left(\frac{\Delta t}{2}\right),$$ (4.13)

or

$$U(\Delta t) = K\left(\frac{\Delta t}{2}\right) D(\Delta t) K\left(\frac{\Delta t}{2}\right).$$ (4.14)

Here $D(\Delta t)$ and $K(\Delta t)$ are the "drift" and "kick" operators respectively, and $D(\Delta t)$ updates a particle's position without changing its momentum, while $K(\Delta t)$ does the opposite; $U(\Delta t)$ is the time evolution operator for an interval Δt. Both drift-kick-drift (DKD, Equation (4.13)) and kick-drift-kick (KDK, Equation (4.14)) schemes are implemented. For all the simulations presented in this work, the KDK scheme is adopted because it is superior to the DKD scheme for variable time step (Springel 2005). The time step of the whole simulation is also restricted by the sink particle velocities: sink particles cannot travel further than one grid zone in one time step.

Velocity updates of the sink particles are set based on the gravitational field at the particle's (smoothed) location. This gravitational field must include a contribution from all the other particles, as well as from the gas. We use the triangular-shaped-cloud (TSC) scheme (Hockney & Eastwood 1981) to calculate the gravity produced by each particle as well as the force each particle feels. In this method the mass of each sink particle is smoothed to the n_{TSC}^3 cells surrounding it, where n_{TSC} is the number of cells used in one

direction. The weights along the x direction are expressed as follows:

$$
W_l^x(\Delta h) =
\begin{cases}
\dfrac{(1-2\frac{\Delta h}{\Delta x})^2}{2(n_{\text{TSC}}-1)^2}, & l = -\dfrac{n_{\text{TSC}}-1}{2} \\[18pt]
\dfrac{2(n_{\text{TSC}}+2l-1-2\frac{\Delta h}{\Delta x})}{(n_{\text{TSC}}-1)^2}, & l = -\dfrac{n_{\text{TSC}}-1}{2}+1,...,-1 \\[18pt]
\dfrac{2n_{\text{TSC}}-3-4(\frac{\Delta h}{\Delta x})^2}{(n_{\text{TSC}}-1)^2}, & l = 0 \\[18pt]
\dfrac{2(n_{\text{TSC}}-2l-1+2\frac{\Delta h}{\Delta x})}{(n_{\text{TSC}}-1)^2}, & l = 1,...,\dfrac{n_{\text{TSC}}-1}{2}-1 \\[18pt]
\dfrac{(1+2\frac{\Delta h}{\Delta x})^2}{2(n_{\text{TSC}}-1)^2}. & l = -\dfrac{n_{\text{TSC}}-1}{2}
\end{cases}
\tag{4.15}
$$

Here Δh is the x-distance between the sink particle and the center of the cell where it resides along the x dimension. The index l ranges from $-(n_{\text{TSC}}-1)/2$ to $(n_{\text{TSC}}-1)/2$ and the cell with $l = 0$ is where the sink particle resides. Taking $n_{\text{TSC}} = 3$, Equation (4.15) reduces the TSC weights described in Hockney & Eastwood (1981):

$$
W_{-1}^x = \frac{1}{8}\left(1 - \frac{2\Delta h}{\Delta x}\right)^2; \quad W_0^x = \frac{3}{4} - \left(\frac{\Delta h}{\Delta x}\right)^2; \quad W_{+1}^x = \frac{1}{8}\left(1 + \frac{2\Delta h}{\Delta x}\right)^2.
\tag{4.16}
$$

Analogous weights are defined along the y and z-dimensions, giving W_m^y and W_n^z.

The weight of the mass in any of the n_{TSC}^3 zones of the smoothing volume surrounding the particle is a product of the weights from the x, y, and z dimensions. After the weights of a sink particle are computed, the particle's mass m_p is applied to the grid. Within each particle's smoothing volume, the particle's effective density at zone (l,m,n) is given by $\frac{W_l^x W_m^y W_n^z m_p}{\Delta x \Delta y \Delta z}$. Outside of the sink's control volume, the density is equal to that of the gas. After the combined gas+particle density is defined, the solution Φ of the Poisson equation is obtained via FFTs (using the FFTW package, see www.fftw.org). For each zone within the sink control volume, the gravitational field f_{lmn} is computed taking differences of the potential. The gravitational force on each sink particle is computed using the same

122

weights as in Equation (4.15):

$$f = \sum_l \sum_m \sum_n W_l^x W_m^y W_m^z f_{\text{lmn}}, \tag{4.17}$$

where l, m and n run from $-(n_{\text{TSC}} - 1)/2$ to $(n_{\text{TSC}} - 1)/2$.

With a TSC smoothing volume of n_{TSC}^3 zones, the effective radius for smoothing by the TSC algorithm is $r_{\text{TSC}} \equiv n_{\text{TSC}} \Delta x / 2$. For $n_{\text{TSC}} = 3, 5$ and 7, r_{TSC} is $1.5\Delta x, 2.5\Delta x$ and $3.5\Delta x$ respectively. With larger r_{TSC}, sink particles' masses are smoothed to a larger volume, and the gravity is softened more. A smaller value of r_{TSC} gives more accurate gravity near a particle. However, the hydrodynamic fluxes are better resolved if the radius r_{ctrl} of the sink control volume (see section 2.2.2) is larger. We have tested different combinations of r_{ctrl} and r_{TSC} with $r_{\text{ctrl}} \geq r_{\text{TSC}}$ for the test problems described in Section 3.1 and 3.2. We find that different r_{ctrl} give nearly the same accretion rate. To maximize resolution, we therefore adopt $n_{\text{TSC}} = 3$ and $r_{\text{ctrl}} = r_{\text{TSC}} = 1.5\Delta x$ as our standard choice.

Sink particles in our algorithm represent unresolved star/disk/envelope structures. Because the gas structure and gravity is not resolved within the control volume of each sink particle, the detailed interaction of star/disk/envelope systems that collide or pass near each other cannot directly be followed. We therefore take a conservative approach and merge two sink particles whenever their control volumes overlap. A new sink particle is created at the center of mass of the two previous sink particles, with total mass and momentum conserved. We note that provided the effective mass distribution of each sink remains spherically-symmetric and concentrated at a very small scale, it would be safe to adopt less-strict merger criteria in methods that compute interparticle forces directly rather than using particle-mesh gravity; in this case close particle-particle interactions require sub-time-stepping (see e.g. Federrath et al. 2010; Krumholz et al. 2004). Because torques on the gas are not well resolved when the sink region has only 3^3 zones, we do not presently track the spin angular momentum of the sink particles.

4.3 Tests of the Method

4.3.1 Particle Orbits

To test the TSC algorithm and the leapfrog integrator, we consider a problem in which two particles with equal mass orbit their common center in circular orbits. The initial circular speed of the two particles is $v = \frac{1}{2}\sqrt{2Gm/d}$, where G is the gravitational constant, m is the mass of each sink particle, and d is the distance between two sink particles. The gravity between sink particles and gas is disabled, so that sink particles only feel gravity from each other. Figure 4.1 shows the trajectory of one particle for 10 orbits for $d/L = 0.2$ (top panels) and $d/L = 0.3$ (bottom panels) with resolutions $32^3, 64^3$ and 128^3 from left to right. Here, L is the simulation box size, corresponding to either 5 or 3.3 times the interparticle separation d (which is the semimajor axis for the reduced-particle Kepler orbit). Vacuum boundary conditions are used for the gravity solver.

As long as the gravity is well resolved, the combination of the TSC scheme and leapfrog integration gives accurate orbits. For $d/L = 0.2$, the radius of the orbit is $3.2\Delta x, 6.4\Delta x$ and $12.8\Delta x$ for resolution $32^3, 64^3$ and 128^3 respectively. For 32^3 resolution with $r_{\text{ctrl}} = 1.5\Delta x$, the cubic smoothing volumes for each particle are separated by only $2 - 3$ zones, such that the gravitational potential is not well approximated by a point mass. For resolution 64^3 and 128^3, this distance ranges $(8 - 10)\Delta x$ and $(21 - 22)\Delta x$ respectively. We find that for 64^3, the orbits are a bit coarse, whereas for 128^3, the orbits are nearly perfect. Correspondingly, for the $d/L = 0.3$ cases, the orbit radius is $4.8\Delta x, 9.6\Delta x$ and $19.2\Delta x$ at resolution $32^3, 64^3$ and 128^3, with circular orbits well represented at the higher resolutions. We conclude that provided the orbit radius is resolved by ≥ 10 zones, quite accurate orbits are obtained, with somewhat lower quality orbits at smaller separations. However, even for orbit radii as small as 3 zones (or ~ 0.03pc for typical simulations of
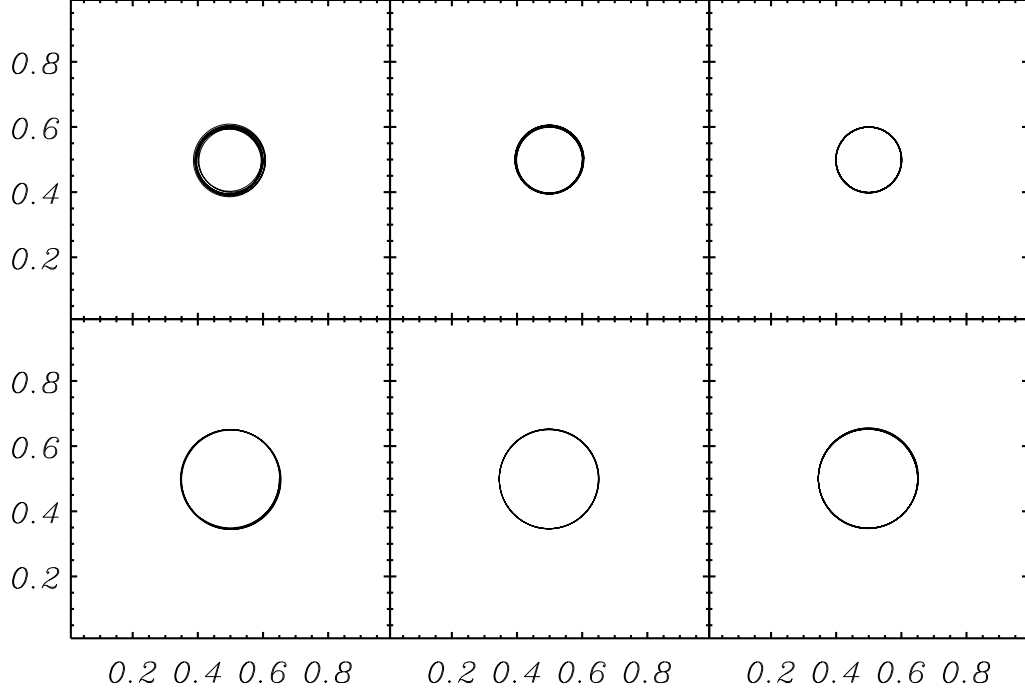
Figure 4.1: Circular orbits of two equal mass sink particles orbiting the center of mass at different distances, testing our leapfrog particle integrator and TSC particle-mesh Poisson solver. The top panels show orbits of diameter $d/L = 0.2$ at box resolutions $(L/\Delta x)^3 = 32^3, 64^3$ and 128^3 zones from left to right. The bottom panels show orbits of diameter $d/L = 0.3$ at the same resolutions. Each panel shows the trajectory of one particle for 10 orbits.

core/star formation in molecular clouds), orbits are approximately circular. By comparison, we note that (Federrath et al. 2011) have found that resolution of a vortex in their hydrodynamic simulations on a Cartesian grid requires a radius of 15 grid cells.

4.3.2 Self-similar Collapse of Isothermal Spheres

To confirm that our algorithms yield the correct accretion rate, we compare our numerical results with analytic solutions. In particular, we compare to the family of self-similar accretions solutions analyzed by Shu (1977). The density profile for a generalized singular isothermal sphere is

$$\rho(r) = \frac{Ac_s^2}{4\pi Gr^2}. \tag{4.18}$$

125

For $A > 2$, equilibrium is not possible because gravity exceeds the gas pressure gradient everywhere; for these initial conditions, a sphere would globally collapse everywhere. The case $A = 2$ with zero velocity everywhere corresponds to an unstable hydrostatic equilibrium. Shu (1977) analyzes a family of self-similar solutions in which the density profile in the outer parts approaches Equation (4.18), while the inner part approaches a free-fall profile with $\rho \propto r^{-3/2}$. The outer part has $v \propto -r^{-1}$, while in the inner part the velocity approaches free-fall $v \propto -r^{-1/2}$. For any value of A, the central accretion rate is constant, such that the central mass $M \propto t$, and we can define a dimensionless accretion rate $\dot{M}/(c_s^3/G)$.

We have tested a series of values of A ranging from 2.0004 to 4, the same as the values in Table 1 of Shu (1977). Krumholz et al. (2004) show (their Fig 1) a comparison of the numerically-computed density and velocity profiles to the semi-analytic collapse solution of Shu (1977) for the singular isothermal sphere; Federrath et al. (2010) show (their Fig. 10) the density and velocity profiles of their numerical solution at several times for the case A=29.3. The initial density and velocity profiles are the solution of Equations (11)-(12) in Shu (1977), obtained using a four-step Runge-Kutta integration scheme. For code units, we adopt an arbitrary density ρ_0, together with length scale, $L_J = c_s(\pi/G\rho_0)^{1/2}$ and time scale $t_J = L_J/c_s$. For all of the tests in this section, the simulation domain size is $(4L_J)^3$, and the resolution is 129^3. Vacuum boundaries are used for the gravity solver.

The initial radial density and velocity profiles are truncated at $r_{\max} = 1.5L_J$. Outside this radius, the initial density is set to $\rho(r = 1.5L_J)$, and the initial velocity is set to zero. To convert the self-similar solutions to initial density and velocity profiles input to the simulation, we choose an initial time $t/t_J = 0.43$ such that in the case $A = 2.0004$, the initial radius of the expansion wave is 11% of the box size and 29% of the initial radius of the sphere. In the case $A = 2.0004$, the total mass of the sphere within $r = 1.5L_J$ is $18.9c_s^3(4\pi G^3\rho_0)^{-1/2}$. A sink particle is introduced at the center of the sphere at the
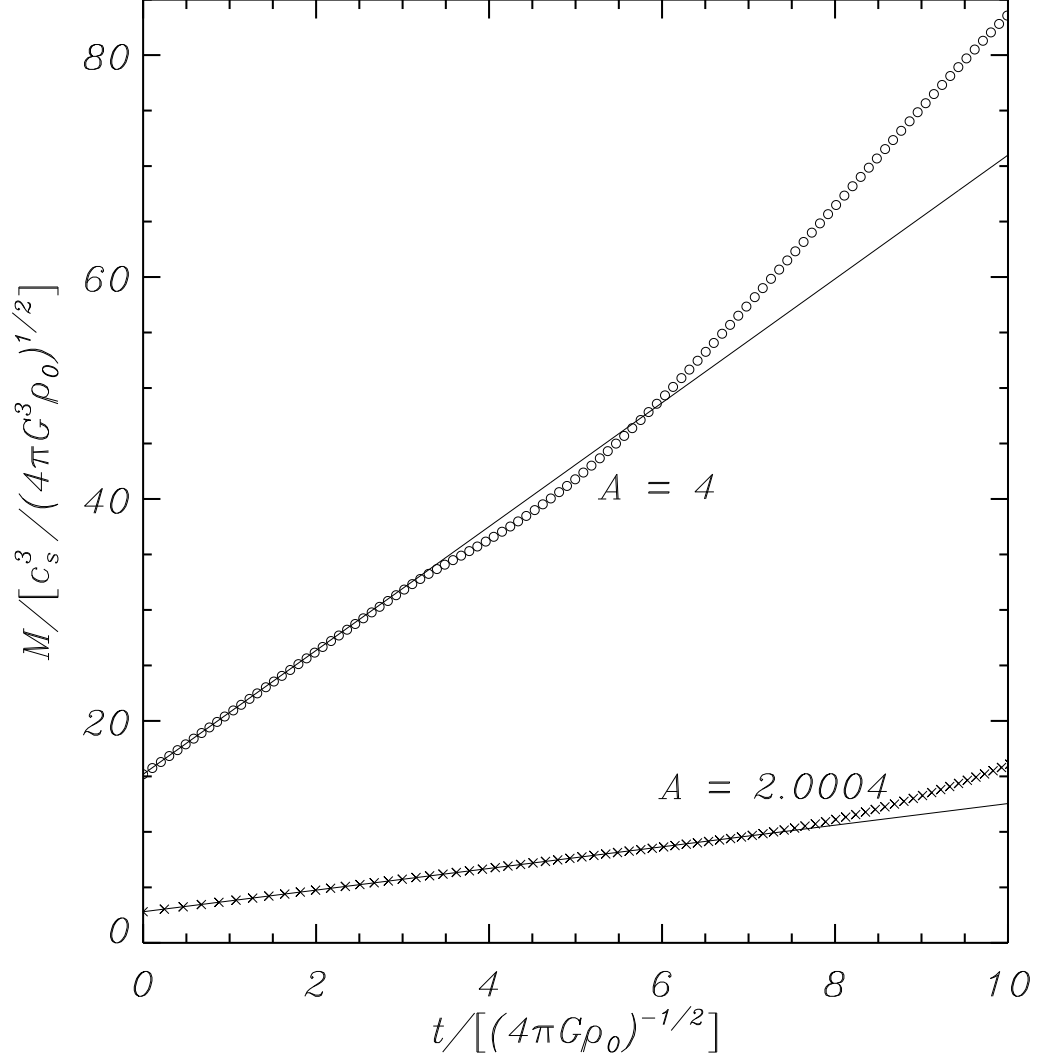
Figure 4.2: Accretion history of the central sink particle for comparison with the case $A = 2.0004$ (crosses) and 4 (open circles) from Shu (1977). The analytic accretion solutions for self-similar flows are shown by the solid lines. The accretion rates from our simulations are consistent with the analytical solutions during early stages. The enhancement of accretion rates in the later stages is due to the collapse of the outer part of the initial sphere, which is affected by boundary conditions. In the units given, the initial sphere masses for the cases $A = 2.0004$ and $A = 4$ are 18.9 and 40.7, respectively. We fit the linear part of this and other accretion histories to derive the accretion rates plotted in Figure 4.3.

beginning of the simulation, with its initial mass set to the mass of the initial profile within $r = r_{\mathrm{ctrl}}$ (Equations (8), (10) in Shu (1977)). Note that the uniform density outside the sphere leads to "outside-in" collapse because of the imbalance of gravity and gas pressure

at the truncation radius. This process will not affect the initial "inside-out" accretion to the central sink particle, however.

Figure 4.2 shows the accretion history of the central sink particle for the cases $A = 2.0004$ (crosses) and 4 (open circles). The solid lines are the analytic solutions from Shu (1977). Before effects from the outer boundary conditions begin to affect the accreting region, the simulation evidently reproduces the analytical solutions extremely well. For the case $A = 2.0004$, the particle mass at $t = 6(4\pi G\rho_0)^{-1/2}$, near the end of the linear stage, has reached 46% the sphere's initial mass, increasing by a factor three from its initial value. For each value of A, we compute the accretion rate in the simulation using a fit to the sink particle's mass versus time during the stage when this evolution is linear.
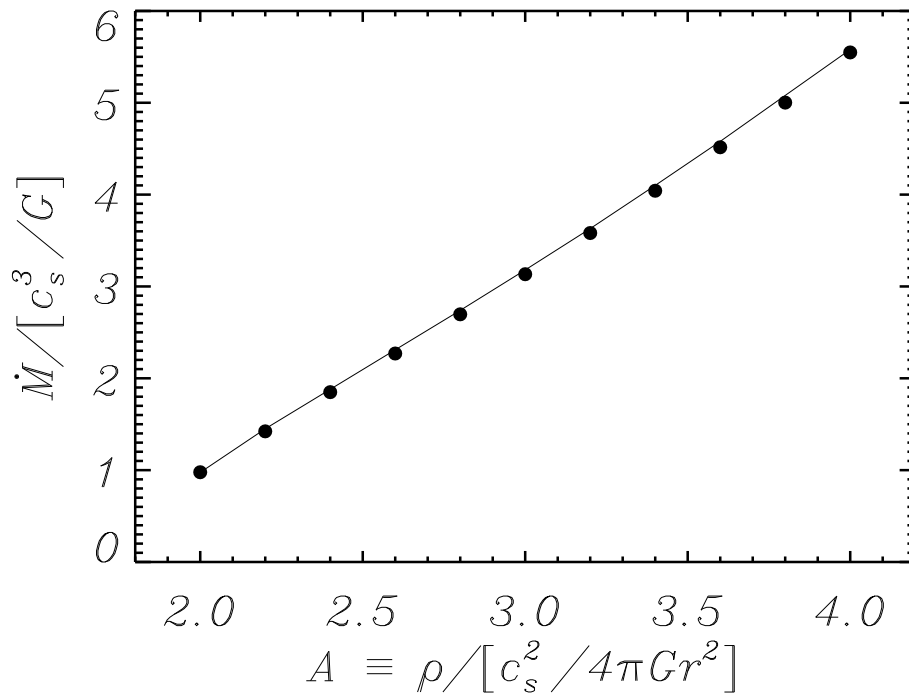
Figure 4.3: Accretion rates for self-similar collapse of isothermal spheres with different overdensity coefficients, A (see Equation (4.18)). The solid line shows the analytical accretion rates derived by Shu (1977), via direct integration of isothermal fluid equations for self-similar models. The solid dots are from accretion rates measured in our 3D simulations.

Figure 4.3 shows the accretion rates for models based on Shu's solutions with different values of A. The line shows the values from the analytic solution of Shu (1977), and

the solid black dots are based on measurements from our numerical simulations. The 3D simulations reproduce nearly exactly the predicted accretion rate from the analytic solutions.
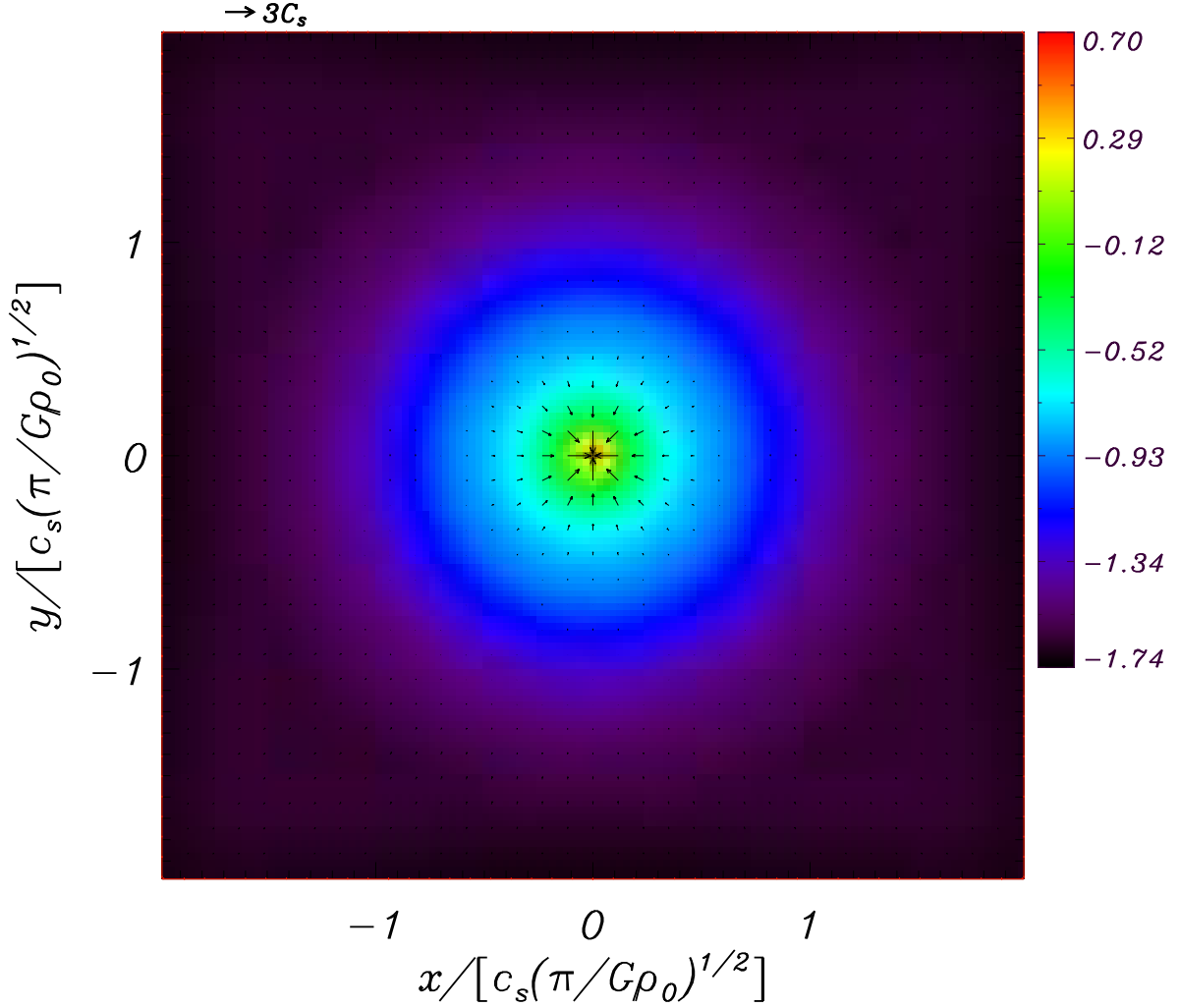
Figure 4.4: Density and velocity field cross-section snapshot for the collapsing near-singular isothermal sphere ($A = 2.0004$). The color scale represents an $x-y$ slice through the density ($\log\rho$). The direction and length of arrows indicate the direction and magnitude of the local velocity, with scale as indicated in the upper left. The "expansion wave" is evident in the plot, with collapse in the inside ($r < 0.67L_J$) and a near-static solution in the outside ($r > 0.67L_J$). The location of the expansion wave for the initial conditions was $r = 0.43L_J$.

Figure 4.4 shows a sample cross-section of the density and velocity field near the center of the collapsing singular sphere for $A = 2.0004$. Since A is close to 2, the sim-
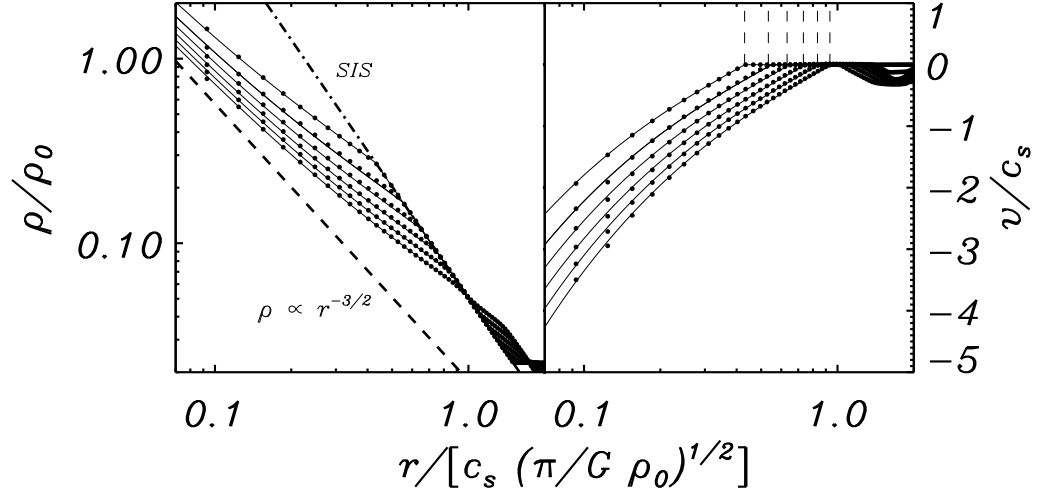
Figure 4.5: Radial profiles of density (left panel, filled circles) and velocity (right panel, filled circles) for evolution of near-singular ($A = 2.0004$) isothermal sphere. The time interval between profiles is constant, equal to $0.1(\pi/G\rho_0)^{1/2}$, with successive profiles moving to lower density and velocity over time. In both panels, the solid lines are the analytic solutions obtained by integrating Equations (11)-(12) in Shu (1977). For the Shu (1977) expansion wave solution, the outer part of each profile is static (the equilibrium singular isothermal sphere), and the inner part of each profile approaches free fall, with $\rho \propto r^{-3/2}$ and $v \propto r^{-1/2}$. The dot dash line in the left panel shows the singular isothermal sphere density profile. The velocity profiles are plotted in linear-log scale to show the propagation of the "expansion wave". The dashed lines in the right panel indicate the position of the "expansion wave" front. The consistency of our numerical solution with the Shu (1977) solution is evident.

ulated sphere recovers Shu's famous "expansion-wave" solution: the outer part retains a static singular isothermal equilibrium profile before the expansion wave arrives, and the inner part is free-falling towards the center. Figure 4.5 shows the radial density profiles and velocity profiles from the simulation at different instants during the collapse. The filled circles are the profiles from the numerical simulation and the solid lines are the corresponding analytic solutions. Our simulation reproduces the analytic solutions. The "expansion wave" is clearly seen from both the density and velocity profiles. In both density and velocity profiles, it is seen that gas very near the boundaries collapses, and the outer density is slightly altered from $\rho \propto r^{-2}$. This behavior is due to conditions near the boundaries, but this process does not affect the collapse in the interior.

4.3.3   Galilean Invariance of Accretion

To confirm that the accretion is properly computed for moving particles, we consider tests in which both the particle and surrounding gas are initialized with a bulk flow across the grid. The initial conditions of these models are exactly same as the $A = 2.0004$ case in Section 3.2, but with an additional uniform bulk flow of speed $v_{ad} = 0, 0.5c_s, 1.5c_s$ and $2.5c_s$. If the update of the mass and momentum of the sink particle is correct, it will continue to move with the surrounding gas sphere at the same velocity. The mass accretion rate onto the sink particle should also be the same for different bulk flow speeds. For this problem, periodic boundaries are adopted for both gas and the gravity solver. For all of the tests in this section, the simulation size is $(4L_J)^3$, and the resolution is 129^3.

We note that the boundary conditions in Section 3.2 are open, different from what we adopt in this section. Here, we adopt periodic boundary conditions so that the sphere may pass through the boundary of the simulation domain (for large Mach number cases). Because of the difference in boundary conditions, the accretion rate is different from that in Section 3.2; however we shall show that the accretion rates are all consistent with each other for different Mach numbers.

Figure 4.6 shows the speed and mass of the sink particle versus time, for all tests. For the case of zero bulk advection, the speed of the particle remains zero all the time. For $v_{ad} \neq 0$, the mean speed of the sink particle agrees with the bulk speed, with small oscillations. During an interval $\Delta x/v_{ad}$, the time for the sink particle to cross a zone, the control volume does not move. However, as discussed in Section 2.2.2, the sink control volume must be reset when the particle crosses a zone boundary. During the time interval $\Delta x/v_{ad}$, the mass and momentum fluxes into the control volume are not exactly symmetric, because the gravitational potential is not symmetric if the particle is offset from its zone center. The downwind material enters the control volume with relatively larger mo-

mentum than the upwind material, and addition of net positive momentum accelerates the sink particle. The speed of the sink particle therefore temporarily increases. As the particle crosses the border of one cell to enter the next cell, the sink control volume is shifted, and mass and momentum differences from cells entering and leaving the control volume are applied to the particle to conserve mass and momentum. As a consequence, the particle's speed is reduced immediately after crossing a cell edge. At late times, the fractional change in the momentum becomes small, so the oscillation amplitude drops.
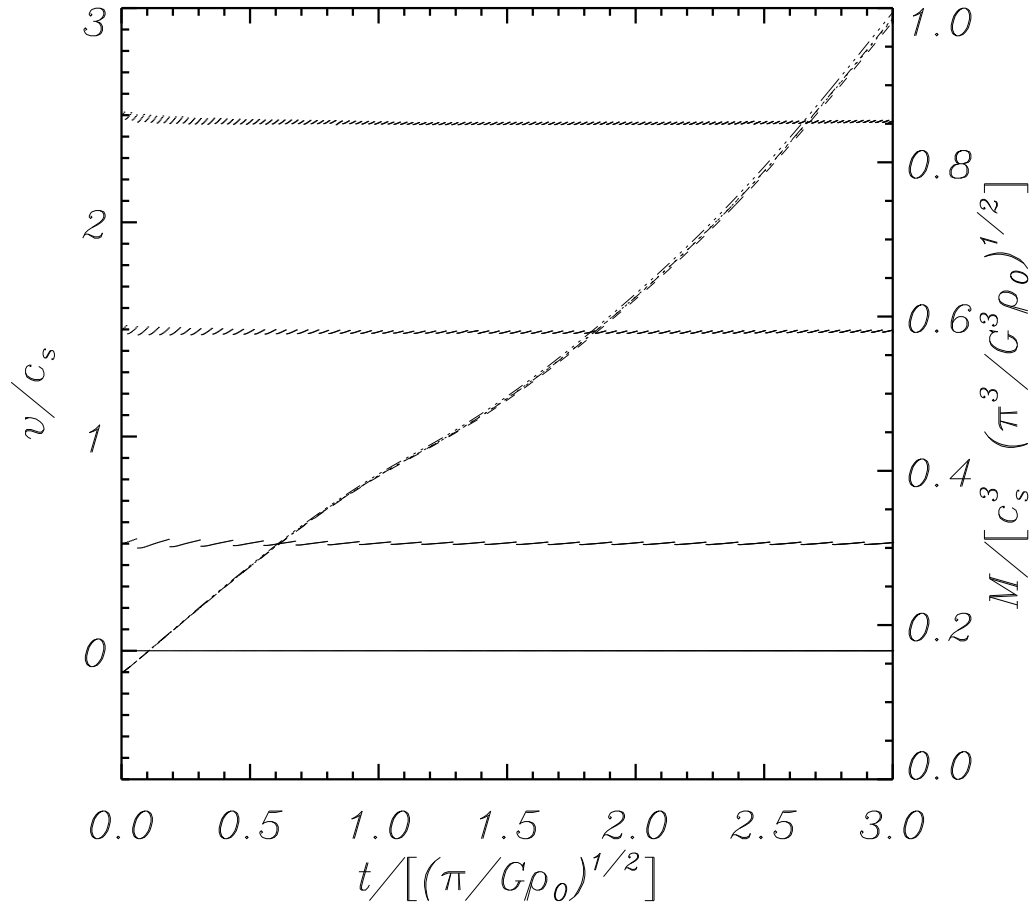
Figure 4.6: Tests of accretion onto a sink particle for the collapsing near-singular isothermal sphere ($A = 2.0004$) with bulk motion across the grid, demonstrating Galilean invariance. Horizontal curves, left scale: the temporal evolution of the speed of the sink particle for different cases. From bottom to top, the bulk advection speed is $0, 0.5c_s$, $1.5c_s$ and $2.5c_s$. The time-averaged particle speeds remain constant, and equal to that of the bulk flow. Diagonal curves, right scale: the temporal evolution of the mass of the central sink particle for the four different cases. The accretion rate is same for static, subsonic, and supersonic advection cases, confirming Galilean invariance of our algorithms.

132

Figure 4.6 shows that the mass of the sink particle increases at the same rate for all the tests, at varying v_{ad}. At early stages, before material originating near the sphere's boundaries accretes to the sink particle, differences in the accretion rate are completely negligible, and and differences remain very small even after material originating near the boundaries reaches the center.

We conclude that our sink particle algorithm satisfies Galilean invariance, with the accretion rate the same whether or not the flow and the grid are in relative motion.

4.3.4   Collapse of a Bonnor-Ebert Sphere

To test our algorithm for the the creation of a sink particle, together with the accretion after formation, we run 3D simulations of the evolution of a Bonnor-Ebert sphere (Bonnor 1956; Ebert 1955, hereafter BE) and compare the results to a 1D spherically-symmetric simulation conducted with another code. We consider a BE sphere with a radius slightly larger than the critical radius, $r = 1.1 r_{BE,crit}$ for $r_{BE,crit} = 0.274 c_s / (\pi / G \rho_e)^{1/2}$, where ρ_e is the edge density. The density inside the sphere is everywhere twice as large as the equilibrium value. Exterior the sphere, the density is set to $0.001 \rho_e$. The initial velocity is everywhere set to zero for the initial conditions. The gas boundary conditions are outflow. The resolution is 129^3, and the box size is $[0.301 c_s / (\pi / G \rho_e)^{1/2}]^3$.

Figure 4.7 shows the cross-section of the density and velocity field across the center of the BE sphere immediately before the central sink particle is created. Evidently, the inner part collapses inwards, following the "outside-in" collapse described by Larson (1969). Because the outer boundary of the sphere is not in equilibrium (for this isothermal simulation, we do not have a hot confining medium), the outer part of the sphere expands outwards at the same time. Only the very late accretion to the sink particle is affected by the early expansion of the outer parts of the sphere.

Figure 4.8 shows the accretion rate and the mass of the sink particle from our 3D
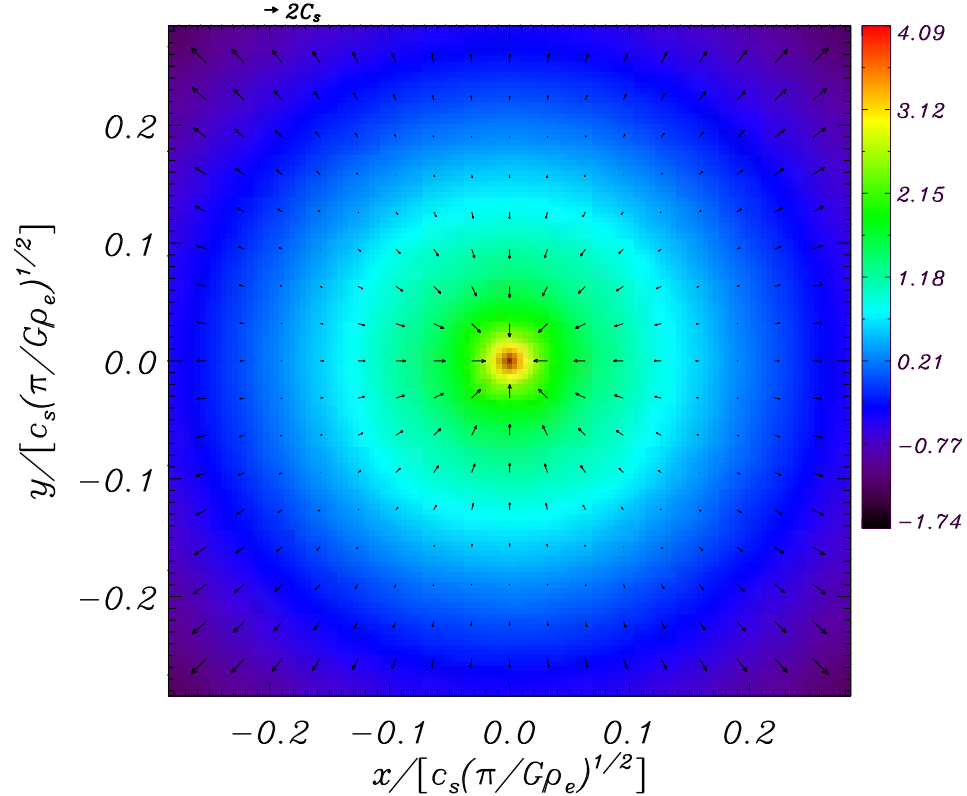
Figure 4.7: Density and velocity field cross-section at the instant of singularity for collapse of a Bonnor-Ebert sphere. The color scale represents an $x - y$ slice through the volume density ($\log \rho / \rho_e$, for ρ_e the initial density at the outer edge of the sphere). The direction and length of arrows indicate the direction and magnitude of the local velocity, with scale as indicated in the upper left. The inner part of the sphere is collapsing, with velocity increasing inward to approach $-3.4c_s$. Because we do not have a hot, high-pressure confining medium, the outer part of the sphere also expands.

simulation, in comparison with the 1D simulation of Gong & Ostriker (2009) obtained with the *ZEUS* code. The solid lines are from the 3D simulation and the dashed lines are from the 1D simulation. The accretion rates immediately after the creation of the particle differ, but the accretion rates at later stages are almost exactly the same. The peak accretion rate is higher for 1D than 3D because it is measured closer to the sink particle (0.5 zones vs. 1.5 zones). In addition, the point of singularity formation cannot be resolved as well on a 3D Cartesian grid as 1D spherically-symmetric grid. However, it is evident that the 3D code captures the overall accretion history very well.

To further check the results of the model evolution, Figure 4.9 compares the density
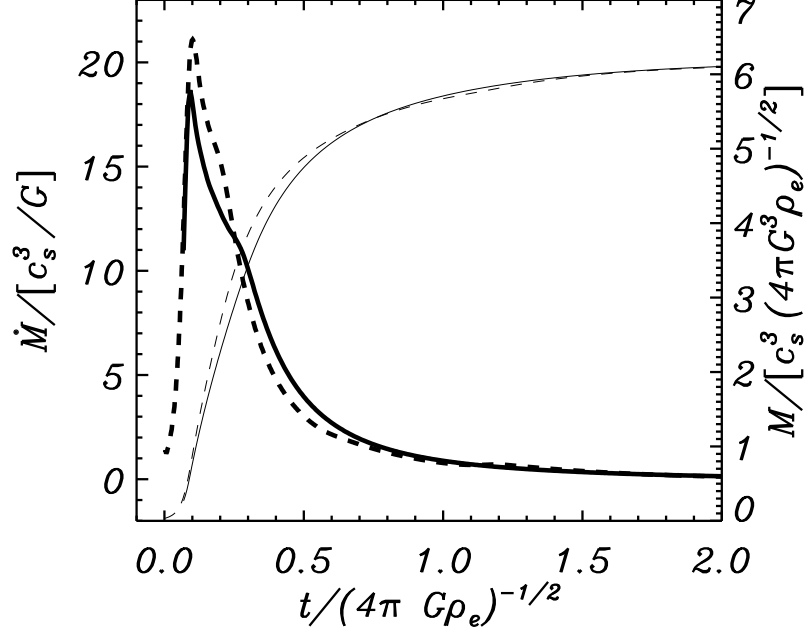
Figure 4.8: Comparison of accretion for 3D Cartesian simulation with 1D spherically-symmetric simulation, for evolution of Bonnor-Ebert sphere. Thick curves, left scale: the temporal evolution of the mass accretion rate at the inner edge of the grid. Thin curves, right scale: evolution of the central point mass. The solid curves are for the 3D simulation with *Athena* and the dashed curve is for the 1D simulation with *ZEUS*.

and velocity profiles for 3D and 1D simulations at the instant of the sink particle creation. The density profiles both approach the Larson-Penston singular solution (Equation (4.7)), while the velocity profiles approach the limit $v = -3.4c_s$, in the inner part.

Figure 4.10 shows the radial density and velocity evolution for the 3D simulation for this test. The solid lines show the profiles before the sink particle is created, the dashed lines show the profiles at the instant of the sink particle creation, and the dotted lines show the profiles during the envelope infall stage (see Gong & Ostriker 2009). Profiles are separated by time $\Delta t = 0.043(\pi/G\rho_e)^{1/2}$. The collapse of the inner part (and the expansion of the outer part) is clearly seen. The density approaches the singular LP profile $\rho \propto r^{-2}$ (Equation (4.7)) at the instant of collapse, and the corresponding velocity profile is flat in the inner part, approaching $-3.4c_s$. After the creation of the sink particle, the inner density and velocity profiles approach free-fall.
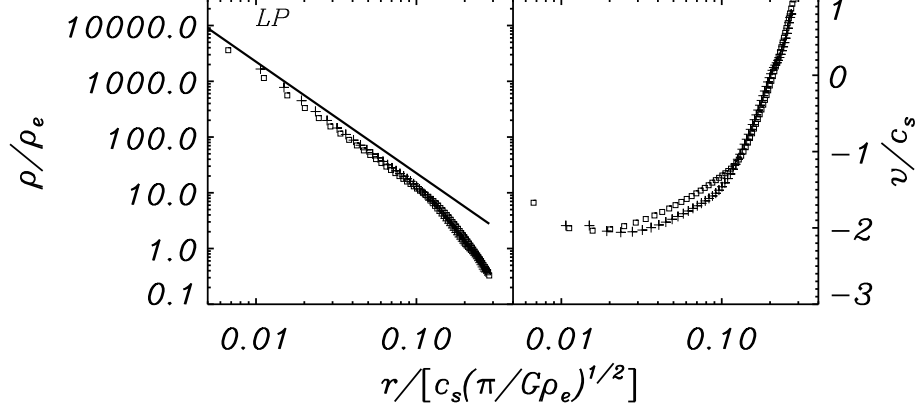
Figure 4.9: Density (left) and radial velocity (right) profile comparison between 3D *Athena* simulation and 1D spherically-symmetric *ZEUS* simulation for the instant of singularity in Larson-Penston collapse. The pluses are for the 1D simulation and the squares are for the 3D simulation. Also shown is the singular LP density profile (Equation (4.7); solid line on left). Units are normalized using the initial density at the edge of the sphere, ρ_e. The initial outer radius of the sphere is $1.1r_{\text{BE,crit}}$, and the initial density in the region exterior to the sphere is $0.001\rho_e$.

4.3.5 Converging Supersonic Flows

Gong & Ostriker (2009) presented a unified model for dense molecular core formation and evolution, based on spherically-symmetric simulations. In that work, dense cores are not present as either stable or unstable density concentration in the initial conditions, but are built by the convergence of supersonic flows. Post-shock compressed gas accumulates over time in stagnant, shock-bounded regions. When the core accumulates enough mass, it becomes gravitationally supercritical and collapses, leading to formation of a protostar at the center. This is followed by a stage of infall of the envelope onto the protostar, and subsequent accretion of ambient material.

To ensure the accretion rate of sink particles is accurate for cores formed by supersonic flows, we run a simulation of a 3D spherical converging supersonic flow, and compare to the accretion rate obtained by Gong & Ostriker (2009) using a 1D spherically-symmetric simulation. The initial density is uniform everywhere, with a value ρ_0 (this represents a typical density within GMCs). The flow in the initial conditions converges to the center

136
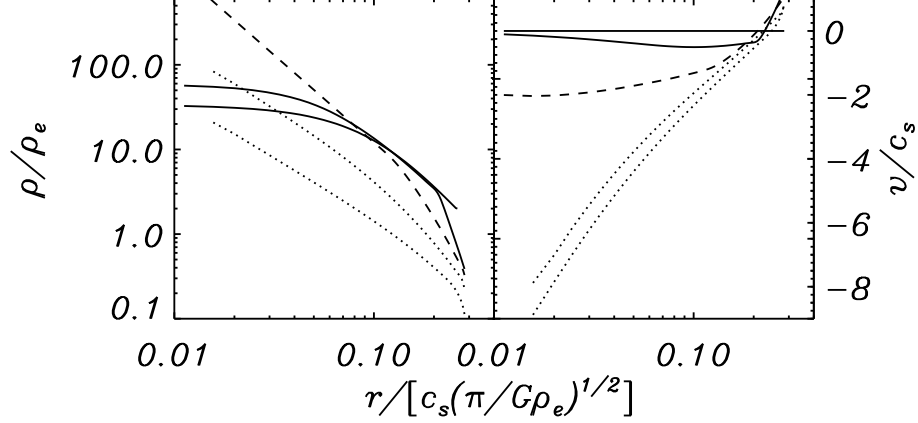
Figure 4.10: Radial density (left) and velocity (right) profiles throughout collapse and infall stages for test beginning with static Bonnor-Ebert density profile. The solid lines are during collapse ($t = 0$ for the lower and $t = 0.043t_0$ for the upper curve in the left panel, and the opposite in the right panel), the dashed lines are at the instant of sink particle creation, and the dotted lines are during the infall stage ($t = 0.129t_0$ for the upper and $t = 0.172t_0$ for the lower curve in each panel). The time unit is $t_0 = c_s(\pi/G\rho_e)^{1/2}$ for ρ_e the initial density at the edge of the sphere. The behavior in each stage is consistent with previous results from spherically-symmetric simulations (Gong & Ostriker 2009). The time interval between profiles is $\Delta t = 0.043t_0$.

everywhere at Mach 2. The size of the simulation box is $1.6c_s/(4\pi G\rho_0)^{1/2}$. This size is chosen so that it is large enough for the post-shock compressed region to grow until it collapses. The simulation is run with 129^3 cells. For the 1D spherical symmetric simulation, the initial density and velocity profiles are the same as 3D but the model is run with 64 zones. For the 1D simulation, a sink cell is introduced at the center after collapse occurs, with an outflow boundary condition next to the sink cell (Gong & Ostriker 2009).

Figure 4.11 shows the accretion rate and the mass of the protostar versus time during the envelope infall stage, comparing the 3D and 1D simulation results. The accretion rate is nearly same for the two cases, and the mass history of the "protostar" is comparable. For the 1D simulation, the accretion rate will decrease to exactly the inflow value $8\pi G\rho_0 r_{\text{box}}$ at late time. For 3D simulation, however, we cannot create an ideal spherical converging flow given our cubic domain, such that the accretion rate decreases after $t \sim 0.2(4\pi G\rho_0)^{-1/2}$. Note that the peak of the accretion rate for the 1D model is smaller
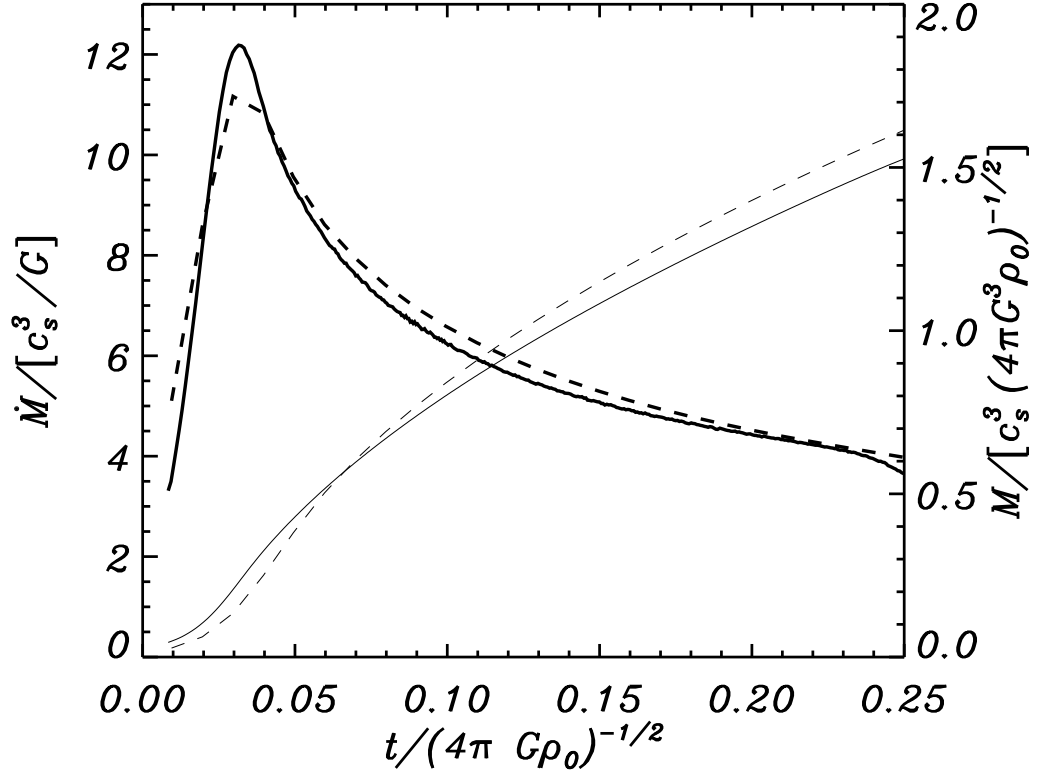
Figure 4.11: Comparison of accretion evolution for 3D Cartesian and for 1D spherically-symmetric simulation for spherical converging supersonic (Mach 2) flow. Heavy curves show accretion rate, and light curves show sink particle mass. Solid curves are the 3D model with *Athena*, and dashed curves are the 1D model with *ZEUS*.

than the value in Gong & Ostriker (2009) for Mach 2, due to lower resolution here.

4.4 Planar Converging Supersonic Flow with Sink Particles

The most generic configuration for converging supersonic flow is planar, and Gong & Ostriker (2011) presented a set of 3D numerical simulations with this geometry – combined with turbulent perturbations – to study the core building and collapse. The models of Gong & Ostriker (2011) represent a localized region within a giant molecular cloud, in which there is an overall convergence in the velocity field (produced by the largest-scale motions in the cloud), combined with a turbulent power spectrum in which linewidth in-

creases with size. Since sink particle techniques were not employed in Gong & Ostriker (2011), each model simulation was stopped when the most evolved core collapsed. To demonstrate the capabilities for following multiple core collapse and evolution when sink particles are introduced, here we rerun a sample simulation from the Gong & Ostriker (2011) suite.

As in Gong & Ostriker (2011), we adopt the isothermal approximation. The isothermal sound speed at a temperature T is

$$c_s = 0.20 \text{ km s}^{-1} \left(\frac{T}{10 \text{ K}} \right)^{1/2}. \tag{4.19}$$

If the density within clouds were uniform, the spatial scale relevant for gravitational instability would be the Jeans length

$$L_J \equiv c_s \left(\frac{\pi}{G\rho_0} \right)^{1/2} = 2.76 \text{ pc} \left(\frac{n_{\text{H},0}}{10^2 \text{ cm}^{-3}} \right)^{-1/2} \left(\frac{T}{10 \text{ K}} \right)^{1/2}, \tag{4.20}$$

evaluated at the mean density ρ_0. The corresponding Jeans mass is

$$M_J \equiv \rho_0 L_J^3 = c_s^3 \left(\frac{\pi^3}{G^3 \rho_0} \right)^{1/2} = 72 \text{ M}_\odot \left(\frac{n_{\text{H},0}}{10^2 \text{ cm}^{-3}} \right)^{-1/2} \left(\frac{T}{10 \text{ K}} \right)^{3/2}. \tag{4.21}$$

The Jeans time at the mean cloud density is

$$t_J \equiv \frac{L_J}{c_s} = \left(\frac{\pi}{G\rho_0} \right)^{1/2} = 3.27 \, t_{\text{ff}}(\rho_0) = 1.4 \times 10^7 \text{ yr} \left(\frac{n_{\text{H},0}}{10^2 \text{ cm}^{-3}} \right)^{-1/2}. \tag{4.22}$$

Since we consider a planar converging flow, another relevant quantity is the total surface density integrated along the z direction,

$$\Sigma = \int \rho(x,y,z) dz = \Sigma_0 \int \frac{\rho}{\rho_0} \frac{dz}{L_J}, \tag{4.23}$$

for $\Sigma_0 \equiv \rho_0 L_J = 9.49 \text{ M}_\odot \text{ pc}^{-2} (T/10K)^{1/2} (n_{\text{H},0}/10^2 \text{ cm}^{-3})^{1/2}$.

For this test, the supersonic flow converges to the central plane from $+z$ and $-z$ directions at Mach number $\mathcal{M} = 5$, for total relative Mach number 10. For both the whole

domain initially and the inflowing gas subsequently, we apply perturbations following a Gaussian random distribution, with a Fourier power spectrum of the form

$$\langle |\delta v_k|^2 \rangle \propto k^{-2}, \tag{4.24}$$

for $|kL/2\pi| < N/2$, where N is the resolution and L is the size of the simulation box in x and y. The power spectrum is appropriate for supersonic turbulence as observed in GMCs (McKee & Ostriker 2007). The perturbation velocity fields are pre-generated with resolution 256^3 in a box of size L_J^3. The perturbation fields are advected inward from the z-boundaries at inflow speed $\mathcal{M} c_s$: at time intervals $\Delta t = \Delta z / (\mathcal{M} c_s)$, slices of the pre-generated perturbation fields for v_x, v_y and v_z are read in to update values in the ghost zones at the z-boundaries.

We set the amplitude of the turbulent power spectrum at the large scale to $\delta v_{1D}(L_J) = 1.3 c_s$, which corresponds to the low amplitude case in Gong & Ostriker (2011). The resolution is $N_x \times N_y \times N_z = 256 \times 256 \times 96$, with domain size $L_x \times L_y \times L_z / L_J^3 = 1 \times 1 \times 0.375$.

4.4.1 Structure Evolution

Figure 4.12 shows evolution of the surface density (Equation (4.23)) projected in the z-direction after the most evolved core collapses and creates a sink particle (marked as "1" in the images). The instants for the four images from top left to the bottom rights are: $0.301t_J$, $0.349t_J$, $0.398t_J$ and $0.446t_J$. The time interval between these images is

$$\Delta t = 0.048t_J = 6.72 \times 10^5 \ \text{yr} \left(\frac{n_{H,0}}{10^2 \, \text{cm}^{-3}} \right)^{-1/2}. \tag{4.25}$$

The black dots and numbers mark the sink particles formed prior to the time of each snapshot for the first three plots. In the last frame, the magenta curves show the trajectories of sink particles and the black triangles show where these sinks were created. Over time, some of the sinks merge, and the large white solid dots show the final set of post-merger

sink locations at $t = 0.446t_0$. The numbers marking sinks in the images indicates the sequence of their creation. In the top right figure, the sink number 7 is missing since it has merged with the sink 1. Similarly, in the lower left, several of the sinks have already undergone mergers, and their corresponding numbers are not shown (5, 6, 7, 10, 11).
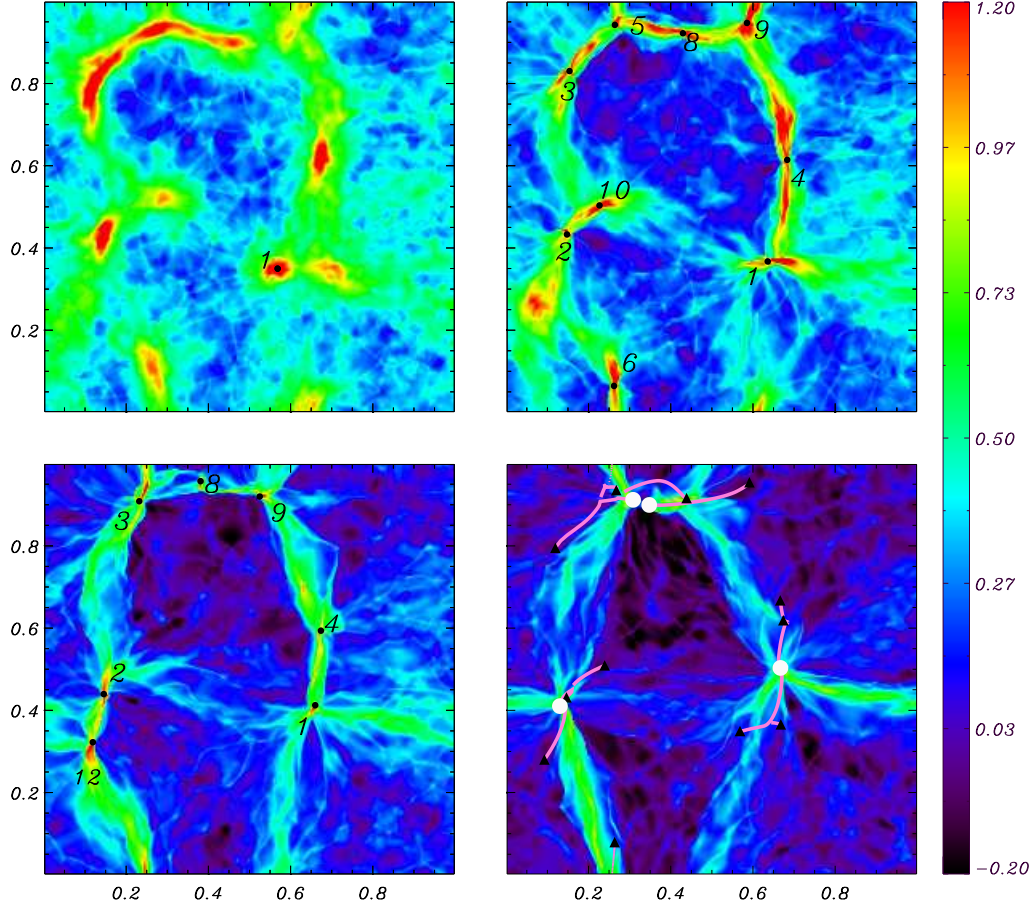
Figure 4.12: Evolution of surface density projected in the z-direction (color scale $\log\Sigma/\Sigma_0$) for a planar converging flow simulation with inflow Mach number $\mathcal{M} = 5$, and supersonic turbulence. The four panels from top left to bottom right show snapshots at four instants: $0.301t_J$, $0.349t_J$, $0.398t_J$, and $0.446t_J$. The top left panel shows the surface density when the first sink "1" is created. The numbers in panels mark the time sequence of sink formation. The black solid dots in the first three frames show instantaneous locations of sink particles. In the final panel, the four white large solid dots show the surviving sinks after mergers. The magenta curves shows the trajectories of all sinks from birth (marked with triangles) to the end of the simulation. The area of the projected domain is $L_J \times L_J$ (see Equation (4.20)).

Filamentary features dominate the moderate–density structure in all images. These

structures grow from the initial turbulent perturbations, which are then amplified by self-gravity (see Fig.1 in Gong & Ostriker (2011)). The localized collapse of these filamentary structures leads to the formation of protostars. Filaments also become more stratified over time as they acquire more material and contract perpendicularly under their self-gravity.

The bottom right panel in Figure 4.12 shows the trajectories of all sinks, as well as their merging history. There were 12 sinks created during this simulation, and four survive at final time. All of the other 8 have merged with other nearby sinks due to close encounters.

4.4.2 Sink Particle Mass Evolution

Figure 4.13 shows the mass of sinks versus time. The solid lines show the four sinks that survive up until late stages. The dotted lines are sinks that undergo mergers with other more massive sinks. Each sink forms at the center of a dense core, and the solid dots show the gravitationally bound core masses calculated using the GRID-core finding algorithm (Gong & Ostriker 2011) immediately before the formation of the corresponding sink particle. The mass of every sink particle grows smoothly to reach and exceed the bound core mass, and keeps increasing until it merges with other sinks. As indicated in the figure, the final masses of sink particles are all much larger than the bound core masses at the initial instant of sink formation, which are in the range $m_{\text{core}} = 0.02 - 0.1 M_J$.

The formation of sinks is divided into three groups. Protostars 1, 2, 3, 4 and 5 form at the earliest time; sinks 6, 7, 8, 9 and 10 form a bit later; and sinks 11 and 12 form during the late accretion stage. Sinks forming at earlier stages are more likely to survive to the end, and their masses grow significantly via mergers and late accretion. For example, the merging history for protostar 1 is: $7 \rightarrow 1 \leftarrow 4 \leftarrow 11$, the merging history for protostar 2 is: $10 \rightarrow 2 \leftarrow 12$, and the merging history for protostar 3 is: $6 \rightarrow 5 \rightarrow 3 \leftarrow 8$.

At late stages, the masses of these surviving sink particles are very high: $M_1 =$
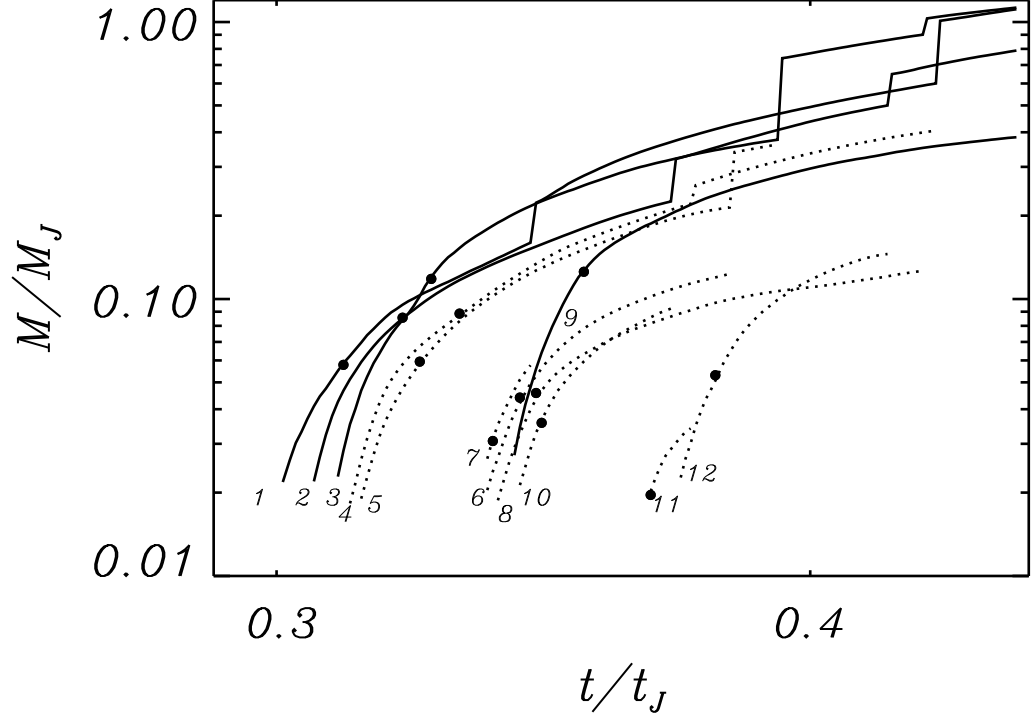
Figure 4.13: Temporal evolution of sink particle masses (see Equation (4.21) and Equation (4.22) for definition of M_J and t_J respectively). The solid black lines show the sinks that survive to late times. The dotted lines show the sinks that are eventually merged into larger particles. The solid black dots show the gravitationally bound dense core masses immediately before the creation of the corresponding sink particle at its center.

$1.11M_J$, $M_2 = 0.79M_J$, $M_3 = 1.13M_J$ and $M_9 = 0.38M_J$. These correspond to tens of $M_\odot$ if $n_{H,0} = 10^2 - 10^3 \, \mathrm{cm}^{-3}$. In part, these sinks may end up with very high mass because the turbulence has low amplitude and is purely decaying. As consequence, matter is not prevented from accreting into the potential wells that develop. In reality, outflows, radiative feedback, and other energy injection would limit gas accretion onto protostars. In addition, some stars could be ejected due to close gravitational encounters, before acquiring a high mass. These physical issues will be addressed in a future publication; it is straightforward to implement localized feedback with rates set by the mass, age, accretion rate, etc, of each sink. Here, our goal is simply to test the proper implementation of sink particle algorithms and to demonstrate that these enable robust long-term evolution.

We note that for the present algorithm (and similarly for other sink particle imple-

143

mentations), the minimum particle mass depends on the grid resolution, on the minimum density threshold for sink creation, and on the size of the sink particle control volume. The sink particle density threshold we adopt here is $\rho_{th} = \rho_{LP}(0.5\Delta x) = 8.86c_s^2/(\pi G(\Delta x)^2)$. With resolution $\Delta x = L_J/N$, $\rho_{th} = 8.86\rho_0(N/\pi)^2$, and the mass within the central cell of the sink region is $0.89M_J/N = N^{-1}65 \ M_\odot (n_{H,0}/10^2)^{-1/2}(T/10K)^{3/2}$. The total initial sink particle mass are larger, due to non-negligible density in the surrounding sink cells. We find (see Figure 4.13) that the initial sink masses in this test simulation are in the range $0.02M_J - 0.1M_J$. With $N = 256$, this ranges from $\sim 6 - 30$ times the minimum mass.

4.4.3 Criteria for Sink Particle Creation

As discussed in Section 2.2.1, different density thresholds have been adopted for sink particle creation by different groups, motivated by different physical and computational considerations. Figure 4.14 shows a comparison of sink particle mass versus time for different sink particle creation criteria. The solid lines are based on criteria of exceeding the LP density threshold (Equation (4.8)) and satisfying the local potential minimum check. The tracks marked by pluses adopt additional criteria: the converging flow check and gravitationally bound state check. The dotted lines adopt the Truelove density instead of the (higher) LP density as a threshold, and apply a check for a local gravitational potential minimum. We find no differences between the sink masses for the first two sets of criteria. For the third set of criteria, the sink masses at birth are much lower than in the first case, because of the lower density threshold. Compared to initial sink masses of $\sim 0.02M_J$ using the LP density criterion, initial sink masses are $\sim 0.005M_J$ using the Truelove density criterion. However, these sinks evolve to follow tracks identical to those found with the other two sink criteria choices. Analogous comparisons at different Mach numbers show that no additional particles are created by artificial fragmentation when using our standard criteria, even though the LP density threshold is higher than the Truelove
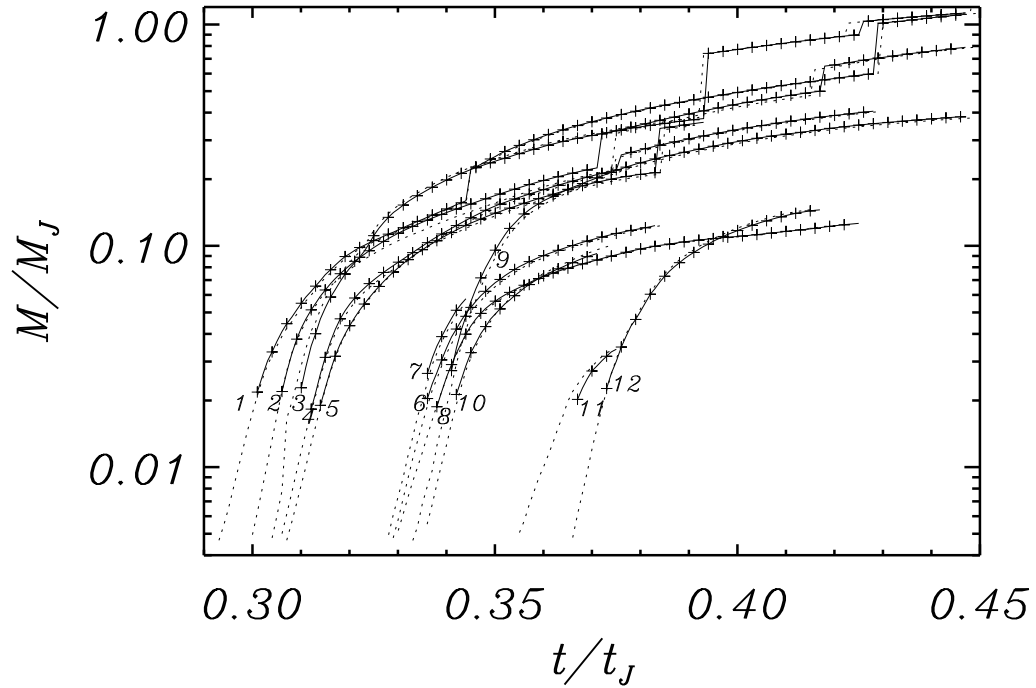
density threshold.

Figure 4.14: Temporal evolution of sink particle masses based on adoption of different creation criteria. The solid lines are for sink particles created with the LP density threshold, and local potential minimum criteria. The tracks marked by pluses are for sink particles created based on additional criteria: a converging flow and a gravitationally bound state. The dotted lines are for sink particles created based on the Truelove density threshold and the local gravitational potential minimum check.

We conclude that a proper density threshold and local potential minimum check are probably sufficient criteria for sink particle creation. By choosing a density threshold given by the LP solution, and requiring that the zone is at a local potential minimum, we can ensure that the region surrounding a cell is under gravitational collapse.

We note that in the study of Truelove et al. (1997), there was no implementation of sink particles. There, the authors showed that artificial fragmentation may occur in AMR simulations if the ratio of the Jeans length to the grid scale is too small. However, in simulations where sink particles are introduced, the formal requirements on resolution need not be identical to the case when there are no sink particles. Previous authors (Federrath et al. 2010; Krumholz et al. 2004) showed that they were able to avoid artificial fragmen-

tation by capping the density at the Truelove value (see Equation 4.6). However, we find that when a slightly higher density criterion (motivated by LP collapse) is adopted for sink particle creation, there is still no artificial fragmentation, and in fact the mass evolution follows similar tracks as it does when the Truelove density threshold is used (see Fig. 4.14). The similarity among the mass evolution tracks for different sink particle creation criteria suggests that the class of sink particle methods currently in use provides reliable results for core collapse and accretion.

4.5   Summary

We have presented an implementation of sink particles to the grid-based Eulerian hydrodynamics code *Athena*. A standard particle-mesh method is adopted to calculate gravity forces by and on the sink particles, with the Poisson equation solved via FFT methods. We use the mass and momentum fluxes from the Riemann solver to update the mass and momentum of sink particles. Criteria for sink particle creation are similar to those used by other authors, although we suggest that a higher density threshold is motivated by the Larson-Penston profile that is known to develop as a generic stage of self-gravitating collapse. The Larson-Penston density threshold we adopt for sink creation in our method is a factor 14 larger than the "Truelove" density threshold adopted in other sink implementations; our method also differs from other implementations in that the sink region surrounding each particle consists of ghost zones rather than active zones. Outside the sink region, the density is below the Truelove value. Our tests show similar results whether we use higher or lower density thresholds for sink formation; additional testing in the future can explore whether artificial fragmentation is avoided in all cases. We validate our method and implementation with a series of tests. These tests include comparison of accretion rates with analytic solutions for self-similar collapse of isothermal spheres,

and comparison of accretion rates and solution profiles with 1D spherically-symmetric collapse of Bonnor-Ebert spheres and cores formed by converging supersonic flows. We demonstrate Galilean invariance of our accretion solutions onto sink particles.

To demonstrate application of our method, we present sample results for a simulation of planar converging supersonic flows with turbulence. Filaments form, and local collapse produces sink particles which then accrete material from filaments. The mass smoothly increases to exceed the mass of the initial bound core in which a sink formed. Sinks forming at early stages merge with other smaller sinks if sink regions (of standard size 3^3 zones) overlap. In the context of these converging flow tests, we have investigated various criteria that have been adopted for creation of sink particles. We find that a (large enough) density threshold and local gravitational potential minimum check give the same results as more strict sets of criteria in this case (and in other tests we have conducted).

The implementation of sink particles we present enables study of a wide range of astrophysical applications involving gravitational collapse of a gaseous medium. In particular, robust and accurate methods for implementing sink particles make it possible to track sequential formation of multiple protostars over long periods under realistic environmental conditions. As such, sink particles represent a crucial numerical tool for addressing key unsolved problems in star formation, including the origin of the stellar initial mass function. The implementation of sink particles we describe here will be made available to the community in an upcoming release of the *Athena* code.

Acknowledgments

the HPCC deepthought cluster administrated by the OIT at the University of Maryland, as well as the Borg cluster in the Department of the Astronomy.

Chapter 5

Summary and Future Work

5.1 Summary

Star formation takes place in GMCs pervaded by supersonic turbulence, and theoretical models of prestellar (protostellar) cores must take these large-scale supersonic flows into account. In this thesis, we developed a model for prestellar core formation and collapse for an idealized case with spherically symmetric geometry and a more realistic case with planar geometry. We also introduced a sink particle algorithm for future work on the post-collapse phase for planar case. With these investigations, we defined the stages of protostar evolution, and investigated typical statistical core properties and their relation to the Mach number of the mother GMCs.

In Chapter 2, we developed a unified model for protostar formation using numerical simulations of a set of spherically symmetric converging flows with different Mach numbers. To simulate the accretion process to the central protostar, sink cell was adopted. Although this assumption of spherical geometry was not realistic, the framework nevertheless captured the key aspects of the real situation. Throughout this work, we divided the protostar formation into four stages, summarized as follows.

1. Core building. As spherical supersonic flows converge to the center, a reversed

shock is created. As the shock front propagates outward, inflowing material is shocked and the mass of the post-shock region grows. Before the post-shock sphere becomes gravitationally supercritical, the mass inside the prestellar core is building up. During this stage, the core is not observable since the central density is not high enough.

2. Core collapse. As the core builds up enough mass, the gravitational force overwhelms the gas pressure and it starts to collapse. The collapse happens in an "outside-in" manner. During the collapse, the density profile can be fitted by a BE sphere. A protostar forms at the instant the collapse front propagates to the center. The density and velocity profile at this instant approaches the LP solution. During this stage, the core is observable.

3. Envelope infall. The mass reservoir inside the shock front infalls to the central protostar during this stage. The density and velocity profiles close to the protostar approaches the freefall solution.

4. Late accretion. After the envelope infall, the late accretion of the surrounding low density medium starts.

In Chapter 3, we adopted a more realistic geometric shape – planar converging flows. At sub-parsec scales, turbulent velocity perturbations induced density perturbations that grew strongly when the density was high enough for self-gravity to be important. In post-shock layers, turbulence and self-gravity collected gas into long, thin filamentary structures at the same time as the highest density regions within the filaments grew to become centrally condensed cores. The first two stages proposed in Chapter 2 were confirmed in this chapter. Prior to collapse, the velocities within dense cores remained subsonic, in spite of the highly supersonic flows that created them. As prestellar cores collapsed, their density and velocity profiles also approached the LP solution. We then investigated the median core masses, core radii, and the collapse time for the most evolved cores as a function of Mach number. We found that the median core masses fell between the analytical arguments for masses of the most evolved cores and the minimum core masses at late

times. The time for the first core to collapse was consistent with analytical argument that $t_{\text{coll}} \propto \mathcal{M}^{-1/2}$. We also showed that the core shape changed from oblate to prolate as it evolved toward collapse. As a side product, we developed a core-finding software using the largest-closed-contour of the gravitational potential to define the core boundary.

In Chapter 4, we implemented sink particles in the *Athena* code. Sink particles are a great way to track the evolution of one single collapsed core, or the evolution of the other uncollapsed regions in a stellar cluster simulation. We used the LP density at half cell size away from sink particles as the density criteria for creating sink particles. Local gravitational potential minimum, converging flow, and gravitationally bound state were checked for sink particle creation. The TSC scheme of the particle-mesh method was adopted for calculation of gravity in gas-particles interactions, and particle-particle interactions. Different from previous methods, the control volume in our implementation was treated as ghost-zones instead of active zones in the simulation grid. We tested the implementation with two equal mass orbits, the collapse of an isothermal sphere, the collapse of a BE sphere, and a 3D spherical converging flow. To show the new implementation is able to track stellar cluster formation, we ran a planar converging flow simulation from Chapter 3. We found that dense regions were able to collapse to form protostars after the first core collapses.

Note that sink particles with high masses in Figure 4.14 are not physical. First, the amplitude of perturbations is 10% of the original amplitude calculated by Equation (3.41). Low amplitude of perturbations makes the total kinetic energy much lower than what it should be and material falls into sink particles more easily. Second, we keep material inflowing to the simulation box from $\pm z$ directions during the whole simulation. The time scale from Figure 4.14 is $t_{\text{tot}} = 0.45 t_J$ (see Eq. (4.22)). Form Equation (3.42), the crossing time from the center to the edge of the cloud at $\mathcal{M} = 5$ is $t_{\text{cross}} = R/\sigma_v = (\alpha_{\text{vir}}/15)^{1/2}/2\pi \times t_J$. The coefficient is 0.44 with $\alpha_{\text{vir}} = 2$. We can

see that $t_{\rm tot} \sim t_{\rm cross}$, which is not realistic. Third, outflows and radiative heating from protostars are not included in this simulation. Li et al. (2004) showed that outflows from protostars is one of the major sources of the turbulent energy inside GMCs, and outflows shift the whole CMF/IMF to the lower mass end. Also, radiation from protostars would increase the surrounding temperature, which might change the material from gravitationally bound state to unbound state. On the other hand, OB stars usually form at the center of stellar clusters. UV radiation from OB stars will create HII regions, which can destroy the whole cloud. Also, magnetic fields will offer extra support against gravity and reduce the accretion to protostars (Li et al. 2004). Lastly, merged sink particles could be stellar clusters instead of one single protostar. The sink region in our simulation is $3\Delta x = 3 \times L_J/256 \sim 2110\mathrm{AU}$ at $n_{\rm H_2,0} = 10^3 \mathrm{cm}^{-3}$, which is larger the typical size of circumstellar disk size (from 100 to 1000 AU) (see e.g. McCaughrean & O'dell 1996; Vicente & Alves 2005).

5.2 Future Work

The most important question to star formation theory is what determines the final stellar masses. Since observed CMFs are similar to the IMF in shape, and CMFs in turbulence simulations resemble observed CMFs, comparing core masses before collapse and protostellar masses after collapse will offer a direct solution to the above question. The implementation of sink particles to *Athena* makes researching these questions possible.

The output from star formation simulations depends critically on the initial conditions for the parent cloud. Girichidis et al. (2011) show that the initial clump profiles, the perturbation patterns and the compressibility of perturbations will affect the resulting CMFs. The connection between the resultant CMF/IMF to cloud conditions is unknown. Also, some recent work of stellar cluster formation start with very high (cluster-like) density

(see e.g., Krumholz et al. 2011, 2012; Li et al. 2010; Offner et al. 2008; Wang et al. 2010), but do not address the question of how such a dense region could have formed within a cloud without already fragmenting.

So far, no systematic investigation has been done on how different physical effects, such as magnetic fields, stellar outflows, and radiative transfer, will affect the CMF and the resultant IMF in simulation. Full exploration of the parameter space and comparing CMFs and IMFs with and without these physical processes will help us understand which processes are dominant during star formation.

Appendix A

Vacuum Boundary Condition Potential via Fourier Transforms

In this section, we provide details for the solution of Poisson's equation with vacuum boundary conditions. Let $-4\pi G \mathscr{G}(\mathbf{x}, \mathbf{x}')$ be the Green's function solution for the Poisson equation $\nabla^2 \Phi = -4\pi G \delta(\mathbf{x} - \mathbf{x}')$, so that the potential produced by a density field $\rho(\mathbf{x})$ is:

$$\Phi(\mathbf{x}) = -4\pi G \int \mathscr{G}(\mathbf{x}, \mathbf{x}') \rho(\mathbf{x}') d^3 \mathbf{x}. \tag{A.1}$$

For potential Φ at (x_a, y_b, z_c) within a domain (L_x, L_y, L_z) with dimensions (N_x, N_y, N_z), the corresponding discrete sum is:

$$\Phi(x_a, y_b, z_c) = -4\pi G \sum_{l=0}^{N_x-1} \sum_{m=0}^{N_y-1} \sum_{n=0}^{N_z-1} \mathscr{G}(x_a - x_l, y_b - y_m, z_c - z_n) \rho(x_l, y_m, z_n); \tag{A.2}$$

here (a, b, c) and (l, m, n) are the integer indices for the corresponding coordinates x, y, z respectively. $\Phi(x_a, y_b, z_c)$ is a convolution of $\mathscr{G}(\mathbf{x})$ and $\rho(\mathbf{x})$.

Because $\mathscr{G}(|\mathbf{x} - \mathbf{x}'|)$ is a function in the domain $[-L_x, L_x] \times [-L_y, L_y] \times [-L_z, L_z]$, and $\rho(\mathbf{x}')$ is a function in the domain $[0, L_x] \times [0, L_y] \times [0, L_z]$, if we define $\rho(x_l, y_m, z_n) = 0$ for $l < 0, m < 0$, or $n < 0$, Equation (A.2) can be re-written as:

$$\Phi(x_a, y_b, z_c) = -4\pi G \sum_{l=-N_x}^{N_x-1} \sum_{m=-N_y}^{N_y-1} \sum_{n=-N_z}^{N_z-1} \mathscr{G}(x_a - x_l, y_b - y_m, z_c - z_n) \rho(x_l, y_m, z_n), \tag{A.3}$$

We may define periodic functions with period $2L_x, 2L_y$ and $2L_z$ in x, y and z directions respectively, such that $\rho(\mathbf{x}')$ and $\mathscr{G}(\mathbf{x}, \mathbf{x}')$ agree with these periodic functions for $x \in [-L_x, L_x], y \in [-L_y, L_y]$ and $z \in [-L_z, L_z]$. Then from the Fourier convolution theorem, Equation (A.3) can be expressed in terms of the respective transforms $\hat{\mathscr{G}}$ and $\hat{\rho}$ of $\mathscr{G}(\mathbf{x}, \mathbf{x}')$ and $\rho(\mathbf{x}')$ from the Fourier convolution theorem:

$$\Phi(x_a, y_b, z_c) = \frac{-4\pi G}{(2N_x)(2N_y)(2N_z)} \sum_{i=0}^{2N_x-1} \sum_{j=0}^{2N_y-1} \sum_{k=0}^{2N_z-1} \hat{\mathscr{G}}_{ijk} \hat{\rho}_{ijk} e^{-2\pi i \left(\frac{ai}{2N_x} + \frac{bj}{2N_y} + \frac{ck}{2N_z} \right)}, \quad \text{(A.4)}$$

Note the summation index for i can be either from $-N_x \to N_x$ or $0 \to 2N_x - 1$ because $\hat{\mathscr{G}}$ and $\hat{\rho}$ are periodic. The same applies to j and k indices. In our implementation within *Athena*, Equation (A.4) is further decomposed into a sum over even and odd terms to save memory.

Appendix B

Gravitational Potential Identification of Cores

B.1   Introduction

GRID-core (Gravitational potential Identification of cores) is a core-finding method using the contours of the local gravitational potential to identify core boundaries, as described in Gong & Ostriker (2011). There it is shown that the GRID-core method applied to 2D surface density and 3D volume density are in good agreement, for bound cores. This user guide describes how to implement this method on observed surface density. We describe the algorithms used to find the largest closed contour that defines the outer core limit, and to identify the gravitationally bound interior part of the core. In addition, we describe use of the IDL code to implement GRID core-finding on FITS maps. Please cite the original paper (Gong & Ostriker 2011) if you use the code for presentation or publication.

B.2   Gravitational potential of surface density

For a layer of half-thickness H, the gravitational potential component $\Phi_{k,\text{2D}}$ of surface density component Σ_k in phase space is

$$\Phi_{k,\text{2D}} = -\frac{2\pi G \Sigma_k}{|\boldsymbol{k}|\,(1 + |\boldsymbol{k}H|)}, \tag{B.1}$$

where $|\boldsymbol{k}| = \sqrt{k_x^2 + k_y^2}$. Note that for $|\boldsymbol{k}H| \gg 1$, $\Phi_{k,\text{2D}} \sim -4\pi G \rho_k / k^2$, which is the solution of the Poisson equation in three dimensions, for $\rho_k = \Sigma_k / 2H$. For $|\boldsymbol{k}H| \ll 1$, eq. (B.1) is the solution of the Poisson equation for an infinitesimally thin layer. The gravitational potential $\Phi_{\text{2D}}(x,y)$ is the inverse FT of $\Phi_{k,\text{2D}}$. In the code, the default value of H is set as δx, the pixel size.

B.3   The largest closed contour

To identify cores via the gravitational potential, we first find and mark all the local minima of the gravitational potential; second, we find the largest closed potential contour surrounding each individual minimum. In the second step, we increase the contour level from the bottom of a given potential well step by step until it violates another minimum's marked territory by enclosing more than one extremum of the potential. We demonstrate this procedure in Figure B.1 using a one dimensional positive potential, $-\Phi$. In the first step, local maxima (minima in Φ) are marked in a descending order; note that only pixels at extrema are marked in this step. For the second step, we take the local maximum "1" as an example. Starting at $|\Phi_{\text{min}}|$, we decrease the isopotential contour level by amount of $\Delta\Phi$ from the top of "1", and find the region which is connected to "1" for each contour level. The blue lines in Figure B.1 show the contour levels, and the dotted blue lines show the identified connected regions to the maximum "1". At the 7th contour level, the connected region violates the territories of other maxima, because more than one extremum is

contained within the contour (i.e. lying above the lowest blue line, in Fig. 1.). The largest closed contour of "1" is thus defined by the 6th contour level, marked by the red lines. We repeat this procedure on all the local maxima and mark the largest closed contour of each maximum.

The contour interval $\Delta\Phi$ has a negligible effect on the results as long as it is small enough. We define the region enclosed by the largest closed contour as a GRID-core. If the distance between two potential minima is smaller than a certain value of pixels (corresponding to a physical distance which is set by the resolution), the regions associated with these two minima are merged and treated as a single GRID-core.
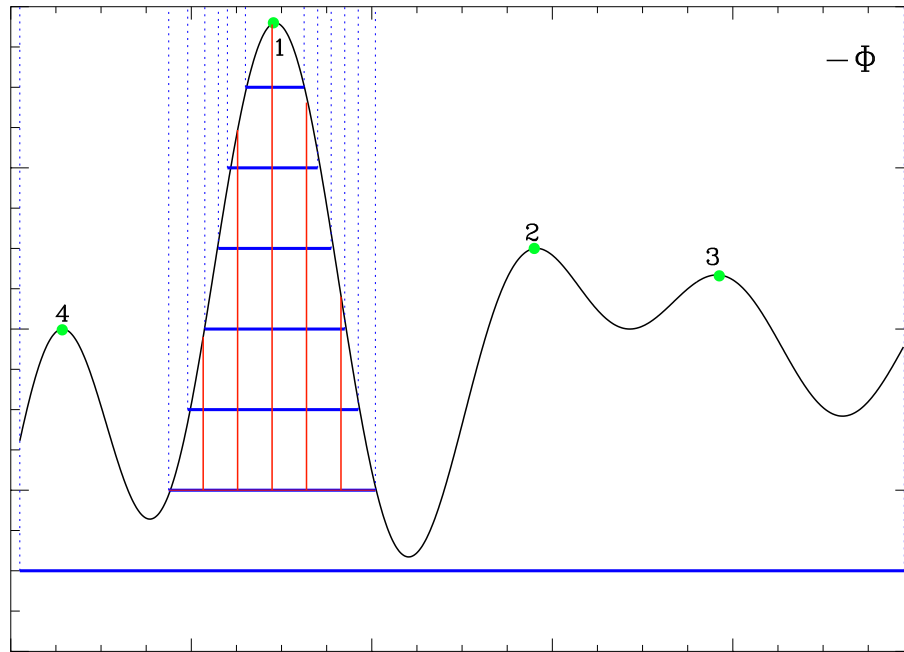
Figure B.1: Schematic of GRID-core identification method.

B.4 Bound thermal cores

Gas with sufficient thermal (and kinetic) energy will not be permanently (or even temporarily) bound to a given core, so the gravitational potential is not the final word. The lower density outer parts of a core are the least bound, and most subject to mass loss.

In order to identify only the bound regions of cores as marked by the gravitational potential, we add thermal energy to the gravitational energy, and only assigning a given fluid element to a core if $E_{th} + E_g < 0$. For any fluid element, the specific thermal energy is taken to be $E_{th} = (3/2)c_s^2$, for c_s the isothermal sound speed, and the specific gravitational potential energy is taken to be $E_g = \Phi - \Phi_{max}$, where Φ_{max} is the potential of the largest closed contour that defines the core. In the example of section 2, Φ_{max} would be equal to the potential of the sixth contour, i.e. $-\Phi_{max} = -\Phi_{min} - 6\Delta\Phi$. Including a thermal energy condition decreases the area so that (instantaneously) bound cores are smaller than cores defined by the potential alone. The resulting region is defined as a bound GRID-core.

Of course, the thermal energy can in fact be radiated away, so that gas that is initially near the largest closed contour may become more strongly bound after the interior of a core collapses. Thus, the gas within the outer (unbound) GRID-core region could evolve to become a bound core eventually.

Since bound cores must have $\Phi_{max} - \Phi_{min} < (3/2)c_s^2$, a value $\Delta\Phi \sim 0.1c_s^2$ is typically suitable for the potential contour spacing in identifying core boundaries. This is the default value adopted in the code.

We define a background surface density as the mean of the bottom 10% of the surface density; this mean value can be subtracted from the surface density in the core region when calculating core masses.

B.5   Structure of the code

The code contains two subroutines: destroy_bad, boundcore2d. The subroutine "destroy_bad" eliminates unresolved cores (total pixel number smaller than $\pi\times$r_pix_lim^2). The subroutine "boundcore2d" calculates core properties such as the coordinates of core center, total mass of the region inside the largest closed contour, mass of the bound core region, the depth of the gravitational potential well ($\Phi_{max} - \Phi_{min}$), and the total number of pixel numbers in marked cores, and bound regions. All the other procedures such as calculating the gravitational potential, and core-finding are handled in the main function. This section explains the function each block in the main function.

The first block is to calculate the gravitational potential of surface density. The surface density in g cm^{-2} is obtained by multiplying input H column density by $1.42m_p$. To create a periodic input for the FFT function, we zero-pad the surface density map in a domain four times as large, putting the surface density in the lower left quarter and zeros in the other three quarters. The next step is to apply a forward FFT to the extended surface density map. After multiplying by the coefficients as in equation (B.1), we apply a backward FFT to get the gravitational potential of the extended surface map. At the end of this block, the bottom left part of the gravitational potential field is extracted for later core-finding. Notice that the potential field is converted to positive values.

The second block is to merge local maxima (originally these are minima, since we use $-\Phi$ instead Φ) if they are too close to each other ($r_{distance} \le$ cls_dis).

The third block is to do GRID core-finding. The algorithm is described in Section 3. The block to eliminate unresolved cores is right after this block.

B.6 The IDL program

The calling sequence is:

output=grid_core($filename, pix\_size, T$,cls_dist=cls_dist,dp=dp,h=h,r_pix_lim=r_pix_lim)

ARGUMENTS:

filename : the name of the FITS file containing column density, where the maps is assumed to represent N_H of H nuclei (not H_2), in units of cm^{-2}

pix_size : the pixel resolution of the input column density map, in units of pc

KEYWORDS:

T : temperature of the cloud, using isothermal assumption, in units of K;

the default value is 10 K.

dp : the interval between potential contour levels, in units of $c_s^2 = kT/\mu$;

the default value is 0.1.

cls_dist : the closest distance between two local potential minima, in units of pix_size;

the default value is 6.

h : the minimum thickness of the 2D layer, in units of pix_size;

the default value is 1.

r_pix_lim : the minimum radius for a core to be considered resolved, in units of pix_size;

the default value is 3, half of cls_dist

OUTPUTS:

1. Two FITS files containing the marked regions identifying cores, e.g.: lcc_0.100.fits (GRID-cores), lcc_b_0.100.fits (bound GRID-cores). The suffix gives the value of dp ("0.100" for the default).

2. A FITS file containing a map of the computed gravitational potential phi.fits ($-\Phi$, in units of $[km/s]^2$).

3. A data file containing the properties of each core: location of potential minimum, total mass of marked region, background-subtracted mass of bound region, pixel numbers of both total and bound regions, gravitational potential $|\Phi_{min}|$ at the core center, gravitational potential depth $\Phi_{max} - \Phi_{min}$.

4. A postscript file showing the marked regions identifying cores: core_on_surfd.ps .

Examples of how to run the code:

1. Setting all keywords –

.run grid_core

output=grid_core("column.fits",0.011,10.,cls_dist=6,dp=0.01,h=1.0,r_pix_lim=3)

2. Using default keywords –

.run grid_core

output=grid_core("column.fits",0.011,10.)

The following figures shows the core-finding results for a column density map, using the first setting.
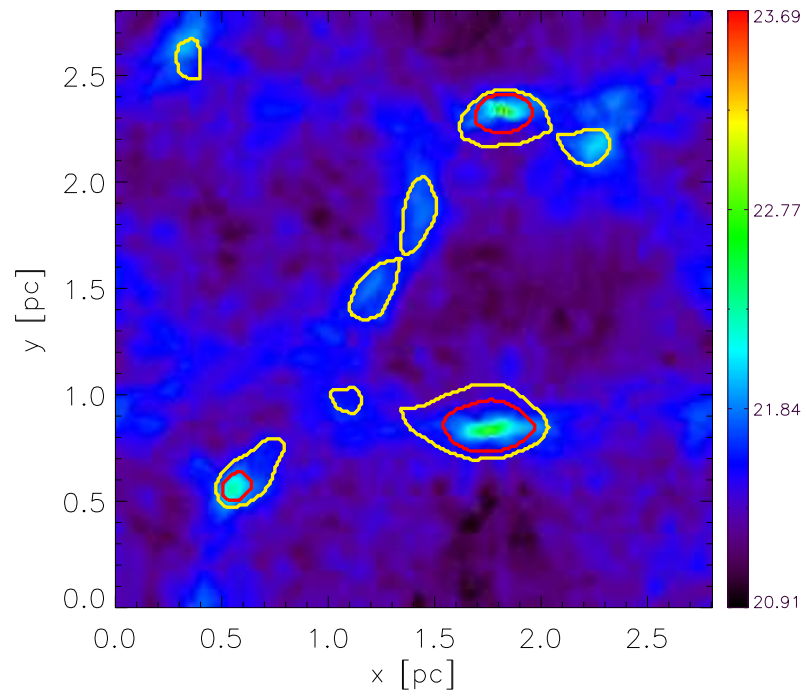
Figure B.2: GRID core-finding results. The yellow curves are GRID-cores and the red curves are bound GRID-cores. Color scale represents the column density ($\log N_H$).

Bibliography

Agertz, O., et al. 2007, MNRAS, 380, 963

Alves, J. F., Lada, C. J., & Lada, E. A. 2001, Nature, 409, 159

Alves, J., Lombardi, M., & Lada, C. J. 2007, A&A, 462, L17

André, P., Belloche, A., Motte, F., & Peretto, N. 2007, A&A, 472, 519

André, P., Basu, S., & Inutsuka, S.-i. 2008, in Structure Formation in Astrophysics, ed.
   G. Chabrier (Cambridge, UK:Cambridge University Press)

André, P., et al. 2010, A&A, 518, L102

Bacmann, A., André, P., Puget, J.-L., Abergel, A., Bontemps, S., & Ward-Thompson, D.
   2000, A&A, 361, 555

Ballesteros-Paredes, J., Klessen, R. S., & Vázquez-Semadeni, E. 2003, ApJ, 592, 188

Ballesteros-Paredes, J., Gazol, A., Kim, J., Klessen, R. S., Jappsen, A.-K., & Tejero, E.
   2006, ApJ, 637, 384

Ballesteros-Paredes, J., Klessen, R. S., Mac Low, M.-M., & Vazquez-Semadeni, E. 2007,
   Protostars and Planets V, 63

Banerjee, R., Vázquez-Semadeni, E., Hennebelle, P., & Klessen, R. S. 2009, MNRAS,
   398, 1082

Basu, S., & Mouschovias, T. C. 1994, ApJ, 432, 720

Basu, S., & Mouschovias, T. C. 1995, ApJ, 452, 386

Basu, S., & Mouschovias, T. C. 1995, ApJ, 453, 271

164

Basu, S., Ciolek, G. E., Dapp, W. B., & Wurster, J. 2009, New Astronomy, 14, 483

Bate, M. R., Bonnell, I. A., & Price, N. M. 1995, MNRAS, 277, 362

Bate, M. R. 2012, MNRAS, 419, 3115

Beichman, C. A., Myers, P. C., Emerson, J. P., Harris, S., Mathieu, R., Benson, P. J., & Jennings, R. E. 1986, ApJ, 307, 337

Bergin, E. A., & Tafalla, M. 2007, ARA&A, 45, 339

Beuther, H., & Schilke, P. 2004, Science, 303, 1167

Blitz, L., Fukui, Y., Kawamura, A., Leroy, A., Mizuno, N., & Rosolowsky, E. 2007, Protostars and Planets V, 81

Bodenheimer P., & Sweigart A. 1968, ApJ, 152, 515

Bonnell, I. A., Bate, M. R., & Vine, S. G. 2003, MNRAS, 343, 413

Bonnell, I. A., Clarke, C. J., & Bate, M. R. 2006, MNRAS, 368, 1296

Bonnor W.B. 1956, MNRAS, 116,351

Boss, A. P., & Black, D. C. 1982, ApJ, 258, 270

Broderick, A. E., Keto, E., Lada, C. J., & Narayan, R. 2007, ApJ, 671, 1832

Burkert, A., & Alves, J. 2009, ApJ, 695, 1308

Caselli, P., Benson, P. J., Myers, P. C., & Tafalla, M. 2002, ApJ, 572, 238

Chabrier, G. 2003, PASP, 115, 763

Chabrier, G. 2005, The Initial Mass Function 50 Years Later, 327, 41

Ciolek, G. E., & Basu, S. 2001, ApJ, 547, 272

Ciolek, G. E., & Mouschovias, T. C. 1994, ApJ, 425, 142

Clark, P. C., Bonnell, I. A., & Klessen, R. S. 2008, MNRAS, 386, 3

Dapp, W. B., & Basu, S. 2009, MNRAS, 395, 1092

Di Francesco, J., Myers, P. C., Wilner, D. J., Ohashi, N., & Mardones, D. 2001, ApJ, 562, 770

di Francesco, J., Evans, N. J., II, Caselli, P., Myers, P. C., Shirley, Y., Aikawa, Y., &

Tafalla, M. 2007, Protostars and Planets V, 17

Dubois, Y., Devriendt, J., Slyz, A., & Teyssier, R. 2010, MNRAS, 409, 985

Ebert R. 1955, Zs. Ap., 37,217

Elmegreen, B. G., & Elmegreen, D. M. 1978, ApJ, 220, 1051

Elmegreen, B. G. 2009, The Evolving ISM in the Milky Way and Nearby Galaxies

Elmegreen, B. G., & Scalo, J. 2004, ARA&A, 42, 211

Enoch, M. L., Evans, N. J., II, Sargent, A. I., Glenn, J., Rosolowsky, E., & Myers, P. 2008, ApJ, 684, 1240

Enoch, M. L., et al. 2006, ApJ, 638, 293

Evans, N. J., II, Rawlings, J. M. C., Shirley, Y. L., & Mundy, L. G. 2001, ApJ, 557, 193

Evans, N. J., II, et al. 2008, ApJS, 181, 321

Evans, N. J., et al. 2009, ApJS, 181, 321

Fatuzzo, M., & Adams, F. C. 2002, ApJ, 570, 210

Federrath, C., Banerjee, R., Clark, P. C., & Klessen, R. S. 2010, ApJ, 713, 269

Federrath, C., Sur, S., Schleicher, D. R. G., Banerjee, R., & Klessen, R. S. 2011, ApJ, 731, 62

Foster P.N., & Chevalier R.A. 1993, ApJ, 416, 303

Gammie, C. F., Lin, Y.-T., Stone, J. M., & Ostriker, E. C. 2003, ApJ, 592, 203

Gardiner, T. A., & Stone, J. M. 2005, Journal of Computational Physics, 205, 509

Gardiner, T. A., & Stone, J. M. 2008, Journal of Computational Physics, 227, 4123

Girichidis, P., Federrath, C., Banerjee, R., & Klessen, R. S. 2011, MNRAS, 413, 274

Glover, S. C. O., & Mac Low, M.-M. 2007, ApJS, 169, 239

Glover, S. C. O., & Mac Low, M.-M. 2007, ApJ, 659, 1317

Glover, S. C. O., & Clark, P. C. 2012, MNRAS, 421, 9

Goldreich, P., & Kwan, J. 1974, ApJ, 189, 441

Goldsmith, P. F. 2001, ApJ, 557, 736

Gómez, G. C., Vázquez-Semadeni, E., Shadmehri, M., & Ballesteros-Paredes, J. 2007, ApJ, 669, 1042

Gong, H., & Ostriker, E. C. 2009, ApJ, 699, 230

Gong, H., & Ostriker, E. C. 2011, ApJ, 729, 120

Goodman, A. A., Barranco, J. A., Wilner, D. J., & Heyer, M. H. 1998, ApJ, 504, 223

Gregersen, E. M., Evans, N. J., II, Zhou, S., & Choi, M. 1997, ApJ, 484, 256

Hatchell, J., Fuller, G. A., Richer, J. S., Harries, T. J., & Ladd, E. F. 2007, A&A, 468, 1009

Heitsch, F., Zweibel, E. G., Slyz, A. D., & Devriendt, J. E. G. 2004, ApJ, 603, 165

Heitsch, F., Slyz, A. D., Devriendt, J. E. G., Hartmann, L. W., & Burkert, A. 2007, ApJ, 665, 445

Heitsch, F., Hartmann, L. W., Slyz, A. D., Devriendt, J. E. G., & Burkert, A. 2008, ApJ, 674, 316

Hennebelle P., Whitworth A. P., Gladwin P. P., & Andre Ph. 2003, MNRAS, 340, 870

Hennebelle, P., & Chabrier, G. 2008, ApJ, 684, 395

Heyer, M. H., & Brunt, C. M. 2004, ApJ, 615, L45

Heyer, M., Krawczyk, C., Duval, J., & Jackson, J. M. 2009, ApJ, 699, 1092

Hockney, R. W., & Eastwood, J. W. 1981, Computer Simulation Using Particles, New York: McGraw-Hill, 1981,

Hopkins, P. F. 2012, MNRAS, 423, 2037

Hunter C. 1977, ApJ, 218, 834

Ikeda, N., & Kitamura, Y. 2009, ApJ, 705, L95

Ikeda, N., Kitamura, Y., & Sunada, K. 2009, ApJ, 691, 1560

Ikeda, N., Sunada, K., & Kitamura, Y. 2007, ApJ, 665, 1194

Iwasaki, K., & Tsuribe, T. 2008, PASJ, 60, 125

Jappsen, A.-K., Klessen, R. S., Larson, R. B., Li, Y., & Mac Low, M.-M. 2005, A&A,

435, 611

Jessop, N. E., & Ward-Thompson, D. 2000, MNRAS, 311, 63

Johnstone, D., Wilson, C. D., Moriarty-Schieven, G., Joncas, G., Smith, G., Gregersen, E., & Fich, M. 2000, ApJ, 545, 327

Johnstone, D., Fich, M., Mitchell, G. F., & Moriarty-Schieven, G. 2001, ApJ, 559, 307

Jørgensen, J. K., Johnstone, D., Kirk, H., & Myers, P. C. 2007, ApJ, 656, 293

Kandori, R., et al. 2005, AJ, 130, 2166

Keto, E., Broderick, A. E., Lada, C. J., & Narayan, R. 2006, ApJ, 652, 1366

Kim, W.-T., Ostriker, E. C., & Stone, J. M. 2002, ApJ, 581, 1080

Kirk, J. M., Ward-Thompson, D., & André, P. 2005, MNRAS, 360, 1506

Kirk, H., Johnstone, D., & Tafalla, M. 2007, ApJ, 668, 1042

Klessen, R. S. 2000, ApJ, 535, 869

Klessen, R. S. 2001, ApJ, 556, 837

Kolmogorov, A. 1941, Akademiia Nauk SSSR Doklady, 30, 301

Könyves, V., et al. 2010, arXiv:1005.2981

Koyama, H., & Ostriker, E. C. 2009, ApJ, 693, 1316

Kroupa, P. 2001, MNRAS, 322, 231

Krumholz, M. R., McKee, C. F., & Klein, R. I. 2004, ApJ, 611, 399

Krumholz, M. R., Klein, R. I., & McKee, C. F. 2011, ApJ, 740, 74

Krumholz, M. R., Klein, R. I., & McKee, C. F. 2012, ApJ, 754, 71

Kudoh, T., & Basu, S. 2008, ApJ, 679, L97

Lada, C. J., Muench, A. A., Rathborne, J., Alves, J. F., & Lombardi, M. 2008, ApJ, 672, 410

Larson R.B. 1969, MNRAS, 145, 271

Larson, R. B. 1981, MNRAS, 194, 809

Lee, C. W., & Myers, P. C. 1999, ApJS, 123, 233

Lee, C. W., Myers, P. C., & Tafalla, M. 1999, ApJ, 526, 788

Lee, C. W., Myers, P. C., & Tafalla, M. 2001, ApJS, 136, 703

Li, Z.-Y., & Nakamura, F. 2004, ApJ, 609, L83

Li, P. S., Norman, M. L., Mac Low, M.-M., & Heitsch, F. 2004, ApJ, 605, 800

Li, Z.-Y., Wang, P., Abel, T., & Nakamura, F. 2010, ApJ, 720, L26

Lubow, S. H., & Pringle, J. E. 1993, MNRAS, 263, 701

Mac Low, M.-M., & Klessen, R. S. 2004, Reviews of Modern Physics, 76, 125

Mardones, D., Myers, P. C., Tafalla, M., Wilner, D. J., Bachiller, R., & Garay, G. 1997, ApJ, 489, 719

Matzner, C. D., & McKee, C. F. 2000, ApJ, 545, 364

McKee, C. F., & Ostriker, E. C. 2007, ARA&A, 45, 565

McCaughrean, M. J., & O'dell, C. R. 1996, AJ, 111, 1977

Men'shchikov, A., et al. 2010, arXiv:1005.3115

Mestel, L., & Spitzer, L., Jr. 1956, MNRAS, 116, 503

Miller, G. E., & Scalo, J. M. 1979, ApJS, 41, 513

Motoyama, K., & Yoshida, T. 2003, MNRAS, 344, 461

Motte, F., Andre, P., & Neri, R. 1998, A&A, 336, 150

Motte, F., André, P., Ward-Thompson, D., & Bontemps, S. 2001, A&A, 372, L41

Mouschovias, T. C., & Spitzer, L., Jr. 1976, ApJ, 210, 326

Mouschovias, T. C. 1987, NATO ASIC Proc. 210: Physical Processes in Interstellar Clouds, 453

Mouschovias, T. C., & Ciolek, G. E. 1999, in NATO ASIC Proc.540: The Origin of Stars and Planetary Systems, ed. C.J. Lada & N. D. Kylafis (Dordrecht: Kluwer), 305

Myers, P. C. 1983, ApJ, 270, 105

Myers, P. C. 2005, ApJ, 623, 280

Nakamura, F. 1998, ApJ, 507, L165

Nakano, T., & Nakamura, T. 1978, PASJ, 30, 671

Nakamura, F., & Li, Z.-Y. 2008, ApJ, 687, 354

Neufeld, D. A., Lepp, S., & Melnick, G. J. 1995, ApJS, 100, 132

Nutter, D., & Ward-Thompson, D. 2007, MNRAS, 374, 1413

Offner, S. S. R., Klein, R. I., & McKee, C. F. 2008, ApJ, 686, 1174

Ogino S., Tomisaka K. & Nakamura F. 1999, PASJ, 51, 637

Onishi, T., Mizuno, A., Kawamura, A., Tachihara, K., & Fukui, Y. 2002, ApJ, 575, 950

Ostriker, E. C., Gammie, C. F., & Stone, J. M. 1999, ApJ, 513, 259

Ostriker, E. C., Stone, J. M., & Gammie, C. F. 2001, ApJ, 546, 980

Ostriker, E. C. 2003, Turbulence and Magnetic Fields in Astrophysics, 614, 252

Padoan, P., Jones, B. J. T., & Nordlund, A. P. 1997, ApJ, 474, 730

Padoan, P., & Nordlund, Å. 2002, ApJ, 576, 870

Padoan, P., & Nordlund, Å. 2004, ApJ, 617, 559

Padoan, P., Nordlund, Å., Kritsuk, A. G., Norman, M. L., & Li, P. S. 2007, ApJ, 661, 972

Padoan, P., & Nordlund, Å. 2011, ApJ, 730, 40

Passot, T., Pouquet, A., & Woodward, P. 1988, A&A, 197, 228

Pavlovski, G., Smith, M. D., & Mac Low, M.-M. 2006, MNRAS, 368, 943

Penston M.V. 1969, MNRAS, 144,425

Pineda, J. E., Rosolowsky, E. W., & Goodman, A. A. 2009, ApJ, 699, L134

Pineda, J. E., Goodman, A. A., Arce, H. G., Caselli, P., Foster, J. B., Myers, P. C., &
    Rosolowsky, E. W. 2010, ApJ, 712, L116

Peretto, N., André, P., & Belloche, A. 2006, A&A, 445, 979

Press, W. H., & Schechter, P. 1974, ApJ, 187, 425

Rathborne, J. M., Lada, C. J., Muench, A. A., Alves, J. F., Kainulainen, J., & Lombardi,
    M. 2009, ApJ, 699, 742

Reid, M. A., & Wilson, C. D. 2005, ApJ, 625, 891

Reid, M. A., & Wilson, C. D. 2006, ApJ, 644, 990

Richtmyer, R. D., & Morton, K. W. 1994, Malabar, Fla.: Krieger Publishing Co.,
—c1994, 2nd ed.,

Scalo, J. 1998, The Stellar Initial Mass Function (38th Herstmonceux Conference), 142,
201

Shirley, Y. L., Evans, N. J., II, Rawlings, J. M. C., & Gregersen, E. M. 2000, ApJS, 131,
249

Shu, F. H. 1977, ApJ, 214, 488

Shu, F. H., Adams, F. C., & Lizano, S. 1987, ARA&A, 25, 23

Shu, F. H., Ruden, S. P., Lada, C. J., & Lizano, S. 1991, ApJ, 370, L31

Simpson, R. J., Nutter, D., & Ward-Thompson, D. 2008, MNRAS, 391, 205

Skinner, M. A., & Ostriker, E. C. 2010, ApJS, 188, 290

Smith, R. J., Clark, P. C., & Bonnell, I. A. 2008, MNRAS, 391, 1091

Smith, R. J., Clark, P. C., & Bonnell, I. A. 2009, MNRAS, 396, 830

Sohn, J., Lee, C. W., Park, Y.-S., Lee, H. M., Myers, P. C., & Lee, Y. 2007, ApJ, 664, 928

Solomon, P. M., Rivolo, A. R., Barrett, J., & Yahil, A. 1987, ApJ, 319, 730

Springel, V. 2005, MNRAS, 364, 1105

Stanke, T., Smith, M. D., Gredel, R., & Khanzadyan, T. 2006, A&A, 447, 609

Stone, J. M., Gardiner, T. A., Teuben, P., Hawley, J. F., & Simon, J. B. 2008, ApJS, 178,
137

Stone, J. M., & Gardiner, T. 2009, New Astronomy, 14, 139

Stone J.M., & Norman M.L. 1992, ApJS, 80, 753

Tafalla, M., Myers, P. C., Caselli, P., & Walmsley, C. M. 2004, A&A, 416, 191

Testi, L., & Sargent, A. I. 1998, ApJ, 508, L91

Teyssier, R., Moore, B., Martizzi, D., Dubois, Y., & Mayer, L. 2011, MNRAS, 414, 195

Tilley, D. A., & Pudritz, R. E. 2004, MNRAS, 353, 769

Tilley, D. A., & Pudritz, R. E. 2007, MNRAS, 382, 73

Hanawa, T., & Nakayama, K. 1997, ApJ, 484, 238

Toro, E. F. 1999, Riemann Solvers and Numerical Methods for Fluid Dynamics (Berlin: Springer)

Troland, T. H., & Crutcher, R. M. 2008, ApJ, 680, 457

Truelove, J. K., Klein, R. I., McKee, C. F., et al. 1997, ApJ, 489, L179

Vazquez-Semadeni, E. 1994, ApJ, 423, 681

Vázquez-Semadeni, E., Banerjee, R., Gómez, G. C., et al. 2011, MNRAS, 414, 2511

Vicente, S. M., & Alves, J. 2005, A&A, 441, 195

Vishniac, E. T. 1994, ApJ, 428, 186

Vorobyov E. I., & Basu S. 2005, MNRAS, 360, 675

Wang, P., Li, Z.-Y., Abel, T., & Nakamura, F. 2010, ApJ, 709, 27

Walsh, A. J., Bourke, T. L., & Myers, P. C. 2006, ApJ, 637, 860

Ward-Thompson, D., Scott, P. F., Hills, R. E., & Andre, P. 1994, MNRAS, 268, 276

Ward-Thompson, D., André, P., Crutcher, R., Johnstone, D., Onishi, T., & Wilson, C. 2007, Protostars and Planets V, 33

Whitworth A., & Summers D. 1985, MNRAS, 214, 1

Whitworth, A. P., Bhattal, A. S., Chapman, S. J., Disney, M. J., & Turner, J. A. 1994, A&A, 290, 421

Williams, J. P., de Geus, E. J., & Blitz, L. 1994, ApJ, 428, 693

Wolfire, M. G., Hollenbach, D., & McKee, C. F. 2010, ApJ, 716, 1191

Zhou, S., Evans, N. J., II, Koempe, C., & Walmsley, C. M. 1993, ApJ, 404, 232

Zweibel, E. G. 2002, ApJ, 567, 962